Universidade do Minho

Jorge Filipe Pinto Carvalho

# Traction and Charging Systems for an Electric Motorcycle

Dissertação submetida na Universidade do Minho para a
obtenção do grau de Mestre em Eletrónica Industrial e de
Computadores Engenharia

Trabalho realizado sob a orientação:

Professor Doutor João Luiz Afonso

Doutor Delfim Pedrosa

Julho 2021

# DIREITOS DE AUTOR E CONDIÇÕES DE UTILIZAÇÃO DO TRABALHO POR TERCEIROS

## *Licença concedida aos utilizadores deste trabalho*

Aos meus Pais.

# Agradecimentos

O desenvolvimento desta dissertação de mestrado contou com o contributo fundamental de diversas pessoas a quem devo um enorme obrigado.

Desejo agradecer ao meu orientador, Doutor João Luiz Afonso pela disponibilidade, apoio, transparência, bem como pelas criticas e sugestões propostas durante a orientação.

Agradeço ao Doutor Delfim Pedrosa pela incansável disponibilidade, acompanhamento na várias fases de implementação, auxilio na montagem do hardware e no esclarecimento de dúvidas, além da boa-disposição e receptividade sempre mostradas.

Desejo transmitir um agradecimento especial ao Engenheiro Tiago Sousa pela ajuda prestada na resolução de problemas de simulação, bem como o apoio no desenvolvimento das PCBs, no que toca a circuitos de controlo, layout e mapeamento de hardware e pela supervisão durante os testes práticos.

Um agradecimento ao Doutor Vítor Monteiro pela ajuda prestada inicialmente no planeamento e estruturação do protótipo do projeto.

Agradeço aos investigadores, colegas de curso e sobretudo amigos de laboratório do Grupo de Eletrónica de Potência e Energia (GEPE), Cátia Oliveira, Luís Machado, Carlos Mendes, Carlos Martins, Daniel Barbosa, Sérgio Coelho pelo ambiente amigável proporcionado em todos os momentos passados no laboratório do GEPE, pelo companheirismo e espirito de ajuda, além do diferente ponto de vista oferecido na resulоção de problemas.

Um agradecimento também ao DAIPESEV – Development of Advanced Integrated Power Electronic Systems for Electric Vehicles, onde se enquadra o desenvolvimento deste projeto de dissertação.

Agradeço também aos meus amigos que sempre tiveram uma palavra de motivação para me dar nos momentos mais dificeis do meu percurso académico.

Quero sobretudo e em especial agradecer aos meus pais pela oportunidade concedida e sacrificios feitos para que eu sempre tivesse todas as condições e recursos necessários durante do meu percurso académico. Sem eles não estaria agora a escrever esta nota de agradecimentos.

# STATEMENT OF INTEGRITY

I hereby declare having conducted this academic work with integrity. I confirm that I have not used plagiarism or any form of undue use of information or falsification of results along the process leading to its elaboration.

I further declare that I have fully acknowledged the Code of Ethical Conduct of the University of Minho.

# Abstract

With the current mobility paradigm, it is proven that excessive energy consumption and low energy efficiency are harming the planet and deteriorating human life conditions. Therefore it is required to substitute Internal Combustion Engines (ICEs) for electric motors and consequently shift gradually to fully electric vehicle (EV) fleets. The electrification of mobility is one of the most researched topics in all technology fields. These efforts put society closer to achieve energy sustainability and reduce the negative human impact on the environment. With this, low energy consumption vehicles such as electric motorcycles (EMs) are a very viable solution to reduce energy consumption. Due to their low power and weight, EMs have high energy efficiency and are optimized for urban transit. In this context, it becomes necessary to develop systems and prototypes common to any EV. Therefore the focus of this thesis is to implement motor traction and battery charging systems for an EM.

One of the most important characteristics of an electric traction system is the possibility of applying regenerative braking. Regenerative braking converts the mechanical energy, otherwise dissipated by conventional brakes, into reusable energy that is sent back to the batteries. This process occurs due to the operation of the traction system's power converter and improves greatly the energy efficiency of the EV. Besides, is proposed that the traction system's input is a hand accelerator that can control the motor speed/torque.

The charging system acts as an interface between the power grid and the motorcycle system. In applications such as EV charging, it is important to ensure power quality in order to maintain the developed system and the power grid healthy. With this, the first stage of the charger is AC-DC rectification and besides regulating the DC-link voltage should also act as a Power Factor Corrector (PFC) and compensate current harmonics. Secondly, the charger system should be able to regulate and control the charging process by maintaining a constant current, voltage, or temperature. The charger should also ensure the battery's safety, and offer the possibility of regulating the charging speed.

This document, details the development of traction and charger systems from the state of the art research and topologies presentation, to the computational simulations, and respective experimental tests/validation.

**Keywords:** Battery Charging; Electric Motorcycles; Brushed DC Motor; Regenerative Braking; Torque Control.

# Resumo

Com o paradigma da mobilidade é evidente que o consumo excessivo de energia proveniente de combustíveis fosseis está a prejudicar o planeta. Por conseguinte, é necessário substituir os Motores de Combustão Interna (MCI) por motores eléctricos e, consequentemente, transitar gradualmente para frotas de veículos 100% elétricos (VE). A eletrificação da mobilidade é um dos tópicos com mais investimento em investigação de todos os campos tecnológicos. Estes esforços aproximam a sociedade para alcançar a sustentabilidade energética e reduzir o impacto humano no ambiente através da extração de combustíveis fósseis. Com isto, veículos de baixo consumo energético, tais como motociclos eléctricos (ME), são uma solução muito viável. Devido à sua baixa potência e peso, os MEs possuem elevada eficiência energética e são optimizados para o trânsito urbano.. Neste contexto, torna-se necessário o desenvolvimento de sistemas e protótipos comuns a qualquer EV. Portanto, o foco desta dissertação é a implementação dos sistemas de tração para um motor e de carregamento de baterias para um ME.

Uma das características mais importantes de um sistema de tracção elétrica é a possibilidade de aplicar travagem regenerativa. A travagem regenerativa converte a energia mecânica, de outro modo dissipada pelos travões convencionais, em energia reutilizável que é reenviada para as baterias. Este processo ocorre devido ao funcionamento do conversor do sistema de tracção e aumenta a eficiência energética do VE. Além disso, é proposto que o sistema de tracção seja controlado através de um acelerador manual que pode controlar a velocidade/torque do motor.

O sistema de carregamento actua como interface entre a rede elétrica e o motociclo. Em aplicações como o carregamento de VEs, é importante assegurar a qualidade da energia tanto do sistema desenvolvido como da rede de elétrica. Com isto, a primeira fase do carregador, para além de regular a tensão DC, deve também actuar como corrector do factor de potência (PFC). Em segundo lugar, o sistema carregador deve ser capaz de regular e controlar o processo de carregamento mantendo uma corrente, tensão ou temperatura constantes. O carregador, para além de fazer a interface entre o DC-link e a bateria, deve oferecer a possibilidade de regular a taxa de carregamento.

Este documento, detalha o desenvolvimento de sistemas de tracção e carregamento desde a investigação e apresentação das topologias mais utilizadas, até às simulações computacionais, e respectivos testes experimentais/validação.

**Palavras-chave:** Carregamento de Baterias; Controlo de Torque; Motociclos Elétricos; Motor DC de Escovas; Travagem Regenerativa.

# Contents

**List of Figures** xi

**List of Tables** xv

**Abbreviations and Acronyms List** xvi

**1 Introduction** 1

1.1 Energy Problem and Electric Mobility 1

1.2 EV Motors and Traction Controllers 2

1.3 Battery Charging and Power Quality 4

1.4 Proposed System Prototypes 7

1.5 Motivation 8

1.6 Objectives 8

1.7 Organization and Structure 9

**2 Charger System - Power Factor Correction and Battery Charging Solutions** 11

2.1 Introduction 11

2.2 Diode Full-Bridge Rectifier and PFC Solutions 11

2.3 Full Active Bridge Converter 13

2.4 Synchronization with the Power Grid 14

2.5 DC-Link Regulation 15

2.6 AC-DC Rectifier Control Techniques 15

2.6.1 Proportional-Integral Control with SPWM technique 16

2.6.2 Predictive Control with SPWM technique 17

2.7 Battery Charging and Charger Topologies 18

2.8 Chapter Conclusion 21

**3 DC Motors - Motor Operation, Topologies and Control Methods** 23

3.1 Introduction 23

3.2 BDC Motor Constitution and Principle of Operation 23

3.2.1 Operation as Generator 25

3.2.2 DC motor Equivalent Model 26

3.3 BDC Motor Converters 27

3.3.1 Full-Bridge Converter . . . . . . . . . . . . . . . . . . . . . . . . . . 27
3.3.2 Half-Bridge Converter . . . . . . . . . . . . . . . . . . . . . . . . . . 29
3.4 Motor Control Techniques . . . . . . . . . . . . . . . . . . . . . . . . . . 30
3.4.1 PI Torque Control Based on the Converter Model . . . . . . . . . . . . . . . 31
3.4.2 Hysteresis Band control . . . . . . . . . . . . . . . . . . . . . . . . . . 32
3.5 Chapter Conclusion . . . . . . . . . . . . . . . . . . . . . . . . . . . . . 34

**4 Simulations of the Motor and Charger Systems 35**
4.1 Introduction . . . . . . . . . . . . . . . . . . . . . . . . . . . . . . . . 35
4.2 Motor Module Simulation . . . . . . . . . . . . . . . . . . . . . . . . . . 35
4.2.1 Motor Simulation Model . . . . . . . . . . . . . . . . . . . . . . . . . . 36
4.2.2 Motor Control System . . . . . . . . . . . . . . . . . . . . . . . . . . . 37
4.2.3 Simulation of Forward modes with 10 Nm Load and a constant DC Power Supply 39
4.2.4 Simulation with 20 Nm Load and 72 V Fixed DC Power Supply . . . . . . . . . 41
4.2.5 Simulation of Regenerative Braking . . . . . . . . . . . . . . . . . . . . . 43
4.3 AC-DC Converter Simulation - Power Factor Correction . . . . . . . . . . . . . . 45
4.3.1 PLL Algorithm for Power Grid Synchronization . . . . . . . . . . . . . . . . . 45
4.3.2 DC-Link Voltage Regulation . . . . . . . . . . . . . . . . . . . . . . . . . 46
4.4 PFC Current Control and PWM technique . . . . . . . . . . . . . . . . . . . . 49
4.5 DC-DC Converter - Battery Charging System . . . . . . . . . . . . . . . . . . . 49
4.6 Charger Simulation Model . . . . . . . . . . . . . . . . . . . . . . . . . . . 50
4.6.1 AC-DC Converter Simulation Results . . . . . . . . . . . . . . . . . . . . . 50
4.6.2 Battery Charging System Results . . . . . . . . . . . . . . . . . . . . . . 51
4.7 Chapter Conclusion . . . . . . . . . . . . . . . . . . . . . . . . . . . . . 52

**5 Traction and Charging Systems Implementation 54**
5.1 Introduction . . . . . . . . . . . . . . . . . . . . . . . . . . . . . . . . 54
5.2 Control System Implementation . . . . . . . . . . . . . . . . . . . . . . . . 54
5.2.1 Digital Signal Controller (DSP) . . . . . . . . . . . . . . . . . . . . . . . 55
5.2.2 Voltage Sensors . . . . . . . . . . . . . . . . . . . . . . . . . . . . . . 56
5.2.3 Current Sensors . . . . . . . . . . . . . . . . . . . . . . . . . . . . . . 58
5.2.4 Sensor for Measuring the Rotor Speed . . . . . . . . . . . . . . . . . . . . 59
5.2.5 Control Board - Signal Conditioning . . . . . . . . . . . . . . . . . . . . . 60
5.2.6 Control Board - Protection and Error Processing . . . . . . . . . . . . . . . 64
5.2.7 Driver circuits for the Charger Converter . . . . . . . . . . . . . . . . . . . 66
5.2.8 Driver modules for the Motor Full-Bridge Converter . . . . . . . . . . . . . . 67

- 5.2.9 DAC - Digital to Analog Board . . . . 69
- 5.3 Power System Development . . . . 69
  - 5.3.1 Charger Converter Prototype . . . . 69
  - 5.3.2 Motor Converter Prototype . . . . 70
- 5.4 Chapter Conclusion . . . . 73

**6 Experimental Tests and Results 75**

- 6.1 Introduction . . . . 75
- 6.2 Motor Operation Results . . . . 75
- 6.3 Charger Operation Results . . . . 78
  - 6.3.1 Synchronization with the Power Grid . . . . 78
  - 6.3.2 Power Factor Correction and DC-Link Regulation . . . . 79
  - 6.3.3 Buck Converter - Charger Control Operation . . . . 80
- 6.4 Chapter Conclusion . . . . 82

**7 Conclusion 83**

- 7.1 General Conclusions . . . . 83
- 7.2 Future Work Proposals . . . . 86

**Bibliography 88**

# List of Figures

1.1 Photographs of electric motors: (a) Characteristic aesthetic of the rotor of a DC motor; (b) Example of the stator of a DC motor (no correlation with (a)); (c) Cut of a squirrel-cage induction motor. . . . . . . . . . . . . . . . . . . . . . . . . . . . . . . 3
1.2 Example of a motor controller produced by the company Piktronik. . . . . . . . . . . 4
1.3 Typical power grid energy consumption throughout the day. . . . . . . . . . . . . . . 5
1.4 Comparison between an on-board charger and an off-board charger. . . . . . . . . . 6
1.5 Current wave with harmonic distortion: (a) Current breakdown in the respective frequency components; (b) Total Current. . . . . . . . . . . . . . . . . . . . . . . . . . . 6
1.6 Proposed topology for the implementation of a traction and charging systems using 2 converters. . . . . . . . . . . . . . . . . . . . . . . . . . . . . . . . . . . . . 7
1.7 Proposed topology for the implementation of a traction and charging systems using 3 converters. . . . . . . . . . . . . . . . . . . . . . . . . . . . . . . . . . . . . 8

2.1 AC-DC diode full-bridge rectifier schematic. . . . . . . . . . . . . . . . . . . . . . . 12
2.2 Power grid current absorbed by a DFB rectifier. . . . . . . . . . . . . . . . . . . . . 12
2.3 Electric schematic of a PFC boost rectifier. . . . . . . . . . . . . . . . . . . . . . . 13
2.4 Grid current absorbed by a PFC boost converter. . . . . . . . . . . . . . . . . . . . 13
2.5 Electric schematic of an Full active bridge converter. . . . . . . . . . . . . . . . . . 14
2.6 Block diagram of a typical PLL algorithm. . . . . . . . . . . . . . . . . . . . . . . 15
2.7 Block diagram of the PI control action, the respective SPWM technique. . . . . . . . . 16
2.8 Block diagram of the predictive control and the respective SPWM technique. . . . . . 18
2.9 Photograph of a 1.6 kWh Li-ion battery bank produced by the company Varta. . . . . . 19
2.10 Equivalent model of a generic battery. . . . . . . . . . . . . . . . . . . . . . . . . 19
2.11 Schematic of the charger topology for grid-battery interface. . . . . . . . . . . . . . 20
2.12 Battery current, voltage and SoC curves during CC-CV charging. . . . . . . . . . . . 20

3.1 Operation and of a BDC motor based on the Lorentz law and the respective creation of torque. $F$ represents the force created, 1 and 2 are the brushes, and A and B are the respective commutation segments that are connected to a DC supply: (a) and (b) show the rotor on two positions shifted 180° from each other. $\Omega$ represents the rotation direction, and $\odot$ and $\otimes$ the vector direction, into the page and out of the page, respectively. The S and N are the stator poles. . . . . . . . . . . . . . . . . . . . . . . . . . . 25
3.3 H-bridge electric schematic applied to the equivalent model of a BDC motor . . . . . . 28
3.4 H-Bridge topology, its behavior in each operation zone and the respective current flow. . 29
3.5 Half-bridge topology schematic. . . . . . . . . . . . . . . . . . . . . . . . . . . . 30

3.6 Categorization of the areas of operation on a $I_{ref}$ and $V_{emf}$ two-axis plane. . . . . . . 31

3.7 Block diagram of the torque control technique. . . . . . . . . . . . . . . . . . . . . . . 32

3.8 Block diagram of the hysteresis control technique. . . . . . . . . . . . . . . . . . . . . 33

3.9 Reference, output and compare signals resulting from hysteresis voltage control. . . . . 33

4.1 Simulation model of a DC motor. . . . . . . . . . . . . . . . . . . . . . . . . . . . . 37

4.2 Motor converter and control system simulation design. . . . . . . . . . . . . . . . . . . 38

4.3 PWM technique where it is shown the resulting PWM duty-cycle according to the control output value and the triangular wave. . . . . . . . . . . . . . . . . . . . . . . . . . . 39

4.4 Response time simulation waveform of the reference current ($i_{ref}$) and the motor current ($i_m$). . . . . . . . . . . . . . . . . . . . . . . . . . . . . . . . . . . . . . . . . . 39

4.5 Simulation waveforms of a $i_{ref}$ slope for and the respective $i_{motor}$. . . . . . . . . . . . 40

4.6 Simulation waveforms of the evolution of speed and $V_{emf}$, according to the slope reference current. . . . . . . . . . . . . . . . . . . . . . . . . . . . . . . . . . . . . . . . . . 40

4.7 Simulation waveforms of the operation modes and transitions throughout the simulation of the traction system with a slope reference current and a 10 Nm load. . . . . . . . . 41

4.8 Motor simulation results with a fixed 72 V DC power supply: (a) Mechanical characteristics of the motor, speed and torque; (b) Relation between the torque performed by the motor (motor torque) and the attached load; (c) Electrical characteristics of the motor, motor current and back-EMF voltage; (d) Motor operation modes from 1 to 4; (e) Comparison between reference current and motor current. . . . . . . . . . . . . . . . . . . . . . 43

4.9 Simulation design of the motor converter supplied by a 72 V battery model. . . . . . . . 43

4.10 Motor simulation results with a 72 V battery: (a) Corresponds to battery voltage evolution throughout the simulation; (b) Represents the input reference current and the back-EMF voltage produced by the motor;
(c) Corresponds to the mode of operation. . . . . . . . . . . . . . . . . . . . . . . . 44

4.11 AC-DC rectifier schematic, showing the different sub-parts of the system and the overall structure of the charger module, where the control methods are highlighted in yellow. . . 45

4.12 PLL algorithm simulation: (a) $\omega t$ angle with 50 Hz frequency in phase with $v_g$; (b) Waveform comparison between grid $v_g$ and the PLL wave, when the control starts at 0° power grid phase, showing they are synchronized; (c) Presents an example where the algorithm is enabled at 90° grid phase. . . . . . . . . . . . . . . . . . . . . . . . . 47

4.13 Schematic of the DC-link regulation PI control. . . . . . . . . . . . . . . . . . . . . . 47

4.14 Waveform evolution of grid current $i_g$ ((a)) and DC-link voltage $v_{dc}$ ((b)) with bypass resistors and respective stages of regulation until the dc voltage reaches permanent state. 48

4.15 Comparison between voltage and current waveforms with and without the implementation of a bypass resistors, blue curve and orange curve, respectively: (a) Waveforms of the voltage evolution; (b) Waveforms of the current evolution. . . . . . . . . . . . . . . . 49

4.16 Charger system simulation design. . . . . . . . . . . . . . . . . . . . . . . . . . . . 50

4.17 Simulation waveforms of the AC-DC converter and the respective PFC and DC-link regulation controls: (a) Power grid current ($i_g$) and reference current ($i_{ref}$); (b) DC-link voltage $v_{dc}$. . . . . . . . . . . 51
4.18 Simulation waveforms of the buck converter for charging current control. . . . . . . . . 52

5.1 Simplified schematic of the motorcycle prototype. . . . . . . . . . 55
5.2 DSP and the respective peripheral boards, as well as the programming software used: (a) TMS320F283355 card integrated on the developed board by GEPE; (b) TMDSDOCK28335 docking station; (c) Code Composer Studio programming environment. 56
5.3 CYHVS5-25A sensor: (a) Picture of the sensor encapsulation; (b) Application schematic of the voltage sensor. . . . . . . . . . 57
5.4 LA current sensor series: (a) generic application board and encapsulation of a LA current sensor series; (b) application schematic of the LA sensor. . . . . . . . . . 59
5.5 Picture of the AM512B sensor integrated with the evaluation board RMK1B. . . . . . . . 60
5.6 Voltage divider schematic. . . . . . . . . . 61
5.7 Schematic of the non-inverting amplifier for offset addition. . . . . . . . . . 61
5.8 Low-pass filter for ADC input. . . . . . . . . . 63
5.9 Window Comparator utilized for error detection. . . . . . . . . . 64
5.10 LM555 error processing. . . . . . . . . . 65
5.11 ADUM3123 and driver configuration. . . . . . . . . . 66
5.12 Control board developed and the respective sub-circuits. . . . . . . . . . 67
5.13 Command and driver boards utilized for the motor control system: (a) GEPE-0015 command board;
(b) GEPE-0025 main driver board with the integrated SKH122AH4 driver. . . . . . . . . 68
5.14 Picture of the GEPE-0016 PCB. . . . . . . . . . 68
5.15 Picture of the DAC board used. . . . . . . . . . 69
5.16 Picture of the charger power board were are detailed the respective components. . . . . 71
5.17 Picture of the ME1003 motor: (a) side view of the motor; (b) bottom of the ME1003, where the speed sensor is attached. . . . . . . . . . 71
5.18 Pictures of the SKM400GB066D IGBT module: (a) Side view, showing the IGBT leg layout; (b) Top view of the IGBT. . . . . . . . . . 72
5.19 Picture of the developed motor converter prototype. . . . . . . . . . 72
5.20 Traction system assembly and respective connections between PCBs. . . . . . . . . . 73
5.21 Motor workbench utilized for the experimental tests. . . . . . . . . . 73

6.1 Typical current (CH4: 5 A/div) and voltage (CH1: 20 V/div) waveforms of the ME1003 motor, during acceleration mode, and the respective PWM signals (CH2,CH3: 10 V/div), for driver validation. Time scale of 25 $\mu$s. . . . . . . . . . 76

6.2 Waveform results of motor operation showing the waveforms/curves of the back-EMF voltage
(CH1: 10 V/div), mode (CH2: modes 0 to 4 (0 no control) as per established before (1 mode/div)), reference current (CH3: 5 A/div), and motor current (CH4: 5 A/div): (a) Deceleration test while in mode 1; (b) and (c) Acceleration test followed by regenerative braking; (d) Test of modes 1, 2, 3. Time scale of 1 s/div. . . . . . . . . . . . . . . . . 77

6.3 Tachometer measuring the rotation speed of the motor axle using the light emitter mode. 77

6.4 PLL Synchronization (CH2: 20 V/div) with the power grid voltage (CH1: 20 V/div). . . . 78

6.5 Frequency component of the PLL signal, $\omega$t, during steady-state regime (CH3: 2 mV/div, corresponding to 2 $\pi$/div). . . . . . . . . . . . . . . . . . . . . . . . . . . 79

6.6 Synthesized current without the current control (CH4: 1.00 A/div), pre-charge DC-link voltage
(CH2: 10 V/div) and power grid voltage (CH1: 10 V/div). Time scale of 5 ms/div. . . . 79

6.7 PFC waveform results showing the absorbed power grid current (CH4: 1 A/div), reference current,
(CH3: 2 A/div), DC-link voltage (CH2: 20 V/div) and : (a) Grid voltage (CH1: 10 V/div); (b) DC-side current (2 A/div): (c) Harmonic analysis of the absorbed current and the respective THD measurement. Time scale of 5 ms/div. . . . . . . . . . . . . . . . . 80

6.8 Buck converter waveform results showing power grid voltage (CH1: 20 V/div), DC-link voltage (CH2: 20 V/div), battery (load) voltage (CH3: 5 V/div) and battery current (CH4: 500 mA/div). Time scale of 5 ms/div. . . . . . . . . . . . . . . . . . . . . . . . 81

6.9 PI Control behavior waveforms: Reference current (CH2: 500 mA/div), battery current (CH4: 500 mA/div) and duty-cycle (CH3: Relative value). Time scale of 100 $\mu$s/div. . . 81

6.10 PWM signal (CH1: 10 V/div) comparison with the Load current (CH4: 500 mA/div), and the reference current (CH2: 1 A/div): (a) Results with a 1 A reference; (b) Results with a 2 A reference. Time scale of 5 $\mu$s/div. . . . . . . . . . . . . . . . . . . . . . . . 82

# List of Tables

2.1 Effects on the PI control resulting of the increase of each a gain independently. . . . . . 17

3.1 Motor modes of operation and the corresponding combinations of IGBT states. . . . . . 28

4.1 Technical data of the DC motor simulated. . . . . . . . . . . . . . . . . . . . . . . . . 36
4.2 Motor parameters utilized for simulation model . . . . . . . . . . . . . . . . . . . . . 36
4.3 Reference currents applied to the braking controller during different instants of the motor operation for a 20 Nm load . . . . . . . . . . . . . . . . . . . . . . . . . . . . . 41

# Abbreviations and Acronyms List

| | |
|---|---|
| **AC** | Alternating Current |
| **ADC** | Analog to Digital Converter |
| **BDC** | Brushed DC |
| **BLDC** | Brushless DC |
| **BMS** | Battery Management System |
| **DAC** | Digital-To-Analogic Converter |
| **DC** | Direct Current |
| **DSP** | Digital Signal Processor |
| **EV** | Electric Vehicle |
| **EV** | Electric Vehicle |
| **DFB** | Diode Full-Bridge |
| **ICE** | Internal Combustion Engine |
| **G2V** | Grid-to-Vehicle |
| **LF** | Loop Filter |
| **OCV** | Open-Circuit Voltage |
| **PCB** | Printed Circuit Board |
| **PD** | Phase Detector |
| **PLL** | Phase-Locked-Loop |
| **PM** | Permanent Magnet |
| **PWM** | Pulse-Width Modulation |
| **SoC** | State-of-Charge |
| **TOU** | Time-of-Use |
| **THD** | Total Harmonic Distortion |
| **V2G** | Vehicle-to-Grid |
| **VCO** | Voltage-Controlled Oscillator |

# Chapter 1

# Introduction

## 1.1 Energy Problem and Electric Mobility

Internal Combustion Engine (ICE) vehicles, which use fossil fuels as the only source of energy, represent the majority of the existing worldwide on-road vehicles today. The shortage of these non-renewable resources, as well as the environmental impact they bring, are considered as some of the most critical worldwide issues. The paradigm of ICE vehicles proves to be the main obstacle to satisfy stringent environmental regulations, such as the Paris Agreement [1].

Another downside of ICE vehicles is the use of mechanic braking systems, where the kinetic energy is wasted in the form of heat by mechanical brakes. This constitutes a great inefficiency from an energy standpoint since there is no mechanism to regenerate the energy used. Alternatively, by employing electric energy storage systems, electric motors, and power electronic converters, it is possible to re-utilize the energy otherwise wasted during braking. This process is called regenerative braking or dynamic braking, in which an electric motor restores the energy to the batteries during braking. Electronic braking systems also have much higher energy and performance efficiency, than the conventional counterparts. Therefore, electrification of transportation is a paradigm shift and is one of the most promising solutions to achieve the global goal of reduced and cleaner energy consumption. In EVs, power electronics act as the connection between the energy sources, e.g., battery pack, and the motor. One of the main advantages of the power electronic systems is that they can provide high efficiency, opposed to combustion systems [2]. On top of that, EVs offer performance advantages such as higher responsiveness, i.e. faster acceleration. The accumulation of arguments in favor of EVs has been propelling the research of electric mobility technology and nowadays this is a well-disseminated concept. Considering this, the world is undergoing a transition of paradigm regarding transportation through electrification.

In regard to the EV market there are two tendencies. For one, there are models designed for commuting purposes with low battery weight and short-range. These are lightweight/low-power vehicles and they are optimized for low consumption and urban traffic. On the other hand, there are long-range electric cars with high-capacity batteries. However, this section of the market has a major disadvantage regarding range compared to ICE vehicles. Other EV disadvantages when contrasted with ICEs are a higher initial cost and time to refill. There are different proposals on how to solve these performance problems: One of the solutions involves the combination of energy sources, which is reflected in hybrid vehicles. The other suggestion is the replacement of the empty battery pack for charged ones instead of charging. With this, the charge time would be equivalent to filling up the tank in an ICE vehicle. Considering the limitations and advantages of

EVs, a good solution is the use of low-power vehicles such as EM. Electric motorcycles have the advantage of having low energy consumption and are optimized for urban driving since they are compact and easy to park. This reflects on reduced traffic when compared to bigger and higher-power vehicles, either electric or ICE based. Taking into account all the advantages of low-power vehicles, electric motorcycles prove to be an economic and environment-friendly solution for work commutes in an urban context.

## 1.2 EV Motors and Traction Controllers

Regarding EVs, the literature suggests a wide range of AC or DC electric motors such as synchronous and induction motors, and brushless DC (BLDC) and brushed DC (BDC) motors, respectively [3]. Each type of motor has different characteristics with specific advantages and drawbacks.

DC motors consist of a stator with a stationary field and a wound rotor with or without brush commutation (Figure 1.1 (a) and (b)). The main advantages of this type of motor are well-established technology, reliability, and simple and robust controls. The main disadvantages are low power and lower efficiency (85%) when compared with alternative technologies [3]. Despite having diverse types of excitation, most DC motors architecture is Permanent Magnets (PM) [3]. PM motors are characterized by their constant rotor magnetization and are called self-excited motors. PMs in the rotor induce high magnetic fields in the air gap, without excitation currents, leading to high power density. PM architecture can be present not only in DC motors but in AC motors such as synchronous motors. Excitation currents represent about half of the losses in the form of Joule losses for non-self-excited motors. Thus, PM motors are intrinsically more efficient, in comparison with separately excited motors, and require less cooling due to the lack of excitation currents.

Synchronous electric motors are AC motors in which at a steady-state, the rotation of the shaft is synchronized with the frequency of the supply current. They can be designed to operate over a wide torque-speed range with superior torque density and power density.

Induction motors are asynchronous AC motors in which the electric current in the rotor needed to produce torque is obtained by electromagnetic induction from the magnetic field of the stator winding [4]. The main advantage of IMs, in particular squirrel-cage motors (Figure 1.1 (c)), which are the most common, is it's construction simplicity. The rotor consists of a stack of laminated steel with short-circuited aluminum bars in the shape of a squirrel-cage. The magnetic field of the stator rotates at a slightly higher speed than the rotor. The slip between rotor and stator frequencies induces rotor currents that produce the motor torque [3]. An important factor when opting for an EV motor solution is the respective constitution, i.e. the presence or absence of rare-earth materials. Taking into account the electrification of vehicles it is required that the production of motors is scalable [5]. The recent issue of the rare-earth magnet price volatility is seriously questioning the adoption of PM motor drives [5]. In this scenario, induction motors are more suitable for replacing the rare-earth magnets with cheaper components [6]. Similar to induction motors, reluctance motors have gained attention due to the concern of price increase or shortage of magnetic material when

the EVs enter mass production. The rotor is also cheap to produce and not temperature sensitive [3].
The reluctance motor efficiency is equivalent to induction motors, whereas the efficiency remains high over a wide speed range [3]. The high ripple torque resulting in higher noise and vibrations is the main drawback. Considering all this, the cost of sustainability comes with a reduction in performance efficiency.

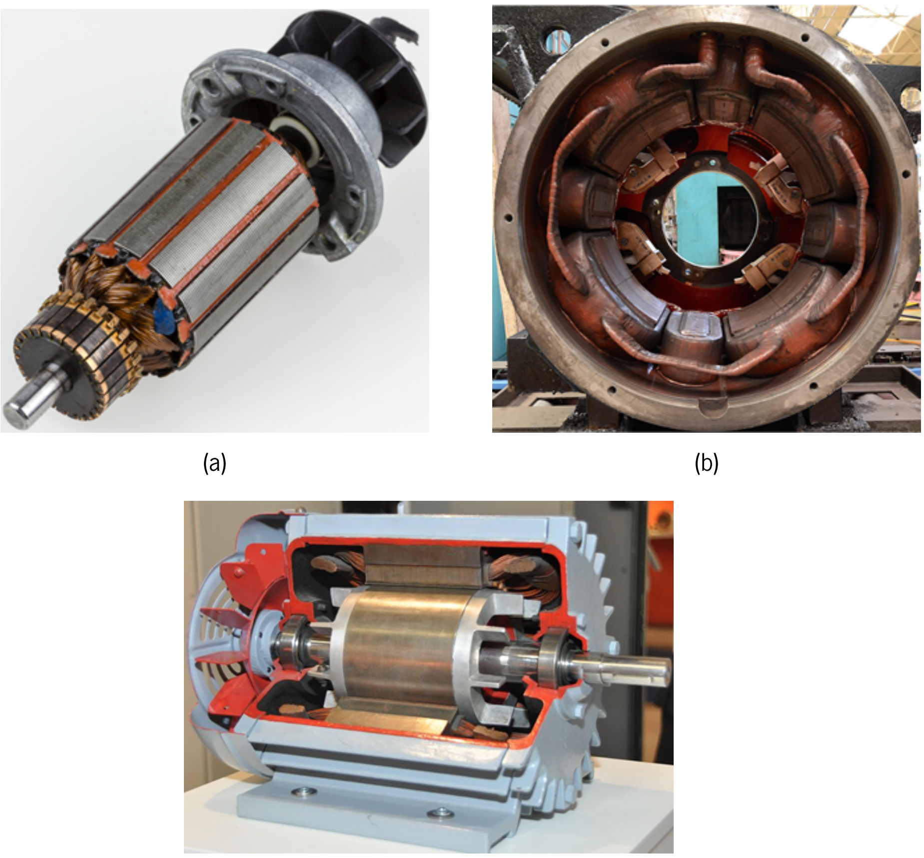

(a)

(b)

(c)

Figure 1.1: Photographs of electric motors: (a) Typical aesthetic of the rotor of a DC motor; (b) Example of the stator of a DC motor (no correlation with (a)); (c) Cut of a squirrel-cage induction motor (Adapted from [7, 8, 9].

With the use of electric motors electric traction systems can be implemented. Considering this, it is used a controller that operates the state of motor, e.g. acceleration and braking. Usually when opting for a motor is offered a conversion kit to operate it, which bring diverse accessories and a motor controller (Figure 1.2). In the market, there is a wide range of motor controllers, varying in terms of power, supply voltage, and functionalities. These motor controllers act as an interface for the user to control speed, rotation direction, regulating torque, starting, stopping the motor and it offers protection against overloads and electric faults. The controllers produced for motor applications employ power electronic converters allied with control methods. With this, the EV requires the integration of a motor controller similar to what was described.

Figure 1.2: Example of a motor controller produced by the company Piktronik.

For electric motors, by resorting to power electronics it is possible to recover energy during braking. This processing is called regenerative braking [10],[11]. Regenerative braking allows the mechanical energy from the motor's rotation to be converted into electrical energy that is returned to the battery. This process occurs when the brake is applied, the vehicle slows down and the motor works as a generator. While running in reverse the motor acts as a generator and thus charge the battery. However, while regenerative braking increases efficiency of the vehicle, it reduces the battery life expectancy, due to constant charge and discharge cycles [3]. On top of that it can only be applied when the batteries are bellow a specific charge due to the risk of overcharging. On the other hand, electric braking systems are used as functional braking, by controlling the motor torque. This operation is similar to braking with transmission or gear box and it is not suited for fast stops [12], [13]. Therefore, on EVs, it is still necessary to implement mechanical brakes in particular situations such as braking at higher speeds. Overall, regenerative braking optimizes driving in non-continuous/start-and-stop environments , since it is more frequently used in high traffic situations.

## 1.3 Battery Charging and Power Quality

The success of EV technology depends on the availability of EV charging stations. To meet this demand it is necessary to have a solid grid infrastructure of charging stations [14]. The interface between EVs and the power grid can be bidirectional. During EV battery charging the current direction is from the grid to vehicle, thus is called G2V (grid-to-vehicle). On the other hand, if the user decides to return or sell energy stored in the EV batteries, the vehicle can send back energy to the grid V2G (vehicle-to-grid). This process can have useful applications, such as in case of a power outage the vehicle can supply an installation, i.e. houses, or small stores. The advantages of a bidirectional charging system are that it supports charge from the grid, battery energy injection back to the grid, and power stabilization with adequate power conversion. However unidirectional charging is a logical first step because it limits hardware requirements and simplifies interconnection issues [14].

Aside from the interface between the EV system and the power grid, there must be provided charging control for the battery, e.g. keeping track of the charging and discharging rate, as well as the respective State of Charge (SoC). The use of Battery Management Systems (BMS) ensures that the battery is in a safe operating zone, to avoid material damage and allows the balancing of the charge of various batteries in the same bank, to guarantee an even charging process. On top of that BMS allows the monitoring of the battery state and the calculation/report of related data. With this, there are diverse topologies for converters that allied with control methods constitute a battery charger [14, 15, 16]. One application of BMS is the control of charging in response to time-of-use (TOU) price in a regulated market [17][18]. Charging control based on TOU reflects on a more economic battery charging by taking advantage of the price swing of electric energy along the day. With this, the user can charge the vehicle during low price energy hours, such as night hours, and resell energy surplus during peak consumption intervals. This occurs due to the discrepancy in energy consumption throughout the day. Smart-grid technologies such has TOU also benefits the power grid's health by flattening the energy consumption curve during the day. Figure 1.3 shows an example of a daily energy consumption curve.

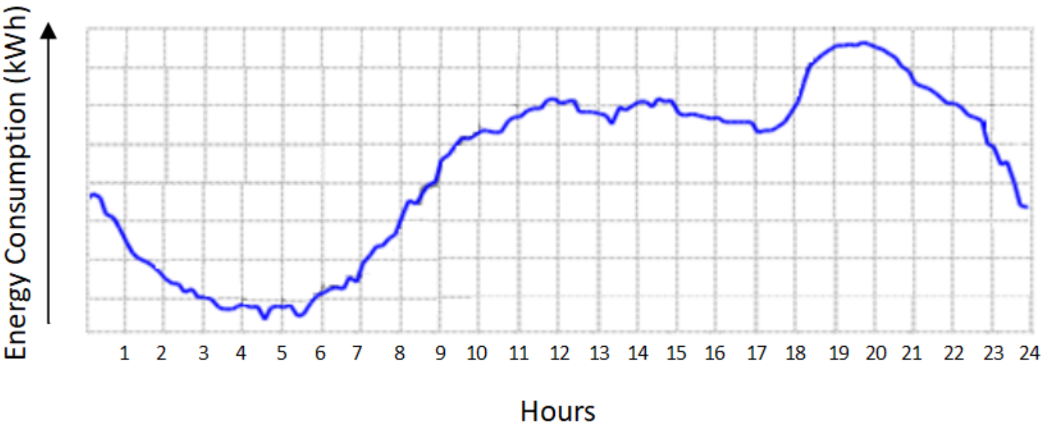

Figure 1.3: Typical power grid energy consumption throughout the day.

EV charging systems can be classified as on-board and off-board. Off-board chargers are the usual charging stations seen in public spaces and are directly connected to the EV batteries. Off-board chargers have their respective power converters placed between the power grid and the EVs. This charging solution is considered a DC-DC charger. On the other hand, on-board chargers, as the name suggests, are integrated on the EV and their topology is AC-DC converters [10], [19] [20]. The main advantage of on-board chargers is flexibility since they can charge an EV anywhere with a regular electrical outlet [21]. This is made possible to charge an EV at home with low investment, since charging stations are expensive and a regular domestic infrastructure is not prepared for this power level. Although, on-board chargers add weight to the vehicles, considering the necessity of on-board converters and have a slow charging rate. Another issue is the non-standardized communication protocol with the power grid since it varies according to the vehicle brand and model. Off-board stations have higher power (≈50kW) compared to on-board chargers (≈5kW), resulting in much faster charging. Off-board chargers also have a universal communication protocol regardless of the EV model [21]. Figure 1.4 illustrates an on-board charger versus an off-board charger.

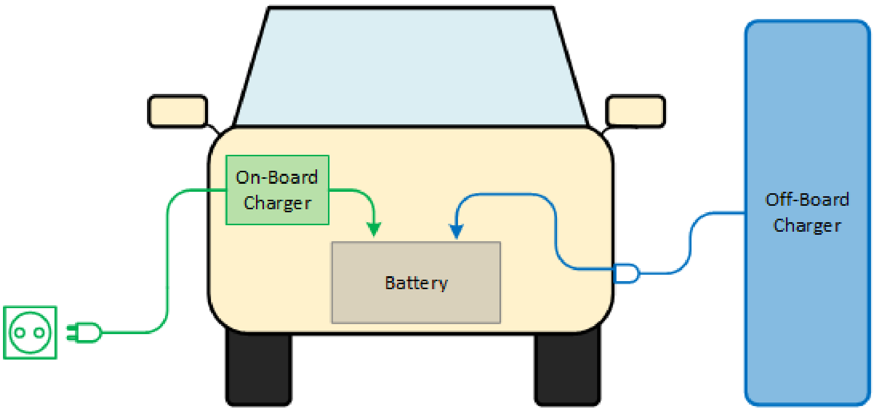

Figure 1.4: Comparison between an on-board charger and an off-board charger.

On the other hand, charging stations come with a multitude of challenges, including the integration of EV charging with the power grid. Literature regarding the topic of EV chargers mention that they have a negative impact on the power grid, due to being non-linear loads. Charging stations inject harmonics on the power grid and by being relatively big loads, they create overloads on the distribution network [14]. A harmonic translates to a sinusoidal component of a periodic signal containing a multiple integer frequency of the fundamental frequency [22]. The integer multiple is called the harmonic order. The presence of several harmonics in a given signal causes it to become distorted [23]. Figure 1.5 (a) represents a distorted current, and Figure 1.5 (b) illustrates the individual harmonic waves. The signal has, besides the fundamental, three harmonics, the third, fifth, and seventh harmonics.

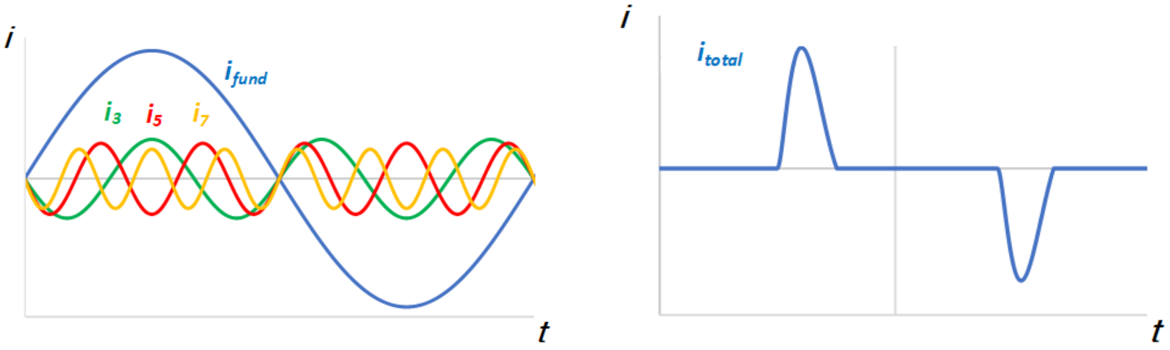

(a) (b)

Figure 1.5: Current wave with harmonic distortion: (a) Current breakdown in the respective frequency components; (b) Total Current.

The distortion of a waveform can be quantitatively measured through the Total Harmonic Distortion (THD) value, which can be calculated in absolute or relative terms. In absolute terms (total THD), the current THD corresponds to the effective value of the current of a signal excluding its fundamental component, as expressed by equation 1.1.

$$THD = \sqrt{\sum_{h=2}^{n} I_h^2} \tag{1.1}$$

In relative terms, THD represents a percentage value and can be calculated relative to the fundamental component (equation 1.2). This reflects the relationship between the amplitudes of the harmonics and the fundamental wave, so it may exceed 100%. This is the most common notation to quantify THD [22],[23] and is given by equation 1.2.

$$THD_{\%f} = \frac{\sqrt{\sum_{h=2}^{n} I_h^2}}{I_1}\,100\% \tag{1.2}$$

Because of the electric problems created by EVs, is important that their consumption of current is healthy for the grid. Therefore is opted for an AC-DC converter incorporating control techniques, which eliminate/reduce the harmonic distortion and correct the power factor. The literature presents diverse topologies and control methods for AC-DC converter solutions and battery management techniques. These are going to be covered further ahead in the appropriate section of this thesis.

## 1.4 Proposed System Prototypes

Based on the contextualization above, two prototypes are proposed, divided by 2 or 3 converter solutions, respectively. The 2-converter solution is composed by the motor and charger systems, where both have an interface with the battery bank (Figure1.6). Considering that both systems do not operate at the same time, the topologies are developed independently. The 3-converter solution has the two previous systems integrated and has an additional DC-DC bidirectional converter that acts as an interface for both motor driving and battery charging (Figure1.7). Accordingly, the advantages of this prototype are a standardized voltage on the DC-link that facilitates the implementation of the charger and motor converters. On top of that, the DC-DC converter integrates a charger control that can also function during motor operation, and not exclusively during charging, as opposed to the 2-converter counterpart. For the 2-converter prototype, the AC-DC and charger converter both compose the battery charging system, acting as the interface between the power grid and the battery. On the other hand, the motor converter is connected directly with the battery. The drawbacks of the 3-converter solution in comparison with the 2-converter counterpart are the necessity of implementing an additional converter and a control technique, adding complexity to the overall system. The synchronization with the charger and motor systems also increases the difficulty of implementation.

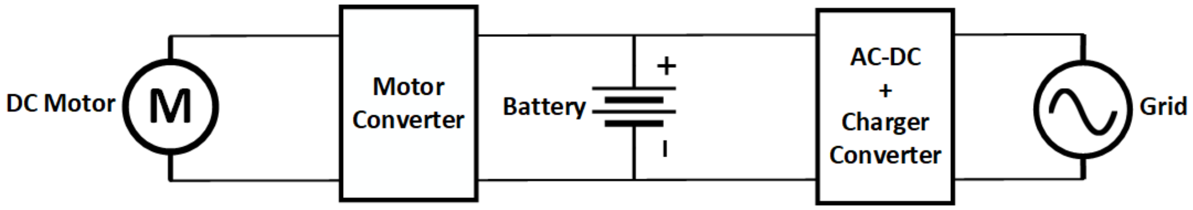

Figure 1.6: Proposed topology for the implementation of a traction and charging systems using 2 converters.

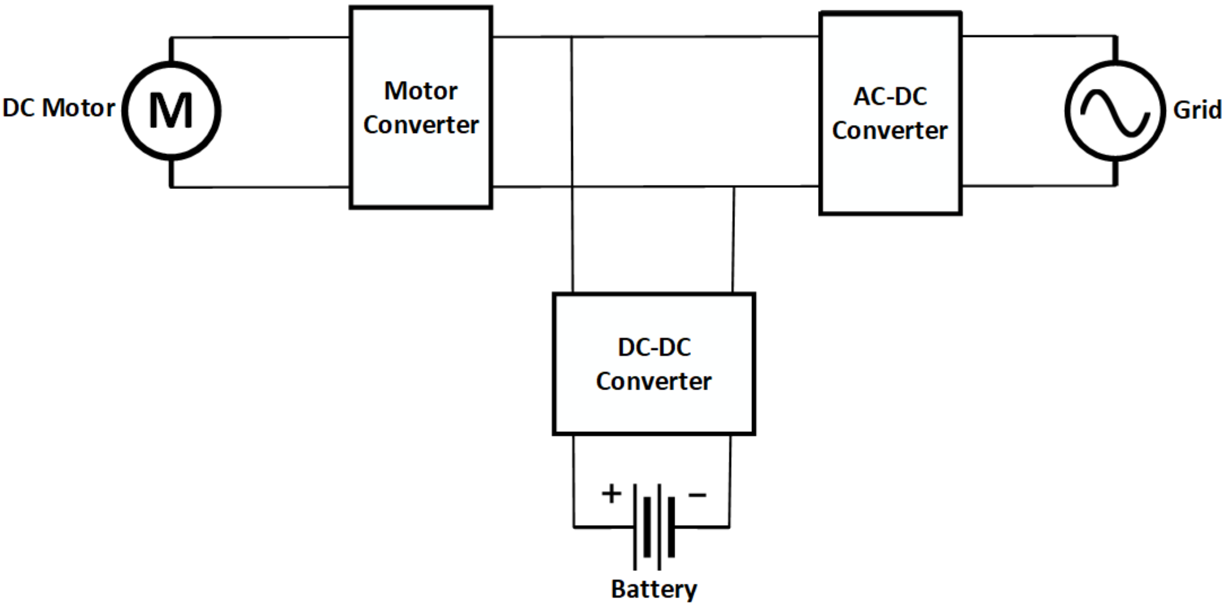

Figure 1.7: Proposed topology for the implementation of a traction and charging systems using 3 converters.

## 1.5 Motivation

Given the current energy and environmental problem, the motivation for this thesis falls under the premise of electric mobility. One solution is the use of small and low-power EVs, such as motorcycles, for short commutes in an urban context. The use of electric motorcycles reflects improvements on the urbanistic plan, regarding parking spaces and organization, as well as traffic fluidity. For this purpose it is necessary to develop regenerative braking and battery charging systems using power electronic converters, to optimize mobility in urban environments. Therefore, taking into account this necessity, the main motivation for this thesis project is the development of quintessential parts of any EV. However, the prominence of EVs creates new challenges for the power grid. Aside from improvements on the electric infrastructure it is necessary to develop chargers that reduce the impacts on the power grid, being another motivation for implementing a battery charger system. Therefore, this project is ambitious in the sense that it is implemented both charging and traction systems, core to any EV. Allied to the motivations mentioned above, this thesis is multidisciplinary, since knowledge in various areas of electronics is required, especially power electronics, micro-controller programming, digital control, and Printed Circuit Board (PCB) design.

## 1.6 Objectives

For the motor converter, which integrates the traction system, it is established the goal of elaborating a torque control, that operates similarly to practical vehicles the user inputs a current/torque using a pedal. The charger system's AC-DC converter must be able to compensate current harmonics and regulate a low ripple DC voltage on the output. On top of that, the charger should provide a steady charging current set by the user, and considering the battery state of charge is necessary to automatically turn off the converter operation.

Thereby, the objectives set for this thesis are:

- State of the art research concerning electric motors, in particular DC motors, the respective driving systems, and commonly used charging topologies. With this, the first objective is to elaborate a market study covering converter topologies for power electronics and control techniques that are best adjusted for the development of traction and charging systems for an EV;
- Development of simulation models, to validate the converter topologies and control algorithm studied for the developed system. The simulations conducted should demonstrate the correct functioning of a DC motor with given characteristics as well as battery charging during regenerative braking. On the side of the charger system, it is expected to observe a current consumption with low THD, DC voltage regulation, and constant charging current on the batteries;
- Implementation of the hardware, for the control systems and power systems. For this, it is necessary to research the hardware required and design the circuits taking into account the disposition of the components and board inter-connections;
- Implementation of the software and coding to then be applied to a microcontroller that processes the control methods;
- Experimental validation of each part that constitutes the proposed solution. From signal acquisition and control processing to the operation of each power converter and the conduction of experimental trials to the systems prototypes.

## 1.7 Organization and Structure

On the first chapter is covered the problem and the context of this thesis, introducing the current environment and energy problems. Besides, the motivations and the objectives to solve these problems are referred, as well as why EVs, in particular, EMs are a good solution.

On chapters two and three bibliographic research is made about common converter topologies as well as control methods for the charger and motor systems, respectively. The second chapter presents solutions for AC-DC, DC-DC converters, in the context of a DC-link regulation and battery charging. On top of that, control methods applied to the topologies proposed are presented according to the bibliography. The third chapter introduces the most common DC-DC converters for motor drive applications. On the other hand, torque control techniques with a pedal/accelerator interface are discussed.

In chapter four is simulated the proposed topologies for both the charger and motor systems and the respective controllers. Furthermore, the results of the simulation are presented and discussed, projecting what is expected for practical tests.

Chapter five has the purpose of introducing the implementation of the control and power systems. This chapter describes in detail the design of the converters and all circuits in PCB, as well as the sizing of the components.

In chapter six the experimental results of the converters are presented to validate the implementation.

At last, in chapter seven the conclusions are reported and presented the final thoughts of the overall implementation. Additionally, suggestions for future work and possible improvements are made.

# Chapter 2

# Charger System - Power Factor Correction and Battery Charging Solutions

## 2.1 Introduction

As referred in section 1.3 EVs battery chargers are classified as on-board or off-board chargers. Taking both solutions into account and considering that currently most plug-in EVs use single-phase on-board chargers [14], this thesis will cover the single-phase on-board solution. Therefore the charger system is integrated into the EV and is composed of an AC-DC converter. The function of a rectifier is to provide a stable DC-link voltage and synthesize a power grid current with low THD. With this, the converter should also act as Power Factor Corrector (PFC), compensate current harmonics and maintaining the grid's power quality. This chapter covers the requirements to make the interface between the EV DC system, i.e synchronization with the power grid and DC-link regulation, the most common topologies and respective control theories. For this purpose, the most typical single-phase rectifiers are full-bridge converters [24]. Depending on the control and structure implemented, the solutions can be a regular a Diode Full-Bridge (DFB) or an Active Rectifier (AR), which is a full-bridge of controllable semiconductors. Along this chapter is going to be drawn the differences and similarities between these two topologies.

## 2.2 Diode Full-Bridge Rectifier and PFC Solutions

In the simplest case, the AC-DC converter can be unidirectional using single-phase diode rectifiers. Usually, the topology used is a DFB that rectifies the grid voltage and producing at the output (or DC-link) a constant DC voltage with a certain ripple. The ripple is minimized by the DC-link capacitor, where the ripple is lower with a higher capacitance. On top of that components referred is also present a inductance after or before the DFB reduce the power grid current noise [24, 25, 26]. Passive as the name suggest do not integrate any control technique, thus is not possible to regulate the output DC voltage nor apply power factor correction and harmonic compensation to the absorbed current. Considering this, simple DFB rectifiers are not suitable for applications where is required a specific DC-link voltage and where energy quality is a concern. Figure 2.1, illustrates the previously detailed DFB rectifier.

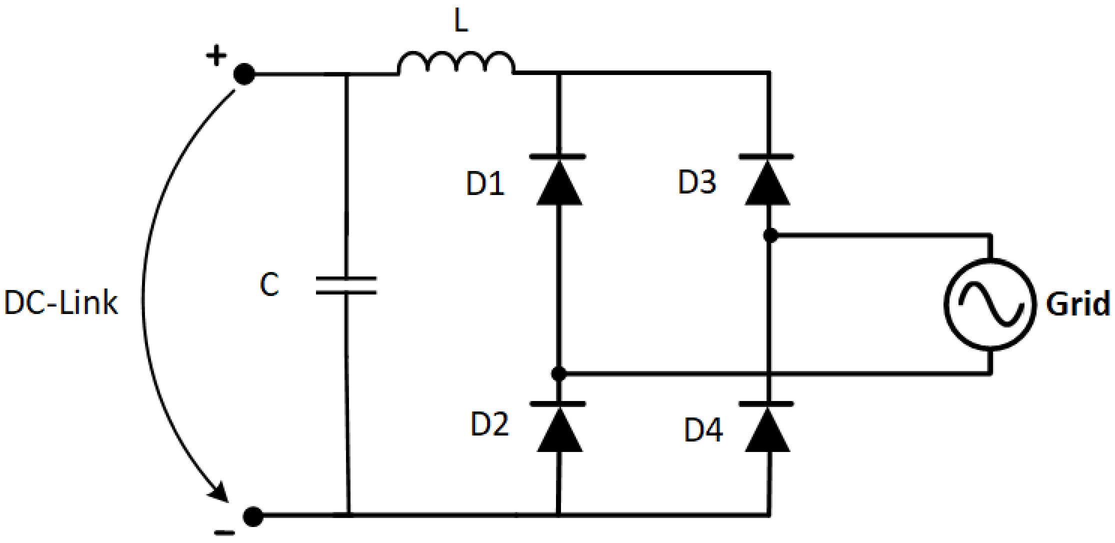

Figure 2.1: AC-DC diode full-bridge rectifier schematic.

The low complexity of the DFB rectifier must, however, be weighed against the disadvantages of relatively high effects on the power grid and an unregulated output voltage directly dependent on the power grid voltage level [25], [24]. Considering converters behave as non-linear loads, they absorb currents with high harmonic content which in turn cause distortion of the current waveform and contribute to a low power factor [25], as shown in Figure 2.2.

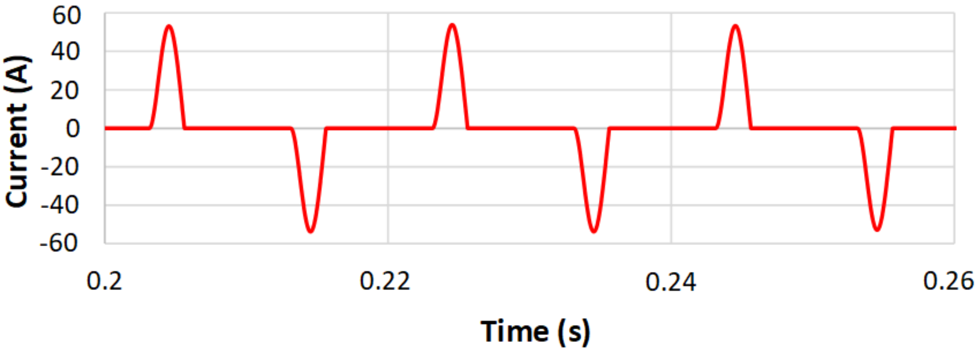

Figure 2.2: Power grid current absorbed by a DFB rectifier.

To achieve a sinusoidal power grid current with THD<$5\%$ (required for the distribution grid), is necessary to implement a PFC converter. Therefore, in addition to the previous system, are implemented boost or buck converters (Figure 2.3), allied with current control methods, that synthesize the current needed to attain the desired DC-link voltage and also eliminate the grid's harmonic content [24], [25]. This proves to be a simple and reliable solution considering that is only needed to control one semiconductor. With this, the converter requires two closed-loop controls. One to obtain the reference current for a specific DC-link voltage and the other to regulate the current consumed. For this converter and regular full-bridge AC-DC topologies, the minimum voltage necessary to control the DC-Link is the peak instantaneous grid voltage for single-phase systems. On PFC solutions are commonly used boost converters to regulate the DC voltage, remove current harmonics and correct the power factor. Therefore, in most PFC converters the output voltage is elevated to values higher than the peak grid voltage.

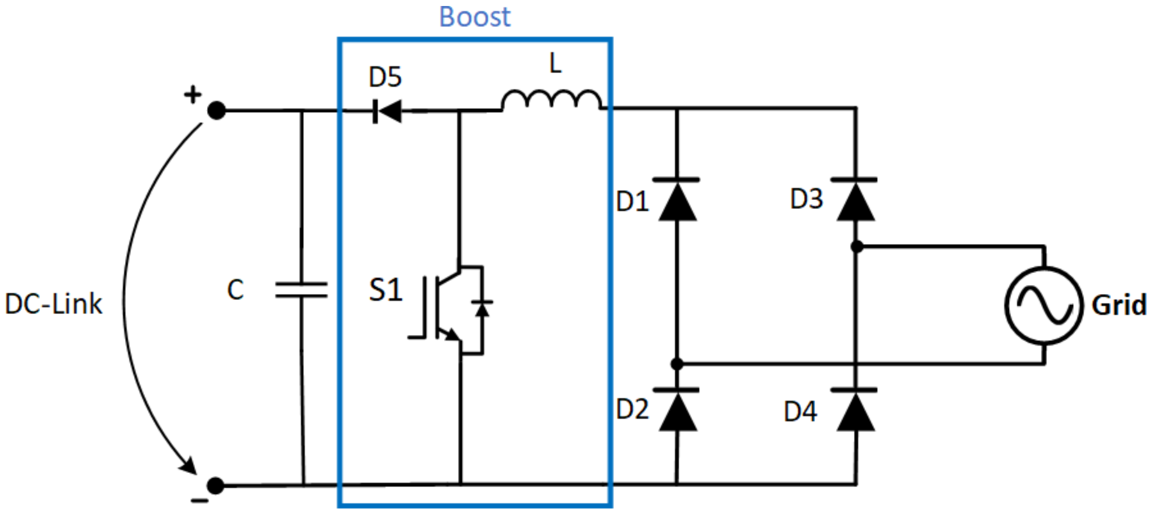

Figure 2.3: Electric schematic of a PFC boost rectifier.

With the implementation of a DC-DC converter, the current absorved has a lower harmonic content than previously, as shown in Figure 2.4. Is also possible to observe that the peak value of the current grid is greatly reduced, posing another advantage in terms of overall safety.

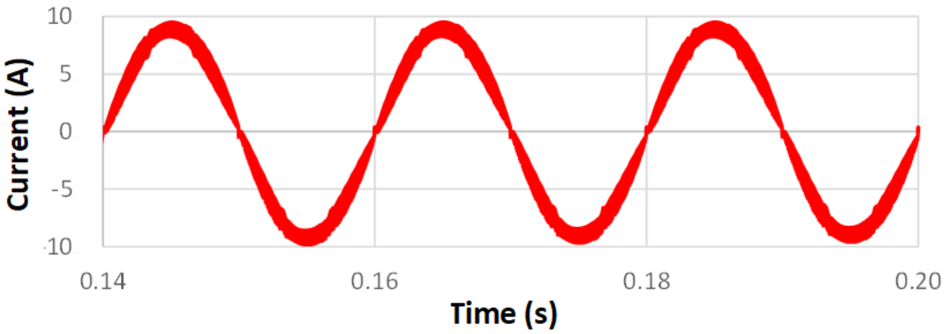

Figure 2.4: Grid current absorbed by a PFC boost converter.

## 2.3 Full Active Bridge Converter

Full active bridge converters are composed of four controllable semiconductors and the respective anti-parallel diodes, as per Figure 2.5. Allied with a control algorithm these converters act as a PFC, eliminating harmonic content and other grid problems and also regulate the DC-link voltage. These converters use Pulse-Width Modulation (PWM) techniques to control semiconductors, such as IGBTs, to dynamically change the input current waveform and thus reduce the harmonic distortion, leading to an increase of the power factor close to the unit [27], [28]. This is an important aspect since without any further electronics (e.g buck or boost converters on the output), is possible to control the DC-link voltage to a constant value independently of the grid voltage since it can act as a boots-buck converter. However a converter stage on the output side can be dimensioned to narrow the voltage range, to values lower than grid peak [24], [25]. Another characteristic of this converter is to allow a bidirectional power flow, due to the existence of the freewheeling diodes placed in anti-parallel with the respective IGBTs. Thus allowing operation as an inverter or a rectifier. During the positive and the negative semi-cycles the converter operates differently. Regarding the former, the semiconductors S1 and S4 are ON (closed) and S2 and S3 are OFF (open) and the bridge output voltage is $+V_{dc}$. During the negative semi-cycle, to obtain a negative output voltage (-$V_{dc}$) is necessary that S2 and S3 are ON and S1 and S4 are OFF. For the remaining combinations such as S1/S3 ON or S2/S4 ON the voltage output is 0 V.

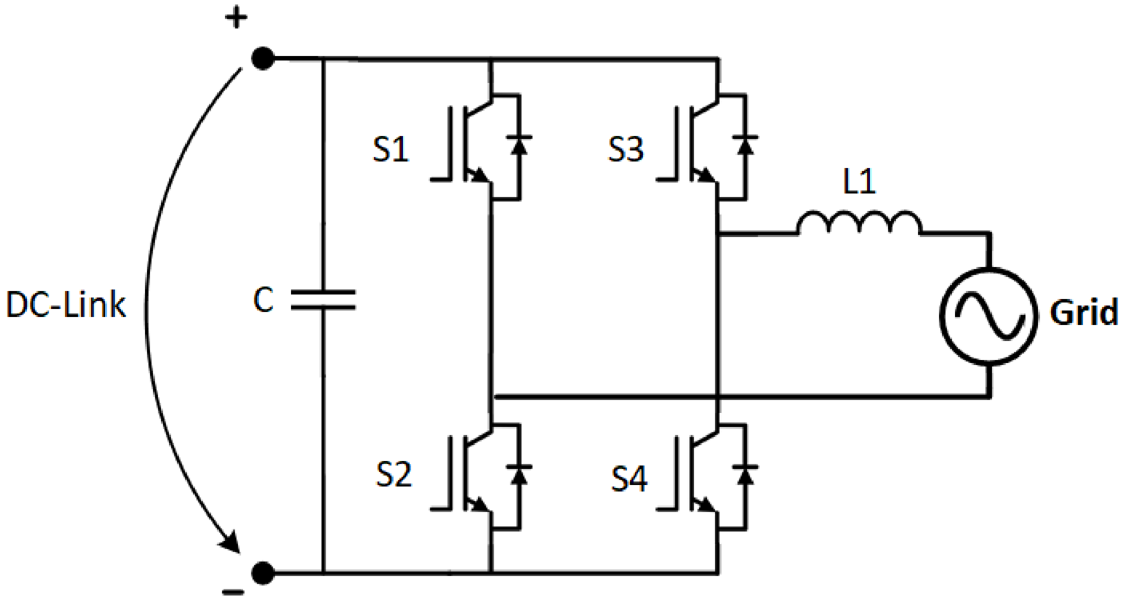

Figure 2.5: Electric schematic of an Full active bridge converter.

It is important to note that for this topology, IGBTs of the same leg (S1 and S2 or S3 and S4) cannot be activated at the same time to avoid short-circuiting the capacitor. This results in additional development hurdles, such as dead-time implementation, and makes the control system more complex in comparison to the passive solution. On top of that, during operation any defects on the dead-time result in damage on the semiconductors if there are no additional safety measures implemented. Another disadvantage of this technique is the need for the controller to generate at least four PWM signals as opposed to one for the passive converter.

## 2.4 Synchronization with the Power Grid

The synchronization of the motorcycle charging system and the power grid for control purposes is required. Usually, the signal obtained from the power grid is distorted due to harmonics created by other nearby electric systems or the power grid itself [29]. With the implementation of a Phase-Locked-Loop (PLL) algorithm it is possible to obtain a perfectly sinusoidal reference signal in-phase with the grid's voltage [30], [31]. A PLL algorithm is a feedback system, where the output and the input signals have synchronized instantaneous frequencies. There are several different algorithms, but they consist essentially of three main parts, the Phase Detector (PD), the Loop Filter (LF), and the Voltage-Controlled Oscillator (VCO) [31], [32]. The PD compares the phase of the input signal with the phase of the output signal given by the VCO. The PD output is an error signal that shows the phase difference between the input signal and the signal from the oscillator. The phase error signal is then filtered, by a low-pass filter, to obtain the mean value of the signal, which is then applied to the VCO. The VCO adjusts the output signal frequency until it is equal to the frequency of the input signal. Under these conditions, the phase error is constant and as a result, a constant signal is applied to the oscillator, which allows the frequency synchronization to be maintained (phase capture) [31], [32]. In Figure 2.6 is presented the a simplified block diagram of the description above.

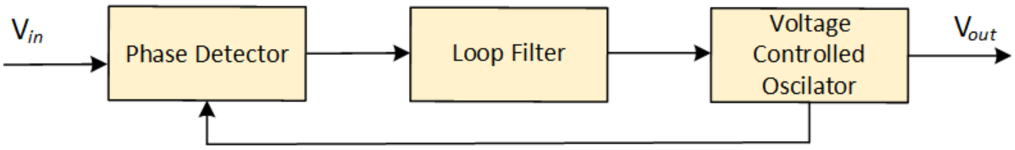

Figure 2.6: Block diagram of a typical PLL algorithm.

## 2.5 DC-Link Regulation

An important characteristic of single-phase rectifiers is the pulsating power transfer that occurs from the AC side to the DC-link, which generates a voltage ripple on the latter. This ripple has twice the line frequency (100 Hz) when the input voltage and current are sinusoidal [26]. The capacitor placed on the DC-Link attenuates the low-frequency ripple, where a bigger capacitance, improves the attenuation in detriment of a slower voltage stabilization [24]. During the start of DC regulation, due to the DC-link capacitor, in-rush currents appear on the converter AC side. In-rush currents reach up to multiple times the nominal value and can damage the converter, destabilize the controller and consequently have a negative impact on the DC-link voltage evolution [31]. For this reason, during the pre-charge of the DC-link capacitor, are used bypass resistors in order to attenuate in-rush currents. The bypass resistor activation/deactivation is made by means of a switch that receives the signal from the controller. Once the voltage of the DC-link reaches a sufficiently high value, the control system is activated and pre-charge resistor is bypassed.

## 2.6 AC-DC Rectifier Control Techniques

To regulated the DC-link voltage and absorb a sinusoidal power grid current with low harmonic content, is required control techniques allied to the topologies presented. With this in mind, the following sections detail various control techniques viable for AC-DC applications.

### 2.6.1 Proportional-Integral Control with SPWM technique

The Proportional-Integral (PI) is a widely used control on PWM converter applications, such as the AC-DC rectifier covered [33]. This current control technique is intended to make a measured current follow a given reference with the least possible margin of error. A PI control with Sinusoidal Pulse-Width Modulation (SPWM) is considered linear as error compensation and voltage modulation are separated. Therefore, a fixed switching frequency can be obtained, resulting in a well-defined harmonic spectrum. The PI current control has an input variable, the error, $i_{error}$ resulting from the difference between the reference current, $i_{ref}$, and the measured current, $i_m$. The resulting output is a SPWM signal, a sinusoidal reference that is compared to a triangular carrier wave. This results in a PWM signal with a specific duty-cycle, imposed by the sinusoidal reference previously obtained. The block diagram respective to the PI current control is presented in Figure 2.7.

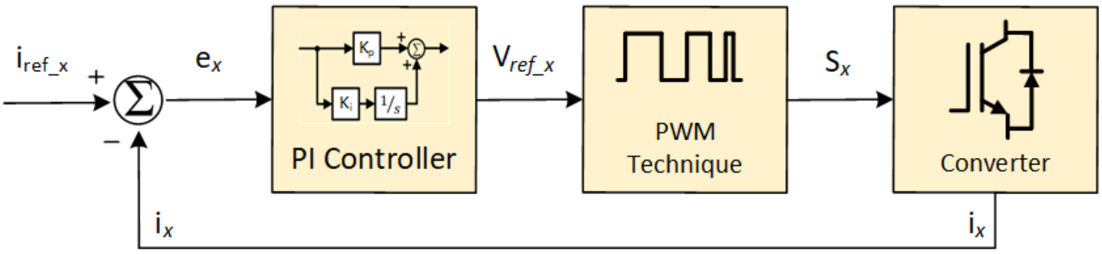

Figure 2.7: Block diagram of the PI control action, the respective SPWM technique.

By observing this diagram, the transfer function of the PI controller is easily obtained, in the domain of Laplace, G(s), represented by equation 2.1. A standard PI controller is also known a two two-term controller where $K_p$ and $K_i$ are the proportional and integral gains of the controller, respectively. The integral portion is corresponding to the sum of previous errors which translates into an integral or $(\frac{1}{s})$ in the Laplace domain.

$$G(s) = k_p + \frac{k_i}{s} \tag{2.1}$$

Understanding the influence of the parameters $K_p$ and $K_i$ on the control is crucial to obtain a successful tuning of a PI controller. With that being said, the proportional action allows the reduction of the permanent regime error at the expense of a greater tendency to oscillation. Increasing the proportional gain allows this error to be reduced, however, the oscillation as a result of this increase will be greater, and if $K_p$ is increased too much it may lead the system to instability. The integral action, on the other hand, eliminates the error in the permanent regime. The system tends to oscillate with the increase of $K_i$, while, the respective decrease allows an increase in stability. The individual effects of these two-terms a closed-loop control system are summarized in Table 2.1.

In addition to allowing as little delay time as possible, the gains of the controller should be selected so that the amplitude of the reference voltage produced is always lower than the amplitude of the triangular wave in the PWM technique in order to avoid over-modulation. On the other hand, they should be selected so that the error is as small as possible, without causing instability to the system.

Table 2.1: Effects on the PI control resulting of the increase of each a gain independently.

| **Parameter** | **Rise Time** | **Overshoot** | **Stability** | **Stabilization time** | **Steady-state error** |
|---|---|---|---|---|---|
| $K_p$ (Increase) | Decrease | Increase | Degrade | Small change | Decrease |
| $K_i$ (Increase) | Decrease | Increase | Degrade | Increase | Eliminate |

### 2.6.2 Predictive Control with SPWM technique

The predictive control technique is based on the electric model of a system. By analyzing a circuit is possible to calculate the converter input voltage necessary to obtain the desired output current. A system consisting of a DC-AC voltage source converter connected to the grid is modelled by a inductor, which is the coupling inductor ($L$). Therefore, the converter output voltage ($V_{conv}$) must be equal to the grid voltage ($V_g$) minus the voltage drop in the inductor ($V_L$), as represented by the following equation:

$$V_{conv} = V_g - V_L \tag{2.2}$$

Ignoring the inductor's Equivalent Series Resistance (ESR), the previous equation can be simplified, as follows, where $i_{conv}$ is the output current of the converter:

$$V_{conv} = V_g - L\frac{di_{conv}}{dt} \tag{2.3}$$

This control is based on current feedback and the current error $i_{error}$ is giving by the difference between the reference $i_{ref}$ and the measured current $i_g$, thus the equation 2.3 can be simplified in :

$$V_{conv} = V_g + L\frac{di_{ref}}{dt} - L\frac{di_{error}}{dt} \tag{2.4}$$

The control is processed digitally, therefore is necessary to transition to discrete-time and since the sampling frequency is superior to the frequency of the signal, it is considered that the derivative error evolution is practically linear. Taking into account the reduced ripple of the output current, due to a high switching frequency of the power semiconductors, the derivative of error takes on the value of $i_{error}$ at each instant $k$. Thus, equation 2.4 can be written as equation 2.5, where $T_s$ represents the sampling period and $\Delta i_{ref}$ the variation of the reference current.

$$V_{conv} = V_g + L\frac{\Delta i_{ref}}{T_s} - L\frac{i_{error}}{T_s} \tag{2.5}$$

After transforming equation 2.5 to discrete time is obtained the following equivalence:

$$V_{conv} = V_{ref}[k] = V_g[k] + \frac{L}{T_s}(i_{ref}[k] - i_{ref}[k-1] + i_g[k]) \tag{2.6}$$

The block diagram of the predictive current control technique is shown in Figure 2.8. For this technique is required the measurement of current the grid current and voltage values.

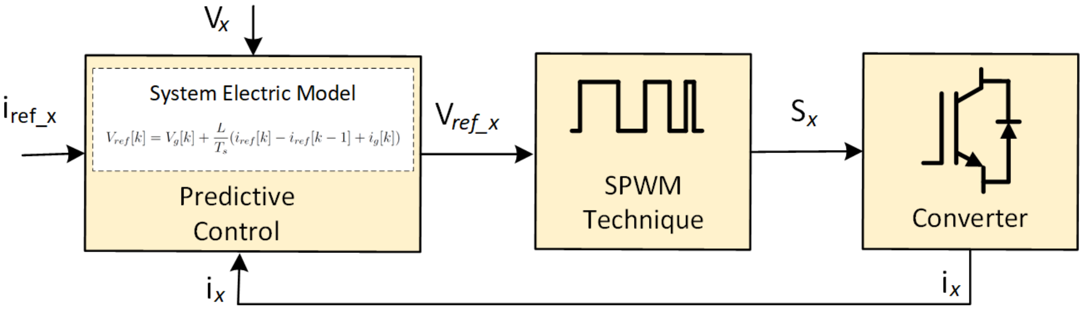

Figure 2.8: Block diagram of the predictive control and the respective SPWM technique.

Comparatively to the PI control technique, the predictive control does not require gain adjustments, furthermore, this method is capable of producing faster responses. However, since the predictive control is based on the electric model of the system, the technique's efficiency is dictated by the quality of the electric circuit. Therefore the predictive control is very sensitive to parameter errors, i.e. in practice the value of $L$, can have variance due to the inherent inductance of cables and over components.

## 2.7 Battery Charging and Charger Topologies

To regulate and control the charging rate and state of the batteries is required some form of control. There are diverse charging methods that improve energy efficiency, such as charge scheduling, V2G energy return, and other smart applications, such as the integration in micro-grids [17]. However, the essential parts of battery chargers are controlling the charging current while motorizing the battery's conditions, such has SoC and temperature.

To evaluate the SoC it can be measured the battery Open Circuit Voltage (OCV) [34]. The OCV is the voltage measured on the two battery terminals ($V_{oc}$) when disconnected from loads or sources and no current flow. A specific OCV corresponds to a different SoC percentages, depending on the battery characteristics.

Regarding the type of battery used, the most common for EV applications are lithium-ion (Li-ion) batteries [35],[36]. Li-ion batteries are well suited for transportation applications, due to their high energy/power density ratio, slow self-discharge, high cycle life [35] [37]. However, as a consequence of the electrochemical characteristics of Li-ion batteries, they are required to work within a relatively narrow temperature and voltage windows [38]. Research areas for Li-ion batteries include extending lifetime, increasing energy density, improving safety, reducing cost, and increasing charging speed.

Figure 2.9 pictures a Li-ion battery bank of 1.6 kWh, 40 V and 40 Ah battery, produced by the Varta Company, where can be seen the connections between each battery unit.

Figure 2.9: Photograph of a 1.6 kWh Li-ion battery bank produced by the company Varta. Reproduced from [39]

.

To simulate and analyze the behavior of a battery is necessary to represent the respective equivalent model. In Figure 2.10 are described the electric parameters of a generic battery model. With this, is taken into account the inherent battery self-discharge, which corresponds to a resistor ($R_{SD}$, usually >1 M$\Omega$), a capacity $C_{bat}$, that translates to the energy storage element, an internal resistance ($R_{bat}$) and the initial voltage ($V_{bat}$). The battery model then behaves like a capacitor and the respective parameters influence the charging speed [34].

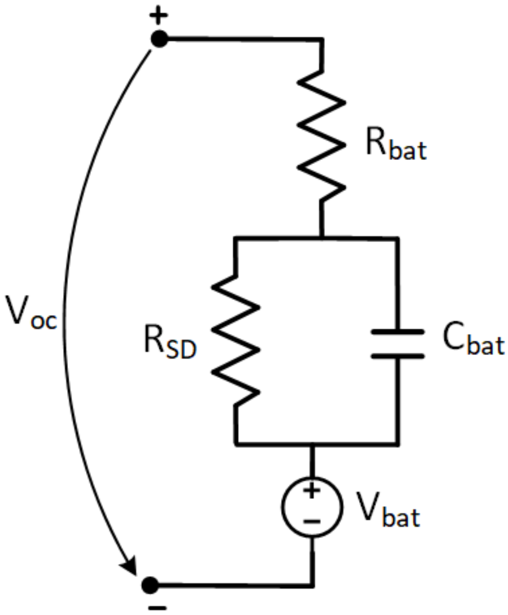

Figure 2.10: Equivalent model of a generic battery.

In order to implement a battery charger is required a power converter, and considering that the EV system is DC, the options are DC-DC converters such as buck/boost [14]. Considering that the implemented charging system only supports G2V, the battery converter is unidirectional. On top of that, the battery voltage is lower than the DC-link voltage, therefore, is opted to implement a buck converter in order to apply energy storage controls [14]. With this, is added an additional DC-DC buck converter to the previously mentioned AC-DC topology, resulting on the schematic presented on Figure 2.11. Therefore the DC-link is effectively the point between the boost and the buck converter.

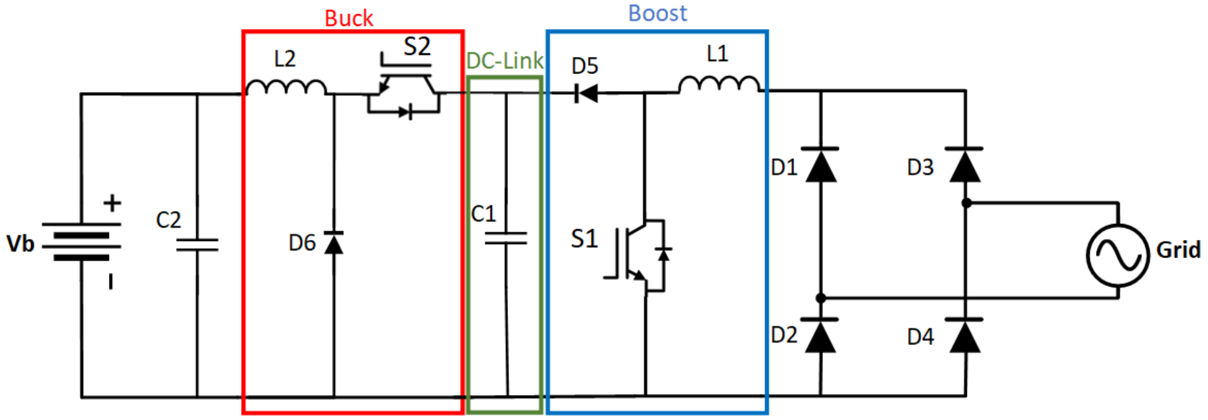

Figure 2.11: Schematic of the charger topology for grid-battery interface.

To ensure a safe charging process are implemented charging protocols such as CC-CV, and CC-CT (Constant Current-Constant Voltage, and Constant Current-Constant Temperature, respectively). These protocols are usually implemented on Li-ion batteries. The CC-CV is the most common protocol [40],[41] and consists of charging the batteries with a high and constant current and a varying voltage when the SoC is low. In later stages, when the SoC reaches a specific value the charging strategy switches to maintain a constant voltage. During this stage, the charging current is much lower as well as the SoC evolution. However, due to the electrochemical characteristics of the EV battery, the charging current decreases along with the increase of battery SoC, which results in a significant reduction of the charging power. This leads to an increase of the charging time at the ending stage [38]. Thus, CC-CV charging is suitable for applications where the charging time is not a concern, e.g., charging at terminal stations [42]. The CC-CV charging process detailed above is illustrated in Figure 2.12, where are shown the battery voltage, current and SoC waveforms.

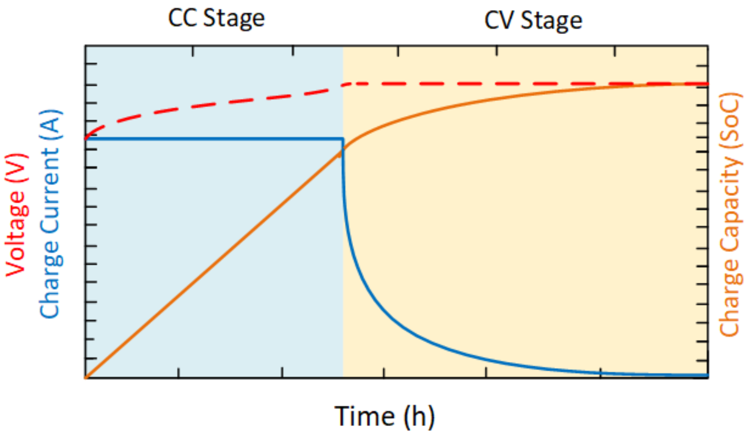

Figure 2.12: Battery current, voltage and SoC curves during CC-CV charging.

On the other hand, with the rising in temperature and the risk flammability being one of the main disadvantages of Li-ion batteries, the CC-CT protocol is also a viable solution regarding safety [41]. Similarly to CC-CV when the batteries SoC is low, they are charged with constant current independently of the temperature. When the Li-ion battery's SoC is high enough the charger prioritizes maintaining a constant temperature and consequently reduces the charging power [41]. The control of temperature is made by regulating the charging current considering that the former is proportional to the battery dissipated power, which in turn is given by equation 2.2.

$$P_d = R_{bat}\, i_{bat}^2 \tag{2.2}$$

A simpler method than CC-CV and CC-CT is plain CC over the whole charging process. This provides a much faster charging but has the disadvantage of not being able to fully charge the batteries due to the risk of overheat and overcharge [38], [42]. Therefore when the SoC reaches a determined value the charger is turned off. This is a more simple approach to battery charging in the context of the present thesis. In this method, the charger has a PI control, where is set a reference current. Similarly to the PI control described in section 2.6.1 the controller output is a PWM wave with a varying duty-cycle that activates the IGBT on the buck converter (Figure 2.11) . The reference current is constant and can be regulated throughout the charging process, according to the user input. Comparing this method with the CC-CV protocol, the latter can be implemented with two PI controllers, one for the CC stage then another for the CV stage. The two PI controllers are implemented independently and is made a transition between the current PI control to the voltage PI control upon reaching a specific SoC. With this, the main difference between the CC-CV and plain CC charging is the necessity of only one PI control on the latter to control the charging current. On top of that the stage transition poses an additional development hurdle.

## 2.8 Chapter Conclusion

This chapter described the essential concepts for the interface between the motorcycle and the power grid as well as the theory of AC-DC power converters. Nonetheless it was described the requirements to implement an EV charger and solutions to eliminate the harmonic currents. With this in mind, it was presented two full-bridge topologies for AC-DC converters, and it was drawn the differences as well as advantages/disadvantages between these solutions. A more simple full-bridge topology is the PFC boost converter, which is a unidirectional converter and only allows G2V, whereas the active converter also enables the V2G option. The main difference between the PFC boost solution and the active converter is the complexity required, reflected in the number of semiconductors to be controlled (one semiconductor and four semiconductors, respectively). On the other hand, it was presented current control techniques to be integrated by these topologies. The control techniques presented are used to synthesize a sinusoidal input current and to regulate the DC voltage on the output. The current control techniques described were PI control and predictive control both with SPWM technique, which produce a sinusoidal reference. These control techniques are given the referred sinusoidal reference current and enforce that the regulated current follows this reference. The PI controller determines the instantaneous error, as well as the the sum of previous errors, and sequentially these components, are multiplied by $k_p$ and $k_i$ gains. These gains act as weights that affect the control behavior therefore is necessary to adjust them accordingly. The adjustment of these gains is the main disadvantage of the PI control. The predictive control is based on the model of the electric circuit. To arrive at the output, an equation is required to analyze the circuit and transition the mathematical model to discrete-time so it can be processed digitally. While the predictive control holds the advantage of not requiring gains, its efficiency is dependent on the accuracy of the parameters and variable measurements. Regarding battery management, it was discussed the implementation of a DC-DC converter that applies a charging protocol. According to literature the most common DC-DC converters for this application are buck, boost, and buck-boost converters. The main advantage of the buck-boost converter is being bidirectional and consequently being able to manage the battery during motor driving. On the other hand, since the battery voltage is usually lower than the DC Bus voltage is used the buck converter over the boost solution. As referred above the two most used charging protocols are CC-CV and CC-CT, where both charging processes start with the control of a constant current and upon reaching higher SoC is made a transition to CV or CT controls, respectively. The main drawback of these solutions is the high charging time during the last charging stages. However, is also possible to charge the battery with plain CC until a specific SoC and turn off the charging process. This lowers the time of charging but is more unhealthy battery-wise since the battery can not be fully charged.

# Chapter 3

# DC Motors - Motor Operation, Topologies and Control Methods

## 3.1 Introduction

Electric motors enable mechanical loads to be driven by converting electrical energy into mechanical energy. Low energy losses resulting from this conversion process allow electric motors to have high energy efficiency when compared to ICEs. Electric motors can be supplied with DC or AC current, divided them in two groups, respectively. Both DC and AC motors are suitable to be implemented on an EV, however, taking into consideration the literature researched, this thesis is going to cover the DC solution [10],[11],[43], [44]. The flexibility obtained from BDC motors, associated with the control simplicity, and the diversity of DC converters available, determines a decisive advantage of these engines over the AC in cases where high torques or wide speed variations are required, such as in EVs [10]. Regarding BDC motors, they can be classified as Brushed (BDC) or Brush-less (BLDC) motors. The construction and operation principles are similar for both motors, and the main difference between BDC and BLDC is that the first requires mechanical commutation of the windings as opposed to electrical for the latter. This contrast implicates advantages and disadvantages for both solutions. BDC motors present more simple control methods, where is only needed a DC voltage supply, resulting in the most undemanding solution from a user perspective and it has a low cost of construction, however, they require regular maintenance to replace the commutation brushes [3], [45], [46]. BLDC offers higher efficiency, lower maintenance, and higher life expectancy, but at the same time, the respective converter and control are more complex and expensive [45]. Taking into account the context of this dissertation and considering a simplified and more robust solution is opted to use a BDC motor. Throughout this chapter is described the principle of operation of a BDC motor, where is presented the respective mechanical constitution, magnetic field generation in the stator, and the production of torque in the rotor. Finally, are showcased the most common converters to supply and control the motor and the respective methods of braking.

## 3.2 BDC Motor Constitution and Principle of Operation

The BDC motor consists of several elements with the stator, the rotor and brushes being the main constituents. In the fixed part of the motor, called the stator or field, there are wrapped coils creating windings (field windings) composing the magnetic poles.

The rotor or armature is placed in the inner part of the motor, between the poles created by the stator. On the rotor, there is a cylindrical core with slots, in which conductors are arranged in grooves along the surface creating the armature windings. These conductors form spirals, which are connected to the segments of the commutation ring that exists on the rotor shaft. The electrical connection of the armature to the outside of the motor is made by brushes, making contact with the commutation ring. The commutation ring consists of several insulated conductor segments connected to the rotor conductors. If the armature has multiple coils, the commutator will similarly have multiple segments—one for each end of each coil. The function of the commutation ring, in combination with brushes, is to switch the polarity of the rotor coils, keeping the armature in rotation.

In regards to operation, BDC motors have two functioning modes: motor and generator. Motors transform electrical energy into mechanical energy, whereas, a generator does the inverse. The structure of a BDC motor and the laws/principles of operation, are the same for both modes, only differing in the direction of energy. In the context of an EV, the BDC motor needs to operate properly in both operation zones. It is assumed that while the BDC motor produces a positive torque (acceleration/motoring) it works as a motor and during regeneration braking it operates as a generator.

BDC motors operation is based on the Lorentz Law, which states that a current-carrying conductor placed in a magnetic produces a force [47]. When applied a DC supply to the stator windings, it is created a magnetic field that crosses the armature and the respective conductors. At the same time the brushes introduce current on the armature conductors, the interaction the electric current and magnetic field produced by the stator generates a driving torque. When the armature of a BDC motor rotates under the influence of driving torque, the armature conductors move through the magnetic field and an Electromotive Force (EMF) is induced, similar to a generator. This phenomenon is described by Faraday's Laws of Electromagnetic Induction, which states that any change in the magnetic environment of a coil of wire will cause a voltage ($V_{emf}$) to be induced in the coil [48]. The generated voltage has opposite polarity relative to the motor supply and is called back-EMF. The back-EMF value is proportional to the rotor rotation speed ($N$), number of poles ($P$) and conductors in the armature ($Z$), and the magnetic flux $\phi$. The back-EMF voltage can be translated as follows, where $A$ represents the number of parallel paths through the armature.

$$V_{emf} = \frac{N\,P\,Z\,\phi}{60\,A} \tag{3.1}$$

The efforts from the supply voltage to overcome the back-EMF are converted into rotor torque. Therefore, this energy conversion in a BDC motor is only possible due to the production of back-EMF. On top of that, the presence of back-EMF makes the BDC motor a self-regulating motor, where it makes the motor draw as much armature current as is just sufficient to develop the torque required by the load [49].

Regarding the Lorentz law, conductors under North magnetic pole (N) carry currents in one direction while all the conductors under South magnetic pole (S) carry current in the opposite direction. Since each armature conductor is carrying current and is placed in the magnetic field, a mechanical torque is created.

The direction of mechanical force generated by the conductors under the N pole is positive (considering the traditional y-axis), while an opposite direction force is created under the S pole, allowing the armature to rotate. To maintain this interaction it is used brushes that invert the polarity of the armature conductors. Each brush is connected to the positive and negative pole of a DC supply, respectively, and by making contact with the segments of the commutation ring linked to the armature conductors their polarity is reversed. At the same time, these conductors become under the influence of the next pole of opposite polarity and consequently, the direction of the force on the conductor remains the same. By reversing the current in each conductor as it passes from one pole to another, it helps to develop a continuous and unidirectional torque.

The process of described above is illustrated in Figure 3.1, where is shown a simplified version of a BDC motor and it's creation of torque.

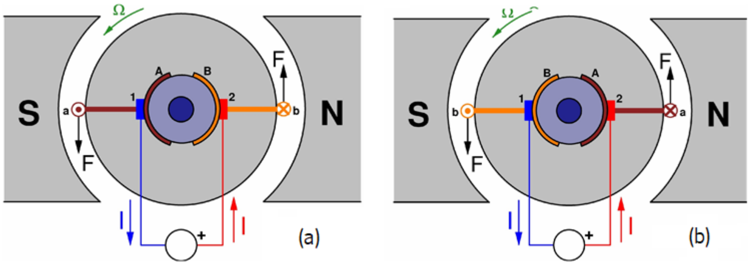

Figure 3.1: Operation and of a BDC motor based on the Lorentz law and the respective creation of torque. $F$ represents the force created, 1 and 2 are the brushes, and A and B are the respective commutation segments that are connected to a DC supply: (a) and (b) show the rotor on two positions shifted 180° from each other. $\Omega$ represents the rotation direction, and $\odot$ and $\otimes$ the vector direction, into the page and out of the page, respectively. The S and N are the stator poles. (Adapted from [50]).

### 3.2.1 Operation as Generator

The principle of operation of a generator is similar to what was described above for a general BDC motor. It is applied a DC voltage to the stator windings, that according to the Lorentz law creates a magnetic field that crosses the rotor. To the motor rotor is applied a mechanical torque produced by a load attached to the shaft, making the rotor rotate. In the context of an EV, this is equivalent to the wheel bearings exerting torque during braking. When the armature rotates, the respective conductors perpendicularly cross the magnetic field lines produced by the stator, generating voltage. The voltage produced on the armature conductors is given by equation 3.2, where $e$ is the voltage produced, $v$ the armature rotation speed ($v = \omega \cdot r$ being angular velocity ($rad/s$) and r the rotor radius), $B$ is the magnetic flux density produced by the stator windings and $l$ is the length of the rotor conductors.

$$e = v\,B\,l \tag{3.2}$$

Considering equation 3.2, it is concluded that the voltage induced on the conductors is proportional to the rotor rotation speed and the intensity of the magnetic flux produced by the stator windings, which in turn depends on the value of current applied on these windings. Observing figure 3.1 it can also be inferred that the rotor conductors when crossing the magnetic flux lines near a stator pole, will have the opposite polarity of the induced voltage when crossing the flux lines near the other pole. In other words, the induced voltage in the rotor conductors is AC [4]. To obtain a DC voltage on the output is used the commutation ring. As the commutation ring rotates, the brushes are fixed and pressed against it, making contact with the segments of the commutation ring that are connected to the armature conductors of respective polarity. In other words, the commutation ring and the brushes play the role of a mechanical rectifier, converting the AC voltage in the rotor conductors, into DC voltage [4]. Considering this, the voltage output of the rotor has a small "ripple", since the maximum values of voltage in each conductor of the rotor occur in different moments, the sum of these voltage values give a final value with a small ripple. The value of the ripple will be smaller the greater the number of grooves, conductors, and segments in the rotor commutation ring. With this, the generated output voltage in the armature is the sum of the rotor conductors induced voltages and is given by equation 3.3, where $k$ is the motor constant ($V/rpm$), $\phi_f$ is the flux produced by the stator windings and $\omega_r$ the angular velocity.

$$V_{emf} = k_v \, \phi_f \, \omega_r \tag{3.3}$$

### 3.2.2 DC motor Equivalent Model

To simulate and design the motor control is necessary to transcribe the theory principles to a circuit model, allowing an easier understanding of its behavior and estimation of parameters. The equivalent electrical circuit of a BDC motor is illustrated in Figure 3.2 It can be represented by a voltage source $V_s$ across the coil of the armature. The electrical equivalent of the armature coil can be described by an inductance $L_a$ in series with a resistance $R_a$ in series with back-EMF $V_{emf}$ which opposes the voltage source. $L_a$ and $R_a$ are constant and are usually specified on the motor datasheet. The supply voltage is dependent on the application but it is kept constant throughout the motor operation. $V_{emf}$ and $I_a$ are related to speed and torque respectively, therefore assume different values during operation.

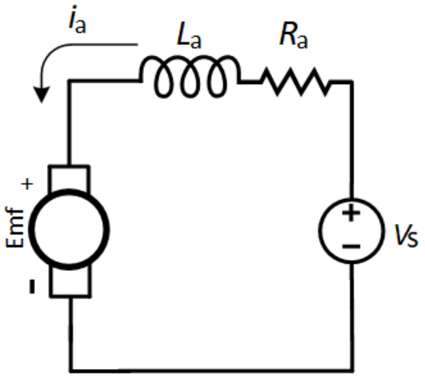

Figure 3.2: Equivalent model of a BDC motor.

Considering that back-EMF is contrary to the supply voltage, it has a subtracting effect and the net voltage on the armature, is written as follows, where $V_m$ is the applied to the motor and $R_a$, $I_a$ correspond to armature resistance and current, respectively:

$$V_m = V_s - V_{emf} = R_a\, I_a + L_a \frac{di_a}{dt} \tag{3.4}$$

Given the parameters of a specific motor back-EMF can also be written as:

$$V_{emf} = k_v\, \omega \tag{3.5}$$

When the motor is operating without load, only a small torque is required to overcome the friction and windage losses. Therefore, since the torque is proportional to the armature current, $I_a$ is low and the $V_{emf}$ is nearly equal to the applied voltage. If the motor is suddenly loaded, it causes the rotor to slow down. Thus, the armature rotation speed is reduced, and consequently, the back-EMF decreases. With the decrease of back-EMF is allowed a greater current to flow through the armature conductors meaning an increased driving torque. The motor will start accelerating when the armature current is just enough to produce the torque required by the load. As the armature speed increases, $V_{emf}$ also increases and $Ia$ to decreases. The motor will stop accelerating when the armature current is too low to produce the torque required by the load.

## 3.3 BDC Motor Converters

In this section are presented generic converter solutions for BDC motor drive. As alluded before these converters make an interface between the batteries the motor. The converters presented are widely used in regulated switch-mode DC power supplies and BDC motor drive applications. To drive a BDC motor load is needed a converter and a respective control theory, allowing to command the motor behavior.

### 3.3.1 Full-Bridge Converter

A Full-bridge or H-Bridge is a Voltage Source Inverter (VSI) used on DC drives, DC-AC applications (rectifier), and switched-mode power supplies [51]. It allows bidirectional current flow, supplies a controllable voltage to a load, and it is constituted by four semiconductors in an H-shape (Figure 3.3). In the context of a BDC motor, the H-bridge presents a four-quadrant DC drive system controlled by PWM signals [10], [43], [52]. The operation of an H-bridge is based on which semiconductors are active, determining a specific operation mode [52]. Considering this, it is possible to reverse the voltage applied to the load and control the current direction, consequently inverting the motor's rotation. Translating to the context of an EV, the H-bridge controls the modes of operation, representing acceleration and braking in both directions (forward and reverse), making up to a total of four functioning modes [10], [52]. For high-power applications where is required controllable semiconductors driven by PWM, the most common semiconductors are IGBTs. With this in mind, it is opted to integrate IGBTs for the converters developed. Figure 3.3, shows the topology of a H-bridge applied to the motor equivalent model, where $V_b$ is the battery voltage supply. S1 to S4 are the converter semiconductors, which in this illustration are IGBTs.

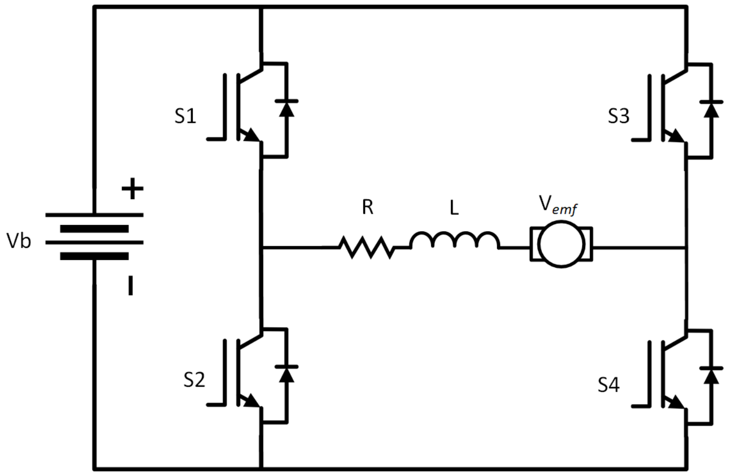

Figure 3.3: H-bridge electric schematic applied to the equivalent model of a BDC motor

Each mode has a combination of working IGBTs, where the driven semiconductor determines a specific mode. Observing Figure 3.3 is concluded that each combination of two operating IGBTs define a specific mode. However, both semiconductors of the same leg (S1 and S2 or S3 and S4) can not be active at the same time, otherwise causing a short circuit. On the other hand, if the two top or two bottom semiconductors are active the motor coasts and it is idle. Therefore, the remaining four combinations are the most relevant, which define the motor operation. On table 3.1 are presented the conditions of each IGBT regarding the four areas of operation. To stipulate concepts such as ”motor’s direction of rotation” is arbitrarily considered that the motor is rotating ”forward” in one direction or ”reverse” if the rotation is inverted. Considering this, it is defined that modes of operation 1 and 2 concern one direction of rotation and the remaining 3 and 4 the opposite. In regards to the torque exerted by the motor, motoring is referred as acceleration, or positive torque, considering that the voltage applied to the motor is positive where the energy flux direction is from battery to motor. Regenerative braking occurs when is applied a torque contrary to the current rotation and the current flows from the motor to the batteries.

Table 3.1: Motor modes of operation and the corresponding combinations of IGBT states.

| | S1 | S2 | S3 | S4 |
|---|---|---|---|---|
| Forward Motoring | PWM | OFF | OFF | ON |
| Forward Regeneration | OFF | PWM | OFF | OFF |
| Reverse Motoring | OFF | ON | PWM | OFF |
| Reverse Regeneration | OFF | OFF | OFF | PWM |

Figure 3.4 illustrates the four areas of operation of the H-bridge, displaying the current flow and voltage applied to the motor represented by it’s simplified model. For each mode, the motor voltage is given by

the following equations, $\alpha_{1,2,3,4}$ correspond to the PWM duty-cycle applied to the respective semiconductor (1-Forward Motoring, 2-Forward Regeneration, 3-Reverse Motoring, 4-Reverse Regeneration):

Forward Motoring:

$$V_m = V_b\,\alpha_1 \tag{3.6}$$

Forward Regeneration:

$$V_m = V_b\,(1-\alpha_2) \tag{3.7}$$

Reverse Motoring:

$$V_m = -V_b\,\alpha_3 \tag{3.8}$$

Reverse Regeneration:

$$V_m = -V_b\,(1-\alpha_4) \tag{3.9}$$

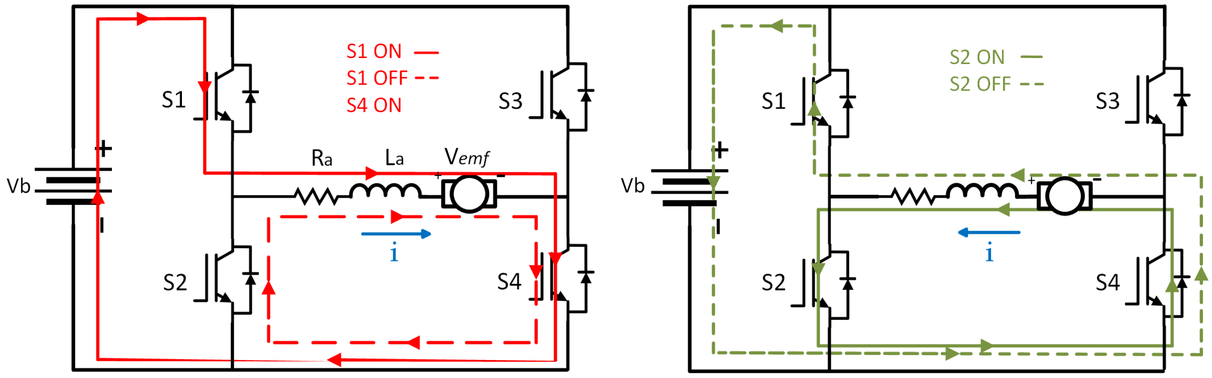

a) Forward Motoring

b) Foward Regeneration

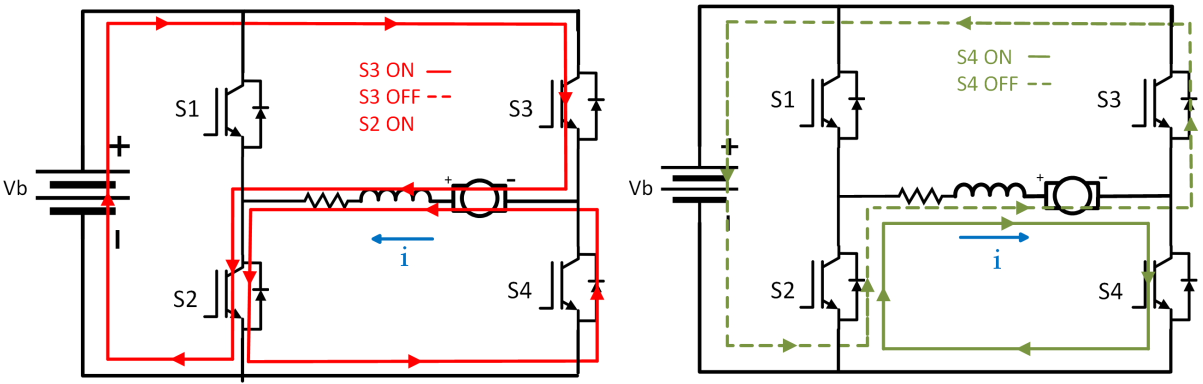

c) Reverse Motoring

d) Reverse Regeneration

Figure 3.4: H-Bridge topology, its behavior in each operation zone and the respective current flow.

### 3.3.2 Half-Bridge Converter

A Half-bridge converter is a DC-DC buck-boost topology used on applications where is required an output voltage higher or lower than the input. Buck-boost converters can be used as an interface on battery supplies, in fuel cell systems, as a complement in power factor correction, and other DC-DC applications where is necessary wide operation ranges of input and output voltage [53, 54, 55]. Buck-boost converters can be unidirectional or bidirectional depending on semiconductors used, diodes, or IGBTs, respectively. The main advantage of this topology is the requirement of only two semiconductors, and admitting that they are controlled by PWM signals the control theory is also simple [54]. The buck-boost operation is defined by which semiconductor is active. While the motor voltage is higher than battery voltage, the converter operates as a buck and S1 is active, as a boost S2 is active and occurs discharge (Figure 3.5). Considering this the semiconductors switching and the respective mode depends on the setup of the converter and voltage levels on each side. In light of an EV, the bidirectional version of this converter can operate in both motoring and regeneration modes despite it's simple structure. Some disadvantages of this topology are difficulties on providing a smooth transition from buck to boost operation and power stress than the IGBTs are exposed to since only one semiconductor operates at time [55]. On top of that this topology does not support operation on reverse gear modes as opposed to the full-bridge solution.

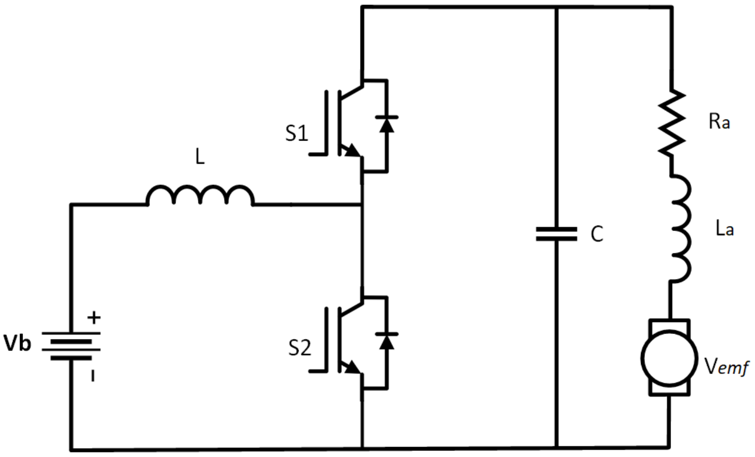

Figure 3.5: Half-bridge topology schematic.

## 3.4 Motor Control Techniques

A bidirectional power converter is necessary to deliver energy from batteries to the electric motor and vice versa. To achieve the aforementioned, the control of the power converter is an important part of managing the electrical energy stored in the batteries. Therefore, the design should fulfill the control objectives for multi-operation regions. The motor controllers presented are current and voltage based controls where the user has a hand accelerator. In the particular application of a current/torque control, the user inputs a reference current resulting in an indirect speed control. Another solution can be voltage/speed controllers, usually called cruise-controls where the controller output provides a constant speed for the motor.

### 3.4.1 PI Torque Control Based on the Converter Model

The devised controller allows an accurate torque control proportional to the current applied on the motor. This control is identical to that of the vehicle with a hand accelerator, where it is given an acceleration reference by means of demanding more or less current [2], [11], [56]. As mentioned before, the motor torque is proportional to the current, therefore the torque control is made using current instead. The control allows an automatic switch between motoring and regeneration modes and for each mode of operation, the control calculates a duty-cycle value to them be processed by PWM technique and subsequently applied to semiconductors. The control of the BDC motor is based upon the identification of the respective areas of operation. For that, is required to measure the back-EMF and the motor's current. Considering this, the four areas of operation can be identified by the quadrants of a two-axis plane composed by $V_{emf}$ and $i_{ref}$, as shown in Figure 3.6.

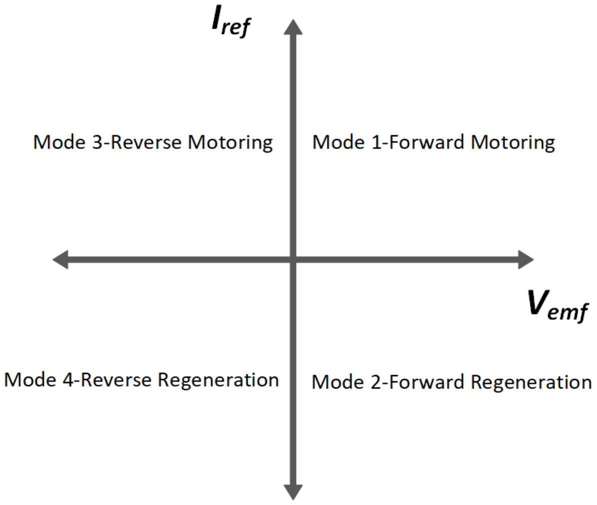

Figure 3.6: Categorization of the areas of operation on a $I_{ref}$ and $V_{emf}$ two-axis plane.

After defining the conditions for each mode, it is possible to determine the current dynamics utilizing the motor's equivalent model. Accordingly, by rearranging equation 3.4 is obtained the equivalent for the different operation modes:

Mode 1:

$$L\frac{di}{dt} + Ri + km\,\omega = \alpha_1\,V_b\,, \quad i \geqslant 0 \tag{3.10}$$

Mode 2:

$$L\frac{di}{dt} + Ri + km\,\omega = (1-\alpha_2)\,V_b\,, \quad i < 0 \tag{3.11}$$

Mode 3:

$$L\frac{di}{dt} + Ri + km\,\omega = -\,\alpha_3\,V_b\,, \quad i < 0 \tag{3.12}$$

Mode 4:

$$L\frac{di}{dt} + Ri + km\,\omega = -\,(1-\alpha_4)\,V_b\,, \quad i \geqslant 0 \tag{3.13}$$

The motor controller determines which mode the motor should be switched to as well as the duty-cycle ratio needed to achieve accurate current tracking. Therefore to determine the PWM duty-cycle ($\alpha_x$) is used a PI current control, similar to what was described in section 2.6.1. The current control module generates a control output $u$ based on the error between the commanded reference current $i_{ref}$ and the measured motor current $i_m$ [56]. Based on equations 3.10 to 3.13 and the control signal $u$ the duty-cycle for each mode can be determined by the following equations:

Mode 1:

If $i_m \geqslant 0$ and $V_{emf} \geqslant 0$, then $\alpha_1 = \frac{1}{Vb}\left(u + V_{emf}\right)$

Mode 2:

If $i_m < 0$ and $V_{emf} \geqslant 0$, then $\alpha_2 = 1 - \frac{1}{Vb}\left(u + V_{emf}\right)$

Mode 3:

If $i_m < 0$ and $V_{emf} < 0$, then $\alpha_3 = -\frac{1}{Vb}\left(u + V_{emf}\right)$

Mode 4:

If $i_m \geqslant 0$ and $V_{emf} < 0$, then $\alpha_4 = 1 + \frac{1}{Vb}\left(u + V_{emf}\right)$

In order to describe the different components of this control technique is illustrated on Figure 3.7 the respective block diagram.

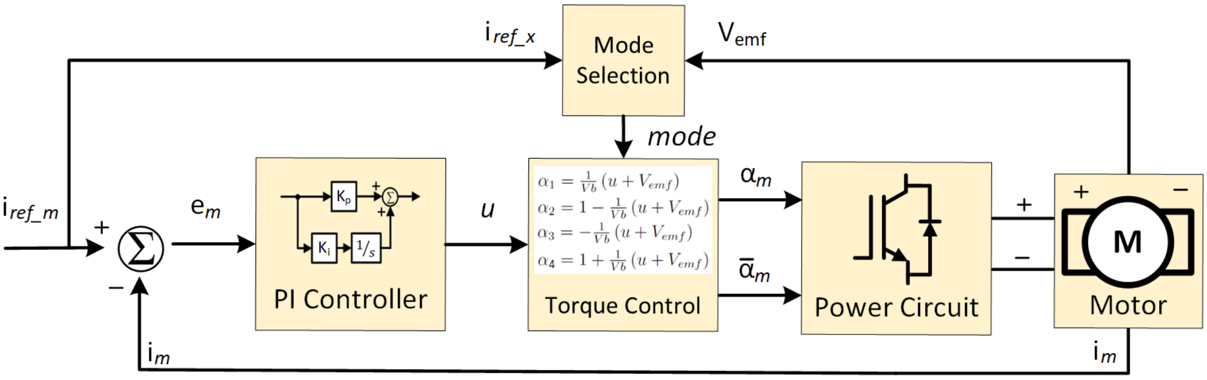

Figure 3.7: Block diagram of the torque control technique.

### 3.4.2 Hysteresis Band control

The hysteresis band control technique consists of ensuring that the motor voltage follows a certain reference voltage, where it's instantaneous value is limited between two previously defined values, i.e. within a certain hysteresis range [31], [57]. The implementation of the hysteresis voltage control technique is achieved by calculating the error, e.g. between the voltage measured on the motor $V_m$ and the reference voltage $V_{ref\_m}$, and then comparing it with the hysteresis limits defined, ±H, which results in a command signal [31], [57]. The block diagram respective to the hysteresis control described above is displayed in

Figure 3.9.

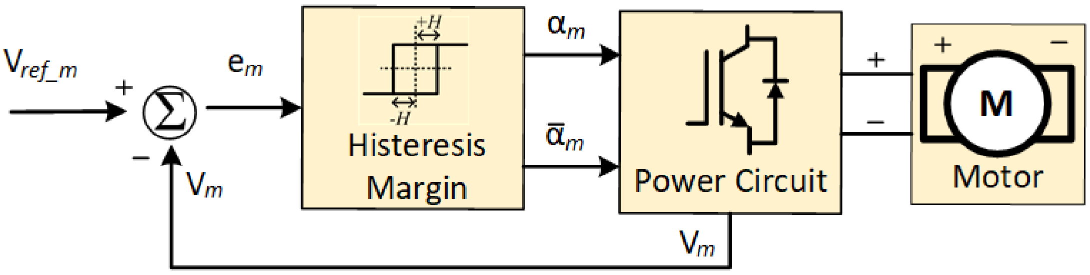

Figure 3.8: Block diagram of the hysteresis control technique.

The operating principle of the hysteresis control technique can be seen in Figure 3.9, where the measured motor voltage waveforms, reference voltage, as well as the respective minimum -H and maximum +H limits. In this voltage control technique, while the instantaneous motor voltage value is lesser than the instantaneous voltage value plus the hysteresis band, the semiconductor will remain closed. In case the instantaneous voltage value is greater than the instantaneous voltage value minus the hysteresis band, the IGBT will remain open. In case the error value is within the established hysteresis limits, the IGBTs must maintain its current state. Therefore this control technique does not require PWM technique.

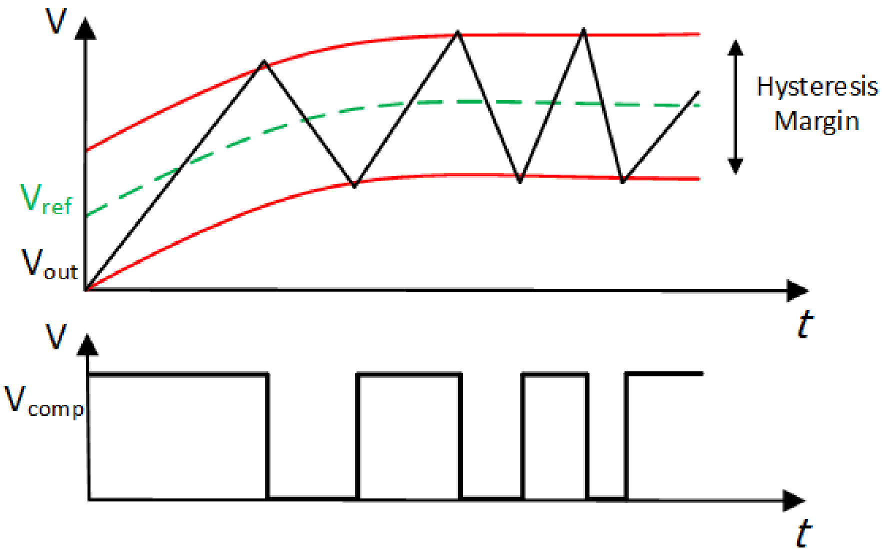

Figure 3.9: Reference, output and compare signals resulting from hysteresis voltage control.

In the context of a motor controller, this theory also requires motor mode recognition and is achieved by measuring the motor voltage and. Accordingly, during motoring mode the supply voltage is positive while during regeneration the voltage has negative polarity, therefore and the hysteresis band should be positive or negative, respectively. The disadvantages of the hysteresis based control techniques are, variable switching frequency, voltage and speed distortion caused by sector changes, starting and low-speed operation problems, as well as high sampling frequency needed for digital implementation of hysteresis controllers [57].

## 3.5 Chapter Conclusion

This chapter described the BDC motor theory and constitution. In the first section, it was presented the core components of a BDC motor, called rotor/armature and stator. Then is described the creation of torque, and how the back-EMF voltage is generated. With this, it was detailed the equivalent model of a BDC motor and it was deducted the respective fundamental equation.

In section 3.3 are presented two converter topologies to operate a BDC motor, a full-bridge or H-Bridge and a half-bridge converter. Then in each subsection described the operation and different modes. The mode of operation depends on which controllable semiconductors are active. The full-bridge topology has four controllable semiconductors and four modes of operation. In the context of driving a BDC motor these four modes correspond to Forward Motoring, Forward Regeneration (Braking), Reverse Motoring and Reverse Regeneration. The half-bridge only requires two semiconductors but it is limited to the two forward gear modes. On top of that, the half-bridge mode transition is not smooth and the semiconductors are under more stress when compared to the H-bridge.

The final section details two torque control techniques, first a PI and model based control, and a hysteresis control technique. For the PI torque control is necessary to detect the mode of operation based on the input reference current and the measured back-EMF voltage. Then it is used a PI control which output is a command variable that is used to determine the duty-cycle of the PWM signal to be applied to the respective semiconductor. In the hysteresis band control is defined a maximum and minimum limit value called hysteresis range in which the controlled voltage is set. With this, it is calculated the error between the measured voltage and a reference and then compared with the hysteresis bands. If the error variable exceeds the maximum or minimum limits, the semiconductor is OFF or ON, respectively. However this control technique various disadvantages such as variable switching frequency and no regulation of the PWM duty-cycle, since this signal is either ON or OFF. On top of that, in the context of this, thesis is more intuitive to use a current control and regulate the motor acceleration, since is more similar to a regular vehicle.

# Chapter 4

# Simulations of the Motor and Charger Systems

## 4.1 Introduction

A simulation tool allows testing the performance of control systems, as well as manipulate their parameters to obtain the desired behavior. Therefore, it is convenient that the simulation model used is very close to the actual model, and to take into account non-ideal aspects of the system components. Besides, problems resulting from design errors can be identified and corrected, thus avoiding damage to electronic components and improving for workers.

All presented simulations were performed using PowerSim Inc's PSIM v9.0.3 simulation software, which is especially suitable for power electronics applications.

This chapter is focused on the simulation of the charger and motor modules. In the charger module is simulated the Passive PFC solution and for the motor module, the full-bridge solution.

Primarily, it is described the BDC motor parameters and the respective simulation model. Then, it is implemented the H-bridge topology and the respective torque control based on its model. With this, it is tested the control theory with a constant supply voltage or a battery, it is simulated the motor operation with a mechanical load and the results are presented. Afterward, it is addressed the PFC solution, its synchronization with the power grid, the current control implemented, and the DC-link regulation. Finally the simulation results for the charger module are presented.

## 4.2 Motor Module Simulation

In this section, firstly is described the motor model and the respective quantitative characteristics. Then, it is described the implementation of the control system where it is explained how is developed the control technique and other details, such as PWM technique. Lastly, the topology with a fixed DC supply and a battery is tested.

### 4.2.1 Motor Simulation Model

This simulation model was based on the ME1003 motor, a permanent magnet brush-type motor with 15 kW ($\approx$20 CV) power, 90% efficiency, brush life of 1500 hours at rated current and a speed range between 0 and 5000 rpm [58].

The motor's electrical and mechanical characteristics are presented on Table 4.1, which are implemented on the DC motor model of the software.

Table 4.1: Technical data of the DC motor simulated.

| **Characteristics** | **Values** | **Units** |
|---|---|---|
| Max Current | 500 | A |
| Voltage Constant | 0.0207 | V/rpm |
| Torque Constant | 0.197 | Nm/A |
| Rated Torque | 39 | Nm |
| Max Speed | 5000 | rpm |
| Electric Power | 15 | kW |
| Moment of Inertia | 268 | kcm$^3$ |

The PSIM software has the model of a DC motor where can be input the known physical parameters of the motor. The necessary parameters to simulate a DC motor on PSIM, are the armature resistance and inductance ($R_a$ and $L_a$) and field ($R_f$ and $L_f$), rated DC supply ($V_t$), rated armature and field current ($I_a$ and $I_f$) and rated speed ($n$). The parameters used in the simulation model are present in Table 4.2. Some parameters were not obtainable on the motor datasheet so it was deducted and consulted based on the known variables and other similar power motors.

Table 4.2: Motor parameters utilized for simulation model

| **Characteristics** | **Values** | **Units** |
|---|---|---|
| Armature Resistance | 0.012 | $\Omega$ |
| Armature Inductance | 0.93 | mH |
| Field Resistance | 1 | $\Omega$ |
| Field Inductance | 9.88 | mH |
| Moment of Inertia | 268 | kcm$^3$ |
| Rated Voltage | 72 | V |
| Rated Current | 200 | A |
| Rated Speed | 3000 | RPM |
| Field Current | 20 | A |

Once the internal parameters of the motor are obtained, it is simulated the model displayed on Figure 4.1. In the illustrated situation, it is measured the torque and speed to determine the mechanical power. It was also placed a mechanical load to simulate a more practical motor operation.

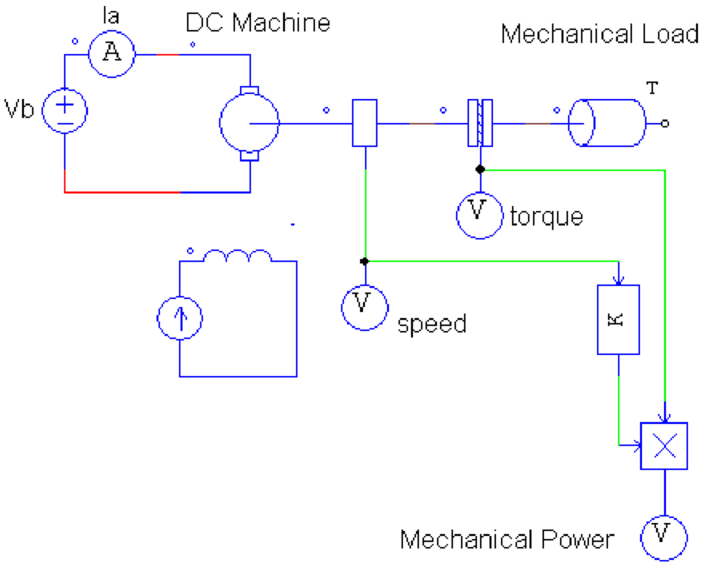

Figure 4.1: Simulation model of a DC motor.

### 4.2.2 Motor Control System

After establishing the motor simulation model is described the implementation of the motor control systems. With this, Figure 4.2 shows the motor control system design. In Figure 4.2 is visible a coding block, in which are found the algorithms and control techniques, coded in C language. The use of this block is advantageous in terms of practical work to be developed since the range of DSPs (Digital Signal Processor) used later on are also programmed in C language. This facilitates the migration of software from simulation to practical implementation. The coding block has as inputs variables measured by sensors that are required for the control operation, e.g. the motor current, and the speed. Based on the sampling of these quantities, the necessary references to the current control are generated. Logical outputs are also available to allow the motorization of some crucial system variables to evaluate a proper operation. In addition to the control blocks presented, the implementation of the PWM technique is also visible, which was used to generate control signals for the IGBT used in the power converters. Due to the high power levels involved on the motor system, the switching frequency chosen for the semiconductors is 10 kHz. According to the Nyquist-Shannon theorem, to reconstruct the original signal is required a sampling frequency at least two times higher than the switching frequency [59]. With this, the sampling frequency of the input variables is 20 kHz. With a lower value, the control would have information losses that would impede its correct operation.

The control algorithm is the torque control described in section 3.4.1, based on detecting the motor operation mode and activating the respective semiconductor. The PWM applied at the semiconductor gate has a duty-cycle calculated by a PI control between reference current and the measured motor current. The output of the control and the coding block is a duty-cycle with a specific value that is then processed by the PWM technique.

In the simulation, the PWM technique is made “analogically” through a comparative circuit. Accordingly, the duty-cycle is compared with a triangular wave with a frequency equal to the switching (10 kHz) and minimum and maximum values equal to the arbitrary duty-cycle range specified in the control block. This results in a PWM signal with a duty-cycle based on the control output. Figure 4.2 shows the implementation of the overall motor system, including the PWM technique, which has four comparators that compare the duty-cycle value signals coming from the current control loops with a 10 kHz triangular signal. This value defines the switching frequency of fully controllable semiconductors. The triangular wave amplitude is the same as the duty-cycle range.

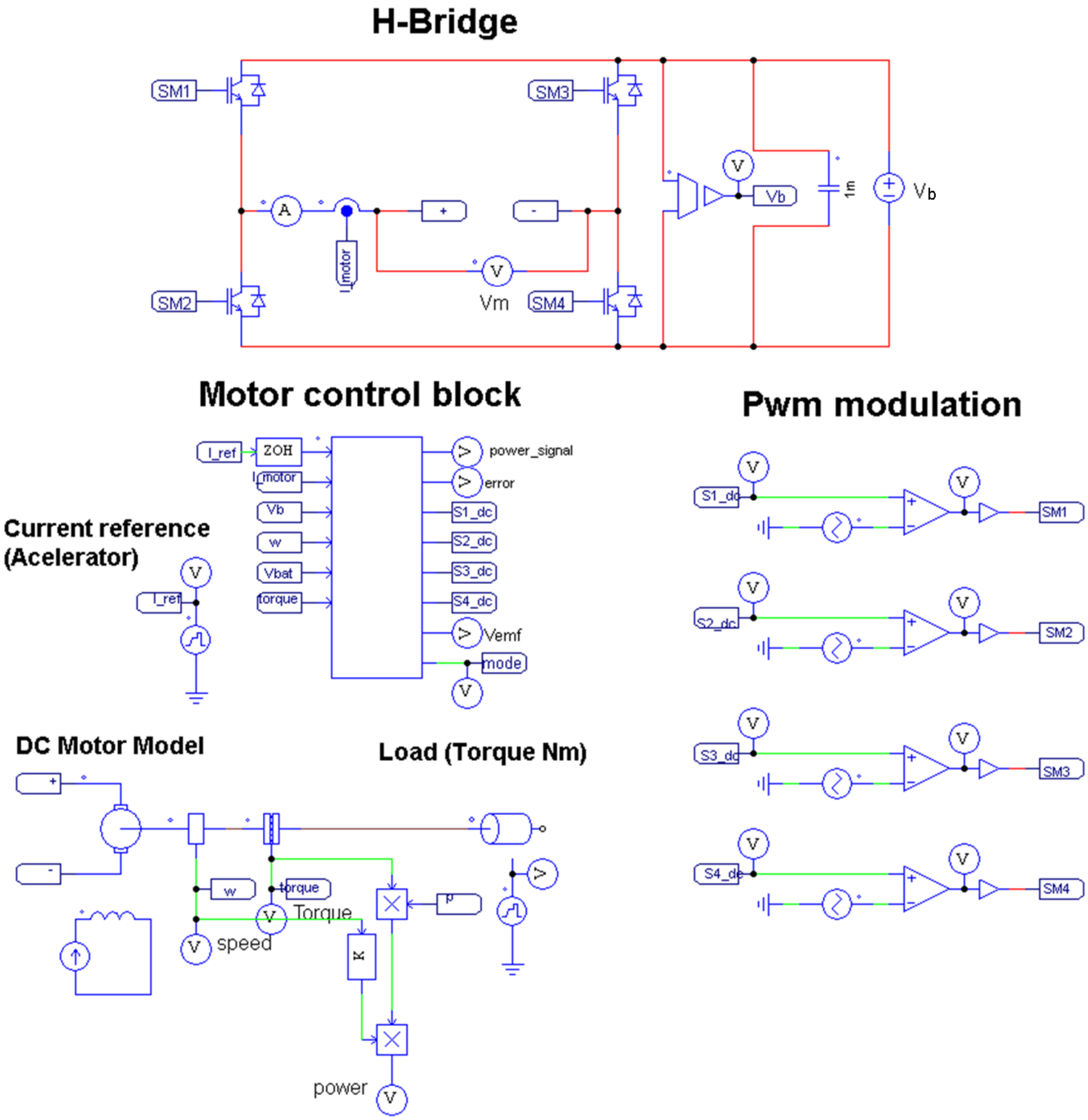

Figure 4.2: Motor converter and control system simulation design.

In figure 4.3 is shown the PWM technique, with the triangular and the duty-cycle reference signals, as well as the resulting PWM signal.

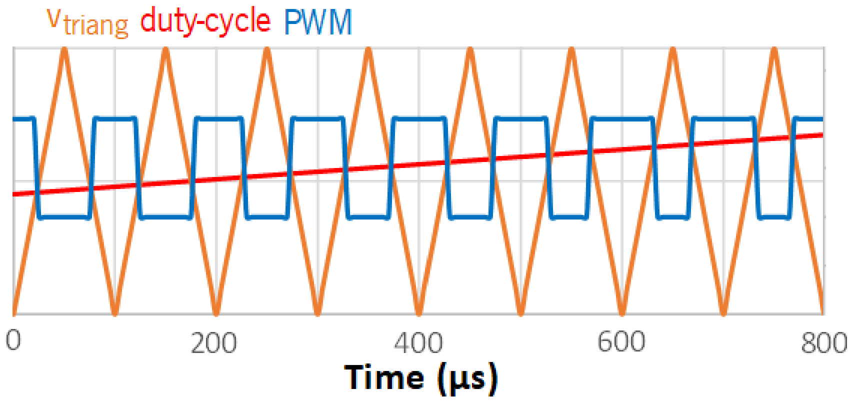

Figure 4.3: PWM technique where it is shown the resulting PWM duty-cycle according to the control output value and the triangular wave.

With all the parts that constitute the traction system, the implemented simulations to validate the topology are conducted. To test the system response to variations on the reference current it is monitored the behavior of motor current. Thus, Figure 4.4 shows the results of the simulation of reference steps and the respective motor current evolution. For the conducted simulation, it is chosen an example of reference variations with steep variations (high $di/dt$) to represent the "worst" case scenario for the control. As observable the response to the variations is fast taking into account the $di/dt$. This aspect is very important in the context of an EV where response times are crucial for safety.

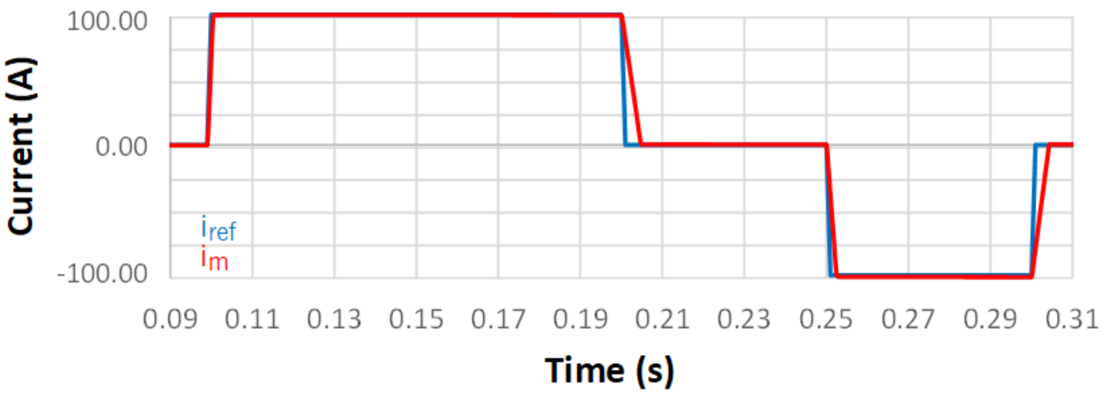

Figure 4.4: Response time simulation waveform of the reference current ($i_{ref}$) and the motor current ($i_m$).

### 4.2.3 Simulation of Forward modes with 10 Nm Load and a constant DC Power Supply

The next step is simulating the motor operation and evaluate its electric and mechanic behavior. Therefore it is tested the traction system and measured variables such as speed, motor current, and mode of operation. On top of that it is simulated a mechanical load of 10 Nm attached to the motor. This implicates that while $i_m$ is low the motor can not produce enough torque to start rotating. According to Table 4.1, the torque constant is 0.197 Nm/A, therefore to generate enough torque to compensate a 10 Nm load it is required at least 50 A. For this specific simulation, it is arbitrated that, on the first stage $i_{ref}$ is a rising slope (0.75 s to 1.0 s), followed by a braking period (0.75 s to 1.0 s), as represented by Figure 4.5.

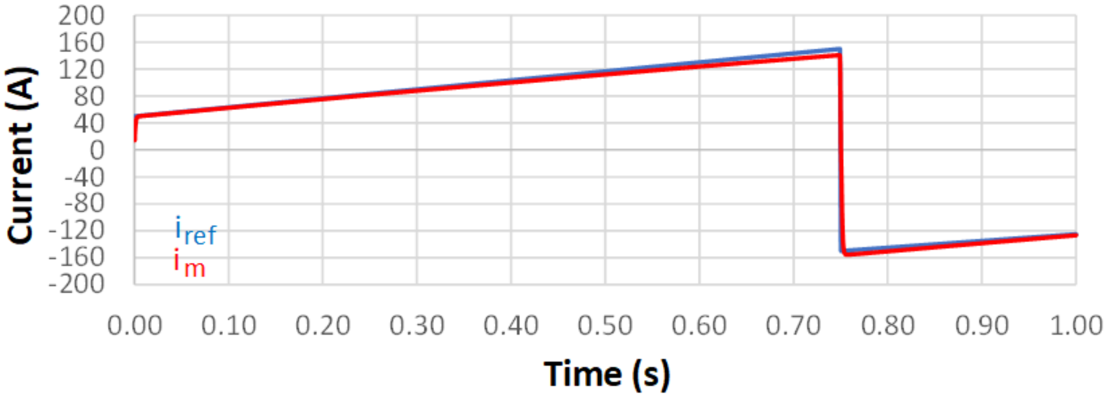

Figure 4.5: Simulation waveforms of a $i_{ref}$ slope for and the respective $i_{motor}$.

To validate the control system it is measured the evolution of rotation speed and consequently the back-EMF voltage ($V_{emf}$), according to $i_{ref}$. The simulation results present in Figure 4.6 shows that with the increase of the motor current, the acceleration also increases, due to a higher torque generated. Similarly, during braking, the decrease of motor current (absolute value) reduces the motor deceleration. Since $V_{emf}$ is proportional to speed the respective waveforms are equal. Is important to notice that despite being used a constant DC power supply it is possible to test the regenerative braking since in a simulation environment the source can absorb energy, contrary to what happens in practical tests.

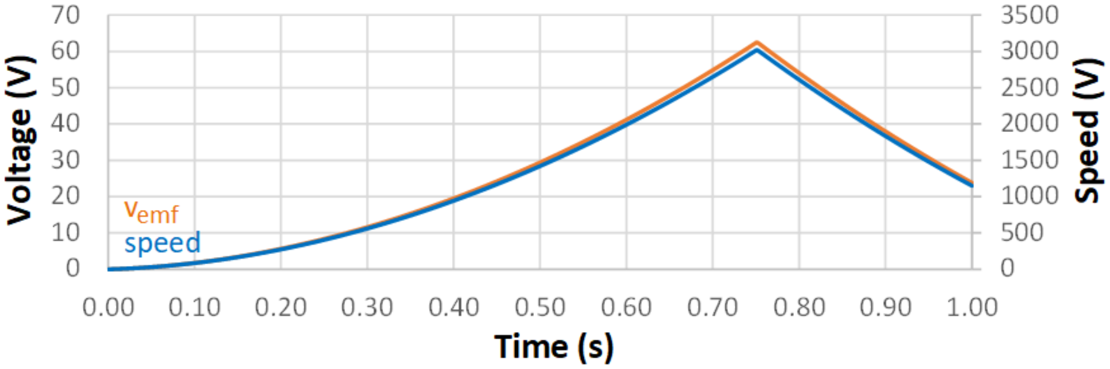

Figure 4.6: Simulation waveforms of the evolution of speed and $V_{emf}$, according to the slope reference current.

To validate the motor operation is monitored it's mode and transitions. With this, in Figure 4.7, it is possible to observe that with the input of a positive $i_{ref}$ the motor operates in mode 1, or forward motoring, and when the control is fed a negative value the motor operates in mode 2 and brakes.

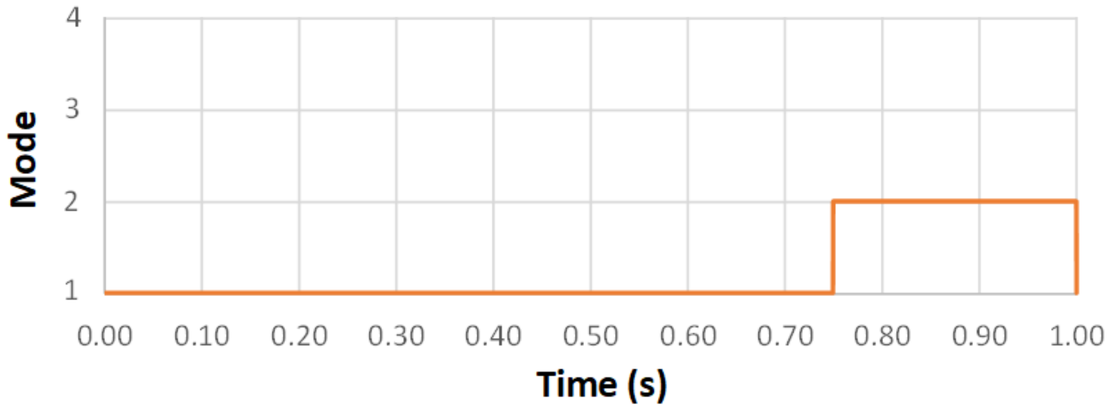

Figure 4.7: Simulation waveforms of the operation modes and transitions throughout the simulation of the traction system with a slope reference current and a 10 Nm load.

### 4.2.4 Simulation with 20 Nm Load and 72 V Fixed DC Power Supply

This section details the behavior of the motor with a mechanical load of 20 Nm, which corresponds to approx. 50% of the rated torque value of the motor used. On top of that is used a fixed DC power supply of 72 V. Figure 4.8 shows the evolution of the motor current $i_m$, from the reference currents assigned in the Table 4.3. For certain time intervals are shown, the respective torque applied and the resulting evolution of speed. In more detail, this simulation tries to establish an extreme example where current variation is steep. As alluded before, braking is seen as a force that acts in an opposite direction, in other words, it is not used a brake but instead of it is applied counter-current that produces an inverse torque.

In this particular simulation, it is used a 20 Nm load, thus, according to the torque constant provided in Table 4.1, the reference current must be greater than 101 A. Besides, both the motor and load moment of inertia was downsized to decrease the system's time constant, making it possible to fit the simulation of different modes on a reduced time interval and improving graphic rendering.

| **Reference Current (A)** | **Time frame** |
|---|---|
| 130 | 0 s to 0.5 s |
| -140 | 0.5 s to 1 s |
| 115 | 1.0 s to 1.5 s |
| -105 | 1.5 s to 2 s |

Table 4.3: Reference currents applied to the braking controller during different instants of the motor operation for a 20 Nm load

According to the current steps applied, the controller can generate adequate responses so that the motor current can follow the respective reference. As observed in Table 4.3, the conducted simulation uses constant acceleration intervals and the controller behavior is evaluated based on the relation between $V_{emf}$ and speed, $i_m$, torque and the mode transition. That being said, in Figure 4.8 (a) and 4.8 (b) the evolution of mechanical and electrical characteristics are presented, respectively. Observing Figure 4.8 (a), from 0 s and 1 s it is possible to confirm that the acceleration/deceleration is proportional to the absolute current value. For the first 0.5 s the motor accelerates with a current of 130 A reaching 1500 rpm, then it is applied the braking, switching to regeneration mode, until speed direction is inverted, causing the motor to accelerate in the opposite direction.

From 0.88 s to 1 s and 1 s to 1.12 s the speed evolution is greater because in those particular instances the load is applying force in the same direction as the motor, helping decelerate/accelerate as observed in Figure 4.8 (b). Transitioning to a practical situation, it is similar to braking on a uphill or accelerating in a downhill, where in these cases the mechanical load applies torque in the same direction as the motor, increasing acceleration. With this, it is possible to validate the traction system by comparing the intervals of each mode with the evolution of torque and speed, respectively.

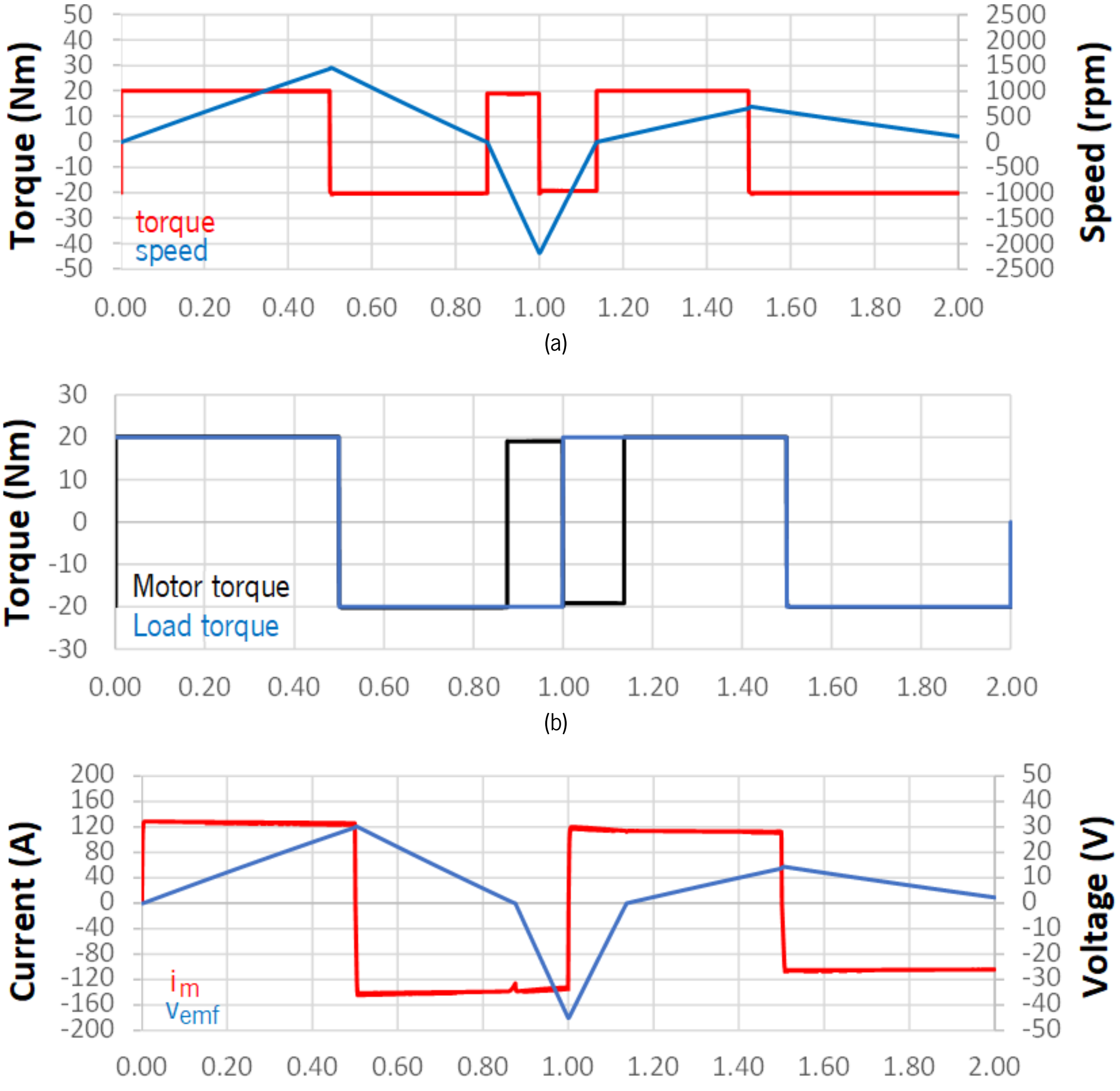

(a)

(b)

(c)

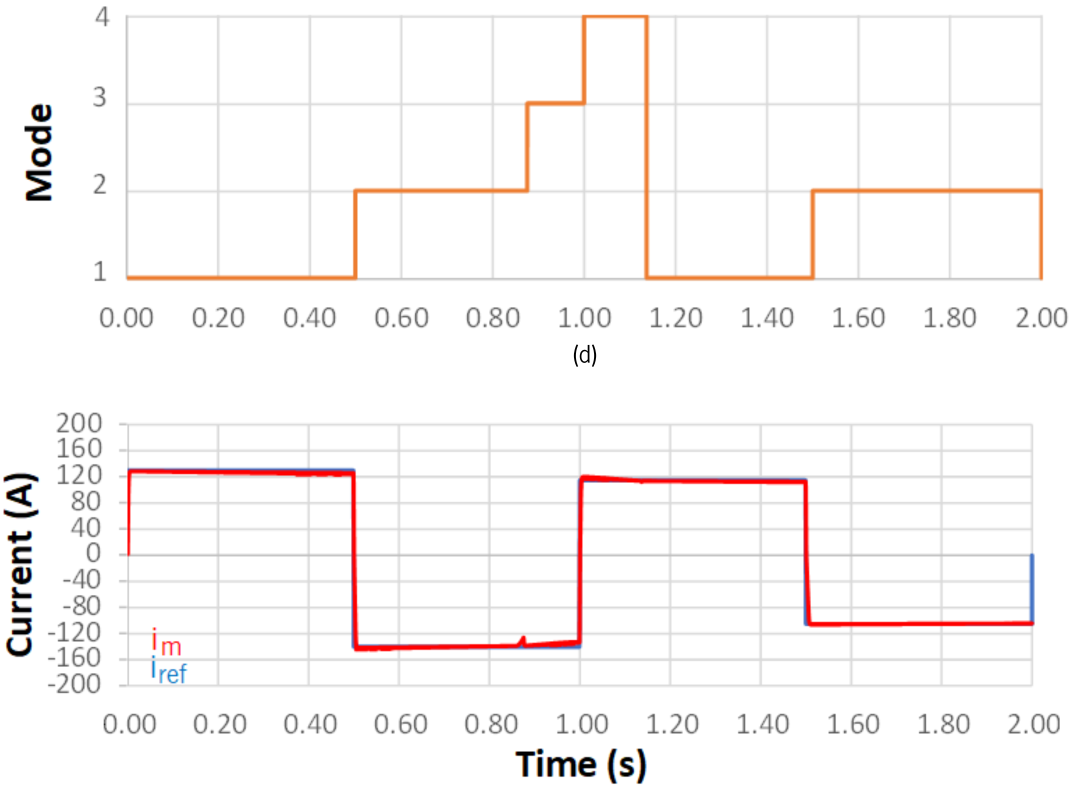

(d)

(e)

Figure 4.8: Motor simulation results with a fixed 72 V DC power supply: (a) Mechanical characteristics of the motor, speed and torque; (b) Relation between the torque performed by the motor (motor torque) and the attached load; (c) Electrical characteristics of the motor, motor current and back-EMF voltage; (d) Motor operation modes from 1 to 4; (e) Comparison between reference current and motor current.

### 4.2.5 Simulation of Regenerative Braking

In order to better evaluate the regenerative braking the traction system supplied by a 72 V battery is simulated. With this, it is possible to monitor the battery charge evolution during motor operation, and validate the regenerative braking method. In Figure 4.9 is presented the converter simulation, similar to what was presented above in Figure 4.2 but with a battery model implemented. The battery parameters were adapted so the charge/discharge can be shown in the few seconds of simulation.

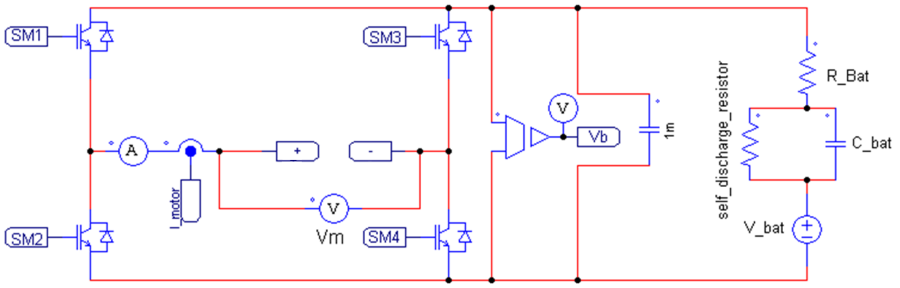

Figure 4.9: Simulation design of the motor converter supplied by a 72 V battery model.

To simulate regenerative braking it is used the same strategy from the other simulations where the input is a reference current to manipulate the speed and modes of operation. With this, Figure 4.10 (a) presents the waveform of the battery voltage ($V_{bat}$), which is analogue to the SoC. By comparing Figures 4.10 (a) and 4.10 (c), can be validated that during motoring mode the battery is discharged and during braking mode the battery recharges. It is also possible to conclude that for a greater $i_m$ the battery charge varies faster, as predicted.

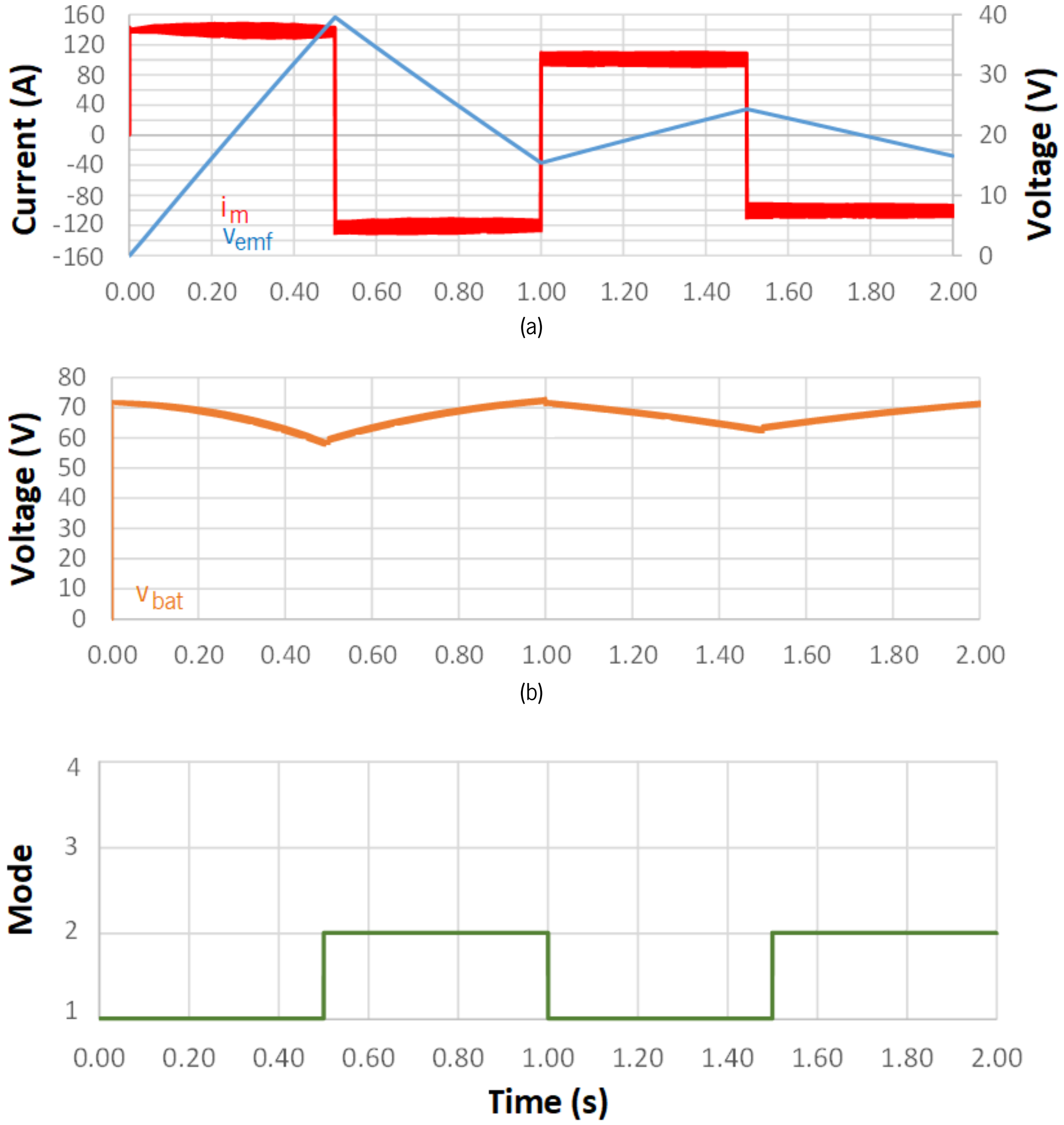

(a)

(b)

(c)

Figure 4.10: Motor simulation results with a 72 V battery: (a) Corresponds to battery voltage evolution throughout the simulation; (b) Represents the input reference current and the back-EMF voltage produced by the motor; (c) Corresponds to the mode of operation.

## 4.3 AC-DC Converter Simulation - Power Factor Correction

The AC-DC converter implemented in simulation is the passive PFC boost topology with a PI current control technique.

The requirements set for the AC-DC converter are 3 kW rated power and a DC-link voltage of 400 V. Considering the converter has an input voltage of 230 V (RMS), a rated power grid current ($i_g$) of 13.05 A (RMS).

Figure 4.11 presents the AC-DC converter, and the respective control system, including DC-link regulation, the PLL algorithm, and PWM technique. In this control strategy, the DC-link voltage ($v_{dc}$) is measured and compared to the reference value ($v_{dc\_ref}$), resulting on an error signal ($v_{dc\_error}$) that it is subjected to a PI controller. The PFC current control has as inputs a reference resulting from the DC-link voltage control ($i_{pk\_ref}$), the PLL signal produced by the PLL algorithm and the DC-side current ($i_{dc}$).

The next subsections detail the procedures highlighted in yellow on figure 4.11, concerning the DC-link voltage regulation, the system synchronization with the power grid, current control, and PWM technique.

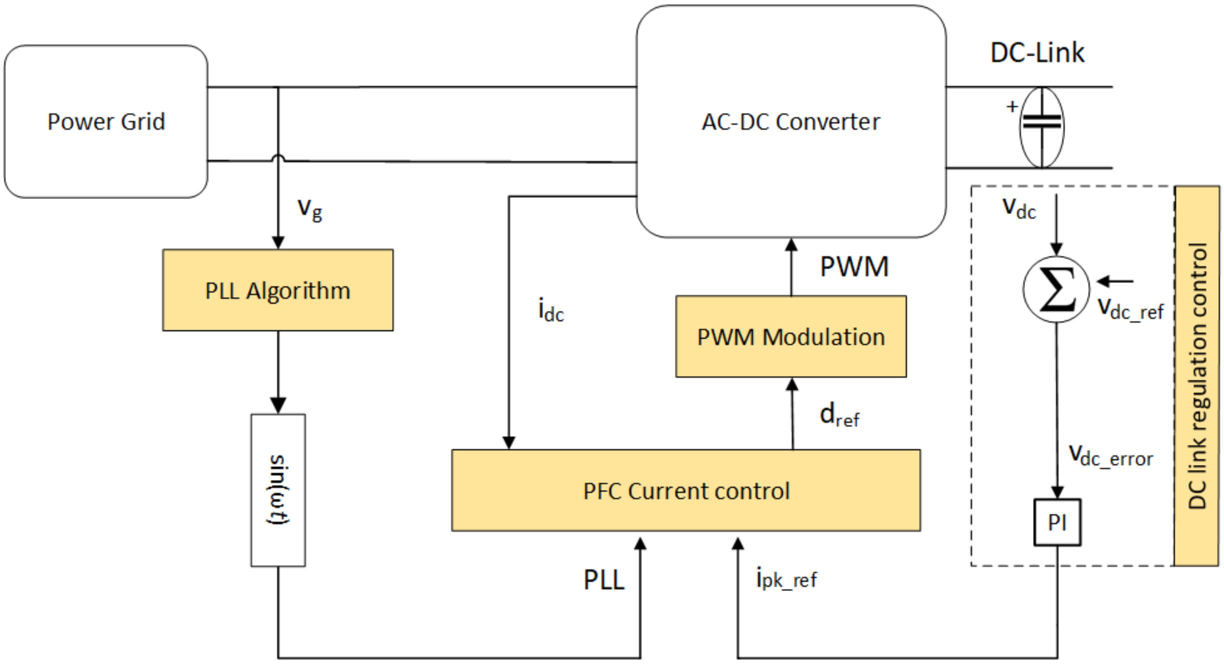

Figure 4.11: AC-DC rectifier schematic, showing the different sub-parts of the system and the overall structure of the charger module, where the control methods are highlighted in yellow.

### 4.3.1 PLL Algorithm for Power Grid Synchronization

As mentioned before, for the proper operation of the AC-DC converter it is necessary to synchronize the system with the power grid voltage. Therefore, it is used a PLL algorithm as described in section 2.4. The PLL used was proposed by Karimi and Iravani [60] and it is based on two blocks, one for the phase calculation and the other for the amplitude calculation. The system has a PI controller, with gains that directly influence the stability of the PLL and the synchronization speed. To validate the synchronization on PSIM is implemented the algorithm and the results are shown in Figure 4.12. Figure 4.12 (a) is presents the evolution of $\omega t$ angle, that composes the sinusoidal waveform sin($\omega t$), with a frequency of 50 Hz and limited between 0 and $2\pi$. From this, by application of sin($\omega t$), results a sinusoidal waveform with a unitary amplitude that when multiplied by the amplitude component of the algorithm, cos($\omega t$), it is obtained a sinusoidal waveform with the power grid peak amplitude (Figure 4.12 (b)). By analyzing Figure 4.12 (b) it is possible to verify that the PLL signal is synchronized with $v_g$ voltage and it has no harmonic distortion. In Figure 4.12 (c), it is displayed a test condition where the algorithm starts when the grid phase is 90° and after a few grid cycles the PLL synchronizes with $v_g$, although it takes more time to achieve that state compared to the situation above where power grid phase is 0°.

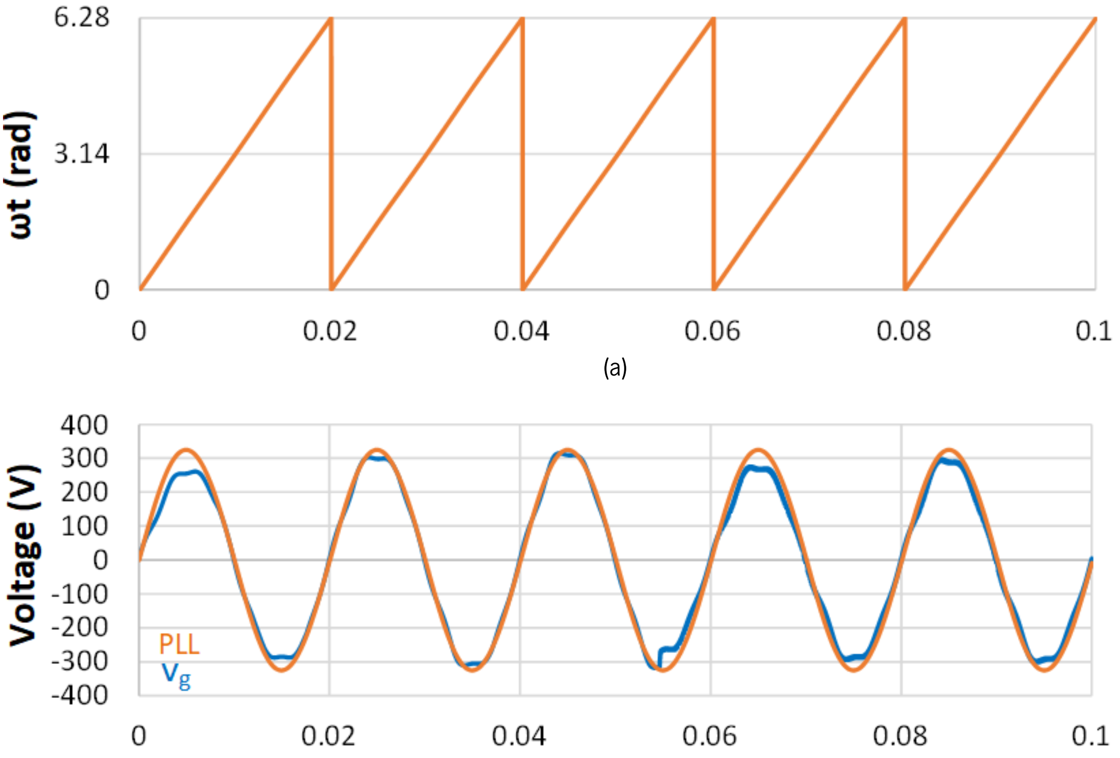

(a)

(b)

### 4.3.2 DC-Link Voltage Regulation

One of the AC-DC functions is to be able to maintain a specific voltage on the DC-link through feedback control. The output voltage of the converter can not assume values below the power grid voltage (325 V), otherwise, the bridge semiconductors (IGBTs) are inversely polarized, and due to the antiparallel diodes, the converter works as a diode full-bridge. During the process of regulation, big variations on the voltage applied to the DC-link capacitors lead to current spikes that are higher, the greater is $dv/dt$. These current spikes are called in-rush currents, and result from the capacitive nature of the converter [61],[62]. In order

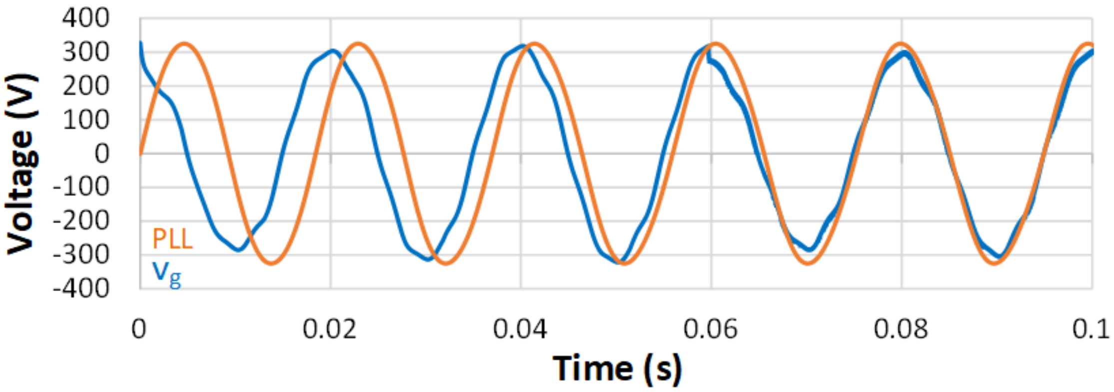

(c)

Figure 4.12: PLL algorithm simulation: (a) $\omega t$ angle with 50 Hz frequency in phase with $v_g$; (b) Waveform comparison between grid $v_g$ and the PLL wave, when the control starts at 0° power grid phase, showing they are synchronized; (c) Presents an example where the algorithm is enabled at 90° grid phase.

to smooth the voltage and current evolution during the start of the operation, it is used a bypass resistor between the power grid and the converter acts as a deterrent to the voltage growth during pre-charge. The resistor reduces the voltage variation and as a consequence, in-rush currents decrease in amplitude. The process of regulation starts with the pre-charge of the DC-link capacitors while the feedback control is disabled. Once the DC-link capacitor voltage reaches a specific value, it is made bypass to the resistor and the feedback control is enabled. In the next phase, the DC-link is regulated by a PI feedback control present in figure 4.13. The result of this control is a command signal that represents a reference current to be subsequently applied to the current control.

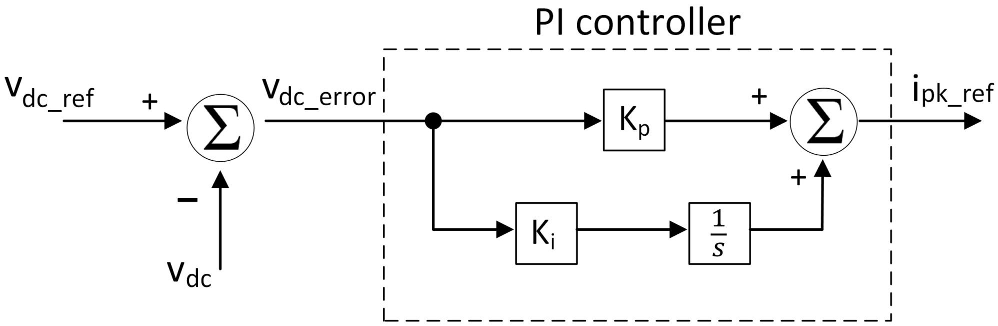

Figure 4.13: Schematic of the DC-link regulation PI control.

Figure 4.14 presents the current and voltage waveforms, $i_g$ and $v_{dc}$, obtained from simulating the regulation of the DC-link at 400 V. Figure 4.14 illustrate the three stages mentioned before, pre-charge of the DC-link capacitors, resistor bypass and regulation voltage through feedback control.

From 0.000 s to 0.045 the DC-link capacitors are being charged and to decrease the amplitude of in-rush currents it is used a 10 $\Omega$ bypass resistor, limiting the current peak at 36 A. The amplitude of the current peak can be reduced by introducing a higher value resistor, however, the voltage evolution would be slower leading to more simulation time. Also, by observing this stage, it is verified that without a current control the grid current presents a distorted waveform. Considering that during the pre-charge stage the DC-link voltage can only assume values below 325 V, it is stipulated that when $v_{dc}$ reaches 300 V, it is made bypass to the resistor and the control is enabled (0.045 s). During this transition, there is a voltage variation of 100 V (300 V to 400 V), due to the start of the control, resulting in a current spike of 28 A. The $dv/dt$ during the transition depends on the control implementation. The greater are $k_i$, and $k_p$ gains, the more aggressive is control response, causing overshoot and increasing $dv/dt$.

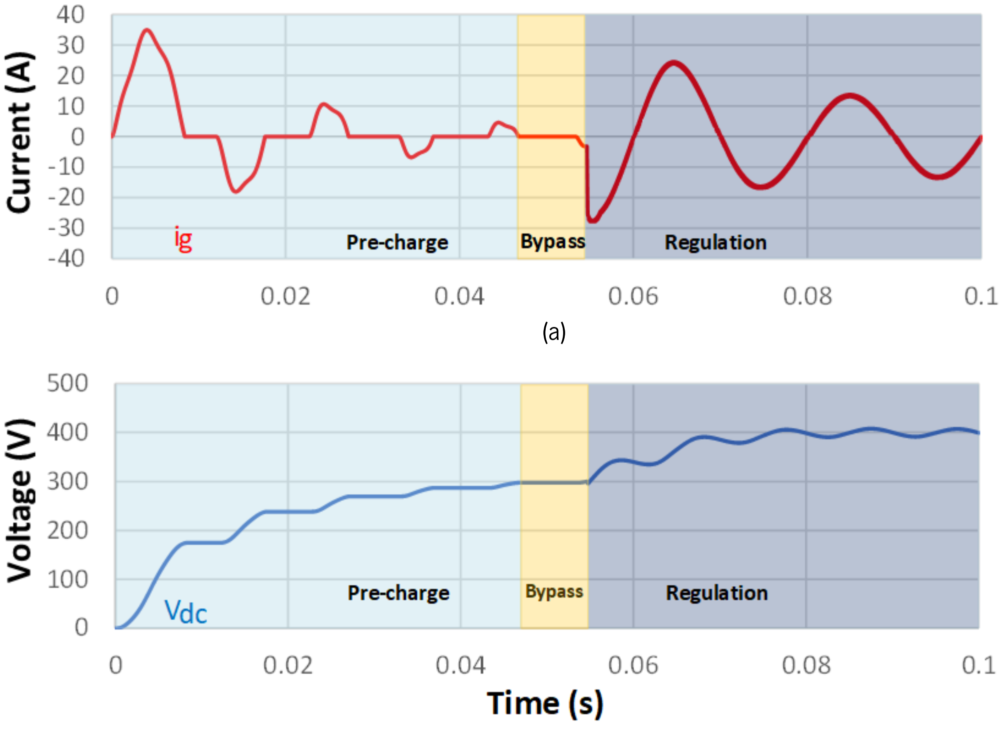

(a)

(b)

Figure 4.14: Waveform evolution of grid current $i_g$ ((a)) and DC-link voltage $v_{dc}$ ((b)) with bypass resistors and respective stages of regulation until the dc voltage reaches permanent state.

In Figure 4.15 is presented a comparison of the evolution of voltage and current between DC-link regulation with bypass resistor (blue waveforms) versus no bypass resistor (orange waveforms). By observing Figure 4.15 (a) the current peak without a bypass resistor reaches 120 A versus 36 A when it is implemented a resistor. The high current amplitude is a result from the high voltage variation present in Figure 4.15 (b), where there is an voltage overshoot, reaching 490 V and then gradually decreasing to 400 V. Comparing both solution's voltage waveforms, at 0.35 s, there is a 200 V difference between both solutions. Considering this, using a 10 $\Omega$ resistor it is possible to decrease the current peak by 70 % and limit voltage to a maximum of 400 V. This results in cheaper hardware due to lower power requirements increases the component's life expectancy and creates a safer electrical system.

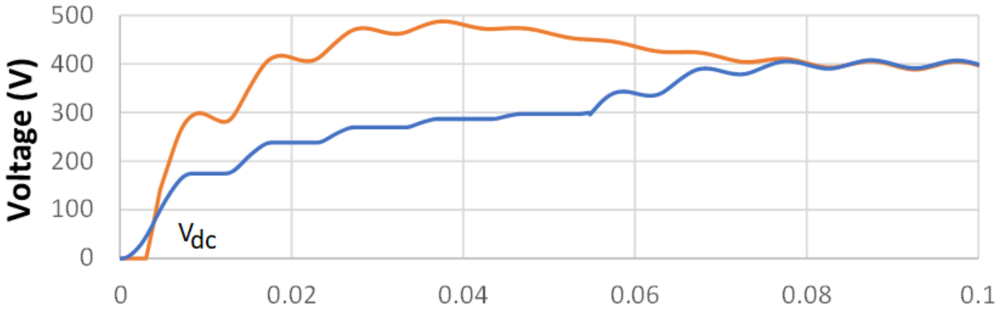

(a)

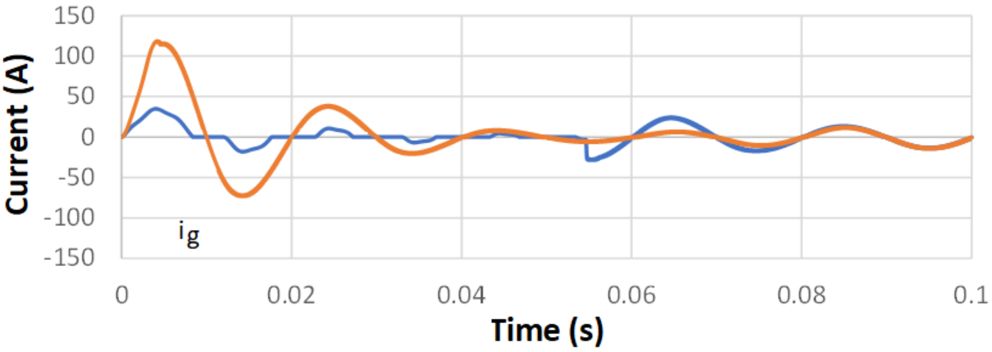

(b)

Figure 4.15: Comparison between voltage and current waveforms with and without the implementation of a bypass resistors, blue curve and orange curve, respectively: (a) Waveforms of the voltage evolution; (b) Waveforms of the current evolution.

## 4.4 PFC Current Control and PWM technique

As referred before, the current control serves as power factor correction, and reduces harmonics of the power grid current. The output of the PI controller is the reference current ($i_{pk\_ref}$) that is compared with the DC-side current ($i_{dc}$) on the PFC current control, producing a relative error (Equation 4.1). The other input of the control is the PLL signal synchronized with the fundamental of the power grid voltage ($V_g$). This component is then added to the relative error equation. The output of the PFC current control is a duty-cycle reference ($d_{ref}$) that is fed to the PWM technique and it is generated a PWM signal for the boost converter IGBT.

$$e_r = \frac{i_{pk\_ref} - i_{dc}}{i_{pk\_ref}} \tag{4.1}$$

## 4.5 DC-DC Converter - Battery Charging System

The battery charger is a DC-DC converter with charging current control. On the other hand, admitting that the battery used has a rated voltage of 100 V it is necessary a buck converter, since the primary side is connected to the DC-link (400 V). In regard to the charging control method it is opted for the constant current (CC) solution. For this, as referred before, is used a PI control that defines a reference current. Since is opted for a 3 kW charger, and it is used a 100 V battery, the rated charging current is 30 A.

## 4.6 Charger Simulation Model

The simulation model implemented is presented in Figure 4.16, with all the components of both the AC-DC and the DC-DC buck converter, as well as the coding block with the control algorithm and PWM technique. Observing Figure 4.16 is noticed the introduction of harmonics of order 1, 3, 5 and 7, which are the most prominent, and line impedance (ZL) to get a very approximate power grid voltage. It is also implemented a bypass resistor to pre-charge the DC-link. For the DC-link simulation is used a 2 mF capacitor, considering that the respective function, in conjunction with the control, is to maintain a constant voltage of 400 V with low ripple. In regards to the battery capacitor it is used a 47 $\mu$F capacitor to filter low frequency. Other than the converters it is possible to see the model of the generic battery used. Regarding the control system it is required to measure variables such as the grid voltage, DC side current, DC-link, and battery voltage, as well as the battery current. The sampling frequency opted for is 100 kHz, and 50 kHz for the switching frequency. It is opted for higher frequencies than for the motor module due to the lower power levels involved. The outputs of the coding block are the two duty-cycle references, for the PWM technique of the buck and boost IGBTs.

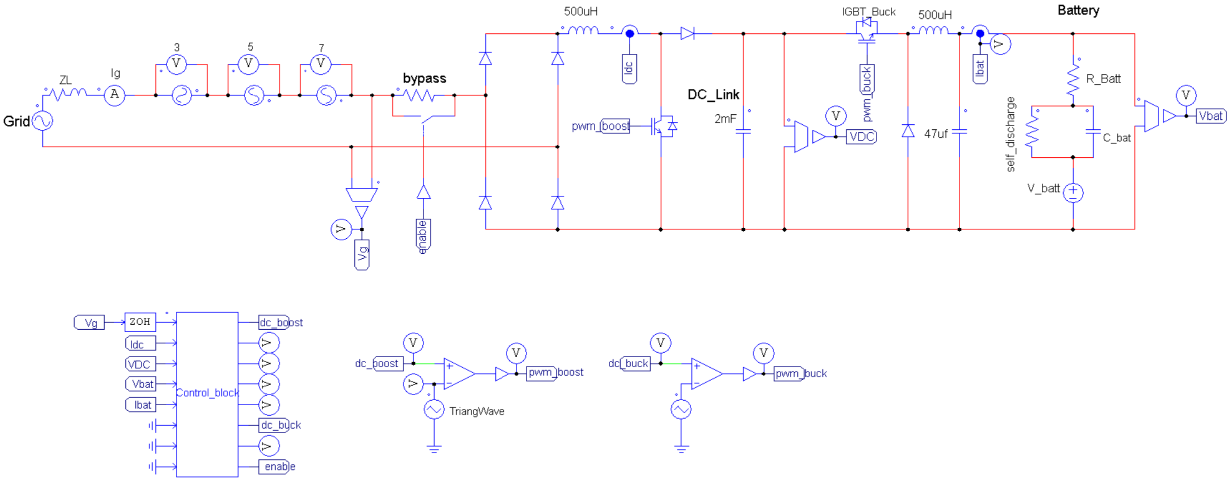

Figure 4.16: Charger system simulation design.

### 4.6.1 AC-DC Converter Simulation Results

Figure 4.17 presents the results of simulation for the AC-DC converter, displaying the waveforms of grid and reference current and DC-link voltage when the control is activated after pre-charge. Figure 4.17 (a) shows the calculated reference current (prior to the multiplication with the PLL signal) based on the DC-link regulation and the grid current resulting from harmonic compensation. In this regard, Figure 4.17 (b) shows the DC-link voltage active regulation until it stabilizes at 400 V with 5 V of ripple. . By measuring the THD$_f$ of $i_g$ is obtained a value of 0.65% concerning the fundamental waveform. Therefore it is possible to validate both DC-link regulation and current harmonics compensation. By observing Figure 4.17 (a) can also be pointed that the calculated reference current is the power grid current peak value.

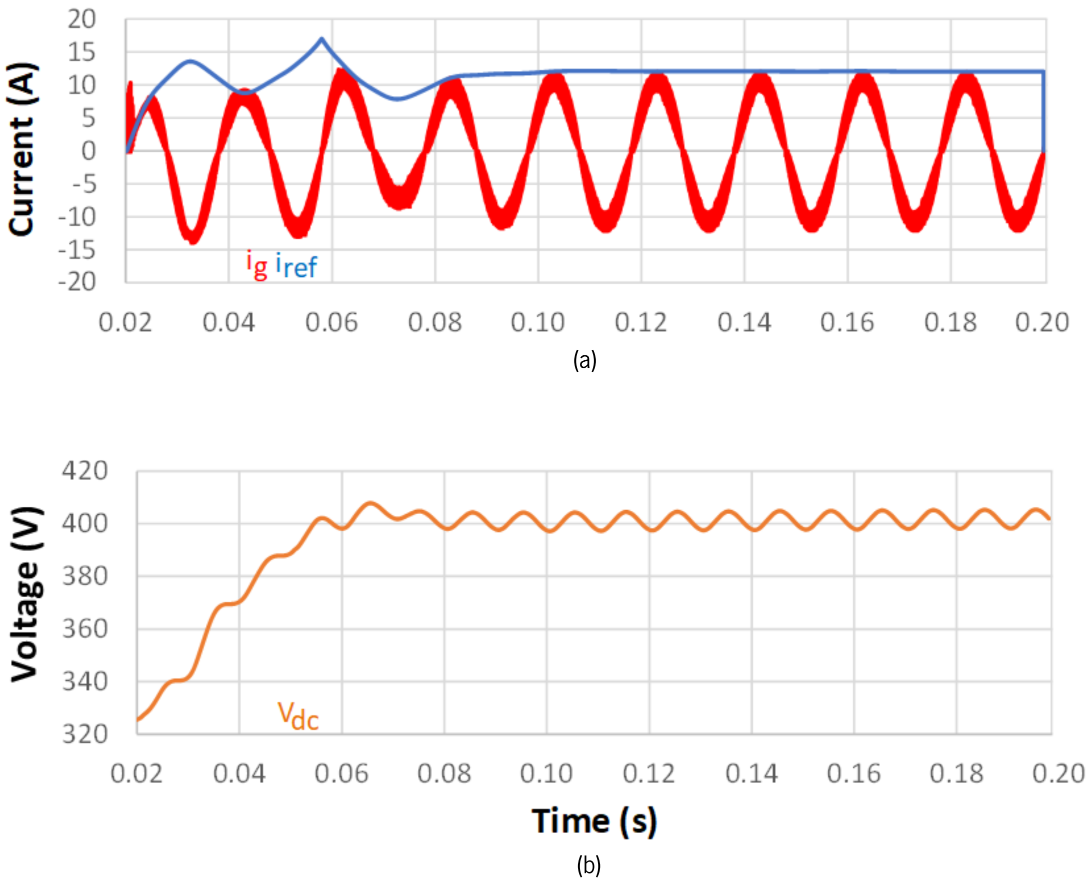

(a)

(b)

Figure 4.17: Simulation waveforms of the AC-DC converter and the respective PFC and DC-link regulation controls: (a) Power grid current ($i_g$) and reference current ($i_{ref}$); (b) DC-link voltage $v_{dc}$.

### 4.6.2 Battery Charging System Results

In order to activate the battery charging control, it is necessary to obtain a stabilized DC-link voltage. Therefore the buck converter is activated when the input voltage is higher than 390 V. The simulation results of the buck converter are shown in Figure 4.18, where are present the charging reference current ($i_{ref}$) and the battery current ($i_{bat}$), as well as the battery voltage. Figure 4.18 (a) shows the input reference current and the battery charging current. At the start of the charging process, is specified a reference of 20 A then at a later stage is lowered this value to 10 A. Figure 4.18 (b) shows the battery voltage evolution during charging, where the starting voltage is 40 V. It is also observable that during the period of higher current, the battery charges faster concerning the later stage, reaching 80 V. With this is possible to confirm the correct functioning of the PI current control.

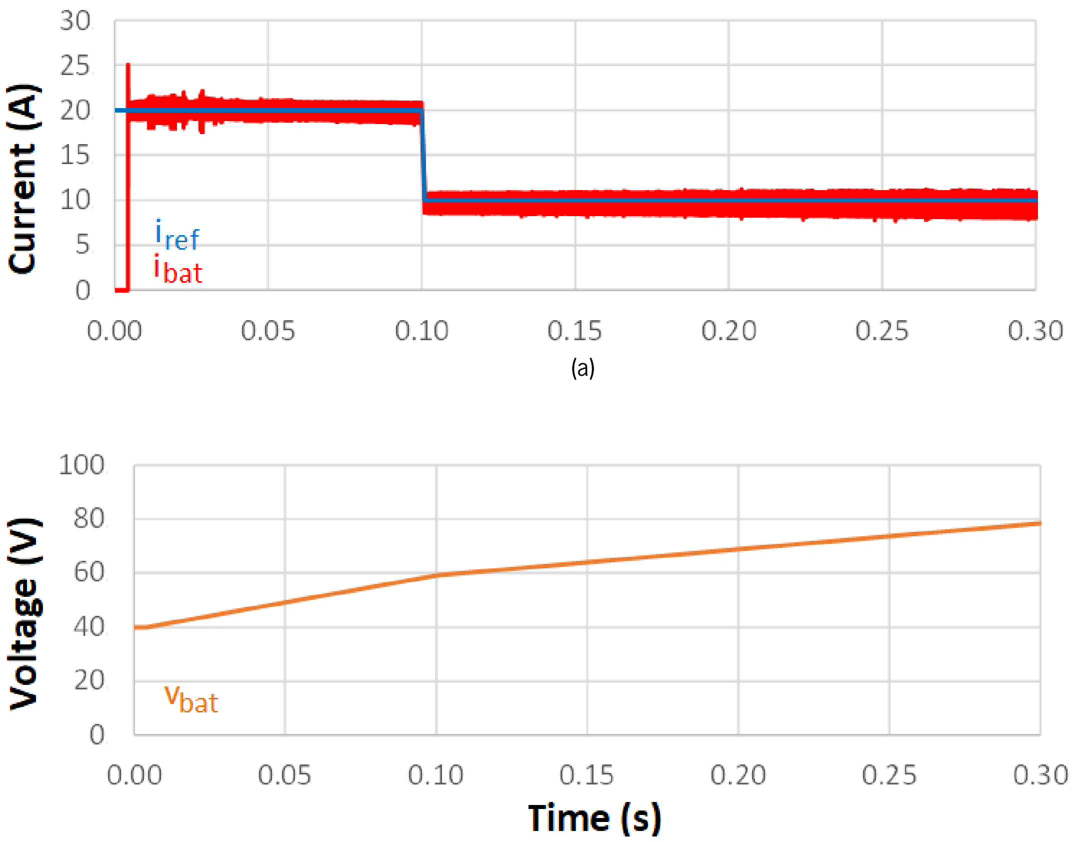

(a)

(b)

Figure 4.18: Simulation waveforms of the buck converter for charging current control.

## 4.7 Chapter Conclusion

In this chapter was described the simulation models composed of the BDC motor and the respective converter and control techniques, as well as the PFC and battery charger converters. It was also presented justification for the topologies implementation, and then validated these solutions. The motor and battery charger simulation models were developed independently from each other, and they are both subdivided into the converter itself with all the components and connections, and the control system, with the coding block containing the control algorithms and PWM technique. With this, it was presented intermediate simulation results detailing step by step the gradual implementation of the simulation models, such as, DC-link regulation and system synchronization with the power grid. Relative to the motor module, it was possible to validate the torque/current control utilized by observing the controlled current tracking the respective reference. By observing the waveform results it was validated the mode detection based on $i_{ref}$ and $V_{emf}$, and by comparing $i_m$ with the speed evolution it was concluded that the motor current is proportional to the acceleration/torque. To validate the regenerative braking it was used a battery model to be possible to visualize the discharge/charge during motoring and braking. From this, it was observed that the higher was the value of the motor current the greater was the charge/discharge of the battery. Concerning the charger system, it was first implemented the PFC converter, starting with the PLL validation. Thereafter, it is implemented the DC-link regulation PI control and shown the impact on the voltage evolution by using a bypass resistor during pre-charge. Then it was shown the overall PFC converter operation, where it was obtained in the simulation a grid current waveform with 0.6% THD$_f$ as well as the DC-link regulation with a 20 V ripple around the 400 V reference. After the PFC, it was simulated the buck charger converter, composed of a PI control that stipulates a charging current. In waveform results, it was concluded that current control is correctly implemented, and the SoC evolution is as expected in theory.

# Chapter 5

# Traction and Charging Systems Implementation

## 5.1 Introduction

For the implementation of the hardware, the process has been divided into two main strands: the control system and the power system. Thus, throughout this chapter, it is detailed the implementation of the hardware relating to the control system, composed of sensors for acquiring the measurable quantities necessary to implement the control theories, signal conditioning circuits, driver circuits necessary for the performance of the power semiconductors, a unit that controls the whole system - the DSP (Digital Signal Controller). Later on, it is covered the power system, the ME1003 BDC motor is presented, followed by the converter topologies (Charger and Motor) implemented, the respective semiconductors, passive elements such as DC-link capacitors, inductors, and overvoltage/overcurrent protections are described.

## 5.2 Control System Implementation

In this section, it is presented all PCBs developed, from signal conditioning and detection of errors to driver circuits for the semiconductors and power boards. On top of that, the hardware and boards previously developed and validated are described, which were re-utilized in the context of this thesis.

Along with the next topics, it is going to be presented the hardware relative to the control system in which belongs current sensors for acquisition of the measurable variables, necessary for implementing the control theories, conditioning signal circuits, processing boards required for operating power semiconductors, and a DSP to calculate multiple variables of every control theory based on the input from the measured variables.

In Figure 5.1 is presented a schematic of the system proposed in this thesis in order to map and better understand the diverse modules and relations between them.

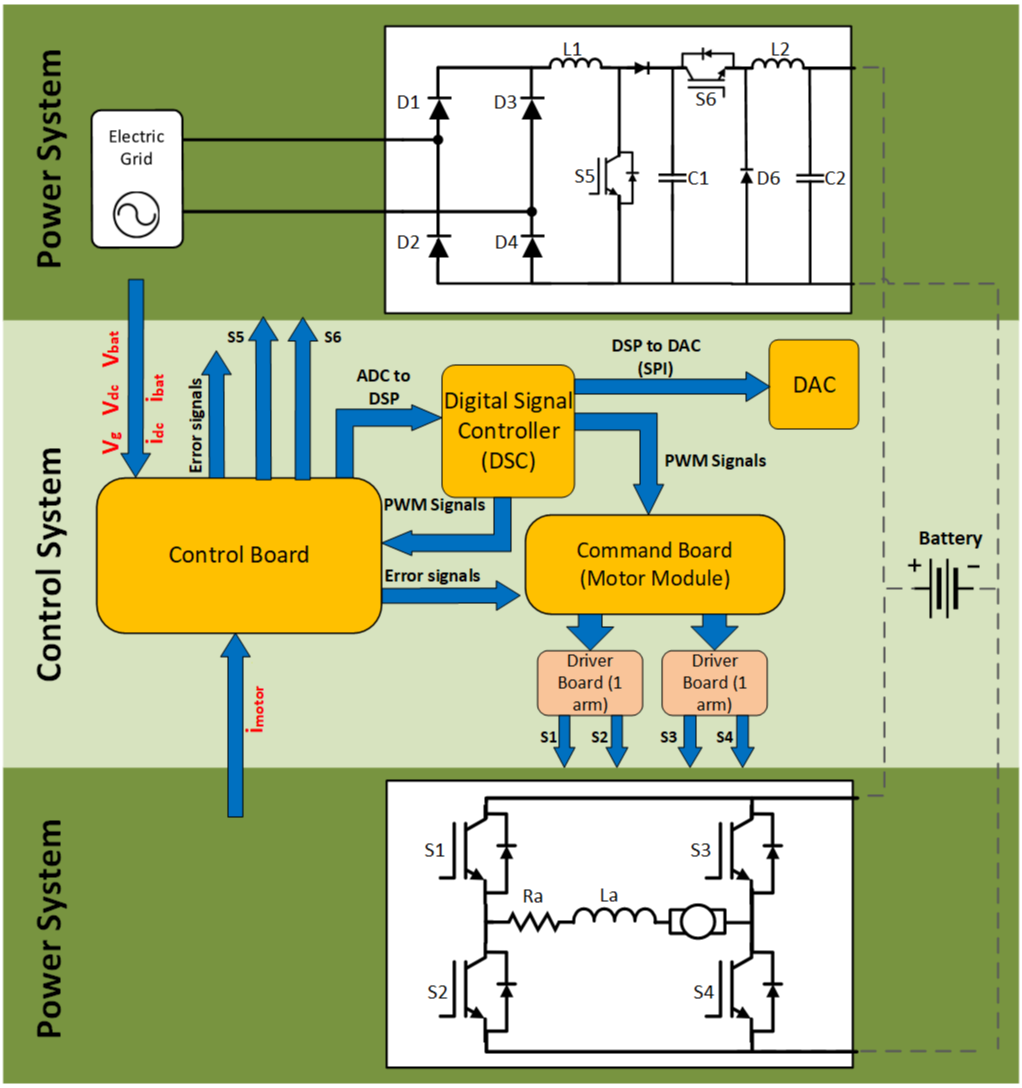

Figure 5.1: Simplified schematic of the motorcycle prototype.

### 5.2.1 Digital Signal Controller (DSP)

To control the processes intrinsic to the correct functioning of the whole system, a development platform based on DSP from Texas Instruments has been used, in particular the model TMS320F28335 which has a 32-bit processing unit with floating-point and a 150 MHz clock frequency. As main peripherals, it has a Serial Peripheral Interface (SPI) module; 3 32-bit timers each; 18 PWM outputs; 16 12-bit ADC channels; 88 General Purpose Input/Output (GPIO) pins, of which 64 can be associated to one of 8 external interruptions [63]. The microcontroller card comes with a docking station TMDSDOCK28335 (Figure 5.2 (b)) that contains the USB JTAG programmer used to program and debug the DSP code, establishing the interface with the computer. In order to facilitate and simplify the use of some of the DSP's features and capabilities, GEPE (Group of Power Electronics and Energy) researchers have designed the board displayed in Figure 5.2 (a) where the TMS320F283355 microcontroller card is inserted. This board requires a +5 V power supply that can be delivered via a JACK connector or a 2-pin connector. On this board, the control card is connected through a 100-pin DIMM (Dual Inline Memory Module) socket. Of the 18 PWM outputs that the DSP has, 12 can be accessed via 2 male 14-pin plugs (6 PWM outputs on each plug). Each of these plugs has been connected to a control board to convert the 3.3 V amplitude PWM signals coming from the DSP into amplitude signals suitable for the control of the rectifier and inverter power semiconductors. In addition to these, 3 more male plugs are used: one of 26 pins used for communication with an external ADC; one of 14 pins needed to program the DSP, through the TMDSDOCK28335 board, and finally, a 10-pin male plug where the GPIOs are configured as outputs in order to establish some commands needed for system operation through the Input/Output board. In addition to the male plugs, the board also has two DB9 plugs, one used for the SPI communication protocol, to which the DAC board is connected, and the other for the RS232 serial communication protocol or for using the EQEP (Enhanced Quadrature Encoder Pulse) module used to read the sensor for measuring the rotor speed. The C language programming, as well as debugging, is done through the Code Composer Studio v7.3.0 development environment (Figure 5.2 (c)), also from Texas Instruments.

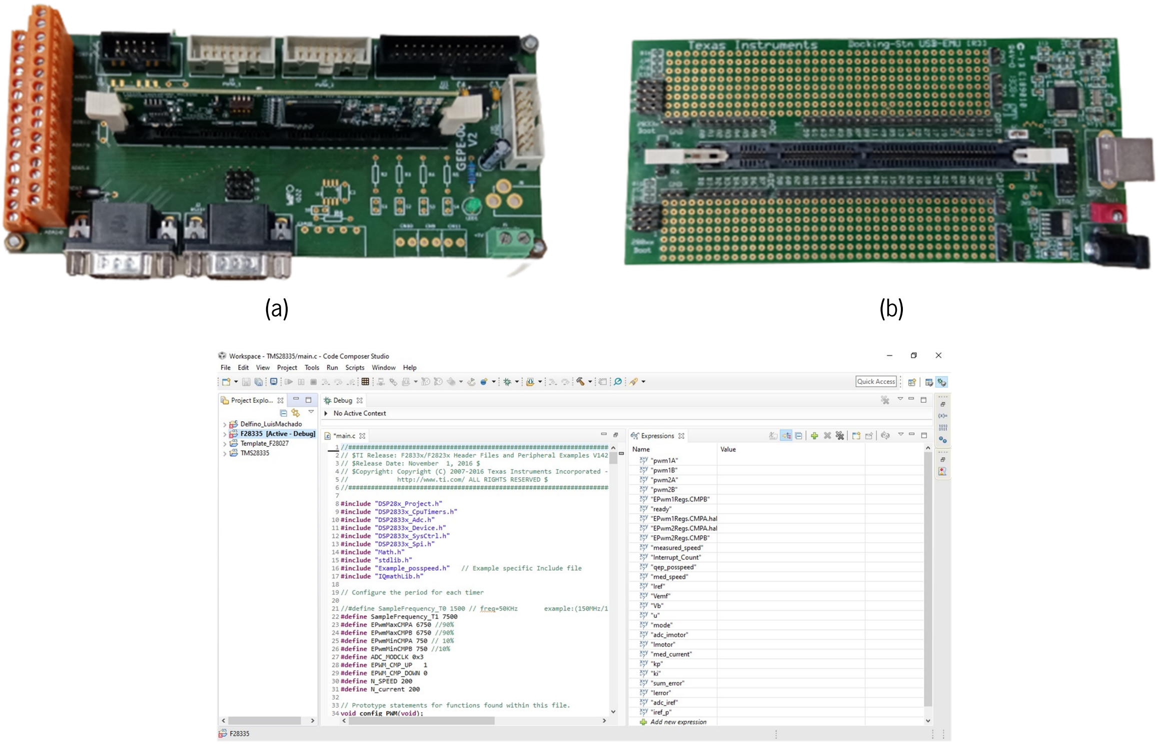

```
//##########################################################################
// $TI Release: F2833x/F2823x Header Files and Peripheral Examples V142
// $Release Date: November  1, 2016 $
// $Copyright: Copyright (C) 2007-2016 Texas Instruments Incorporated -
//             http://www.ti.com/ ALL RIGHTS RESERVED $
//##########################################################################

#include "DSP28x_Project.h"
#include "DSP2833x_CpuTimers.h"
#include "DSP2833x_Adc.h"
#include "DSP2833x_Device.h"
#include "DSP2833x_SysCtrl.h"
#include "DSP2833x_Spi.h"
#include "Math.h"
#include "stdlib.h"
#include "Example_posspeed.h"   // Example specific Include file
#include "IQmathLib.h"

// Configure the period for each timer

//#define SampleFrequency_T0 1500 // freq=50KHz       example:(150MHz/1
#define SampleFrequency_T1 7500
#define EPwmMaxCMPA 6750 //90%
#define EPwmMaxCMPB 6750 //90%
#define EPwmMinCMPA 750 // 10%
#define EPwmMinCMPB 750 //10%
#define ADC_MODCLK 0x3
#define EPWM_CMP_UP   1
#define EPWM_CMP_DOWN 0
#define N_SPEED 200
#define N_current 200

// Prototype statements for functions found within this file.
void config_PWM(void);
```

```
"pwm1A"
"pwm1B"
"pwm2A"
"pwm2B"
"EPwm1Regs.CMPB"
"ready"
"EPwm1Regs.CMPA.hal
"EPwm2Regs.CMPA.hal
"EPwm2Regs.CMPB"
"measured_speed"
"Interrupt_Count"
"qep_posspeed"
"med_speed"
"Iref"
"Vemf"
"Vb"
"u"
"mode"
"adc_imotor"
"Imotor"
"med_current"
"kp"
"ki"
"sum_error"
"Ierror"
"adc_iref"
"iref_p"
```

(a) (b)

(c)

Figure 5.2: DSP and the respective peripheral boards, as well as the programming software used: (a) TMS320F283355 card integrated on the developed board by GEPE; (b) TMDSDOCK28335 docking station; (c) Code Composer Studio programming environment.

### 5.2.2 Voltage Sensors

The implemented control theory for the AC-DC converter makes use of three voltage sensors to measure the power grid, DC-link, and battery voltage.

The voltage sensors used are Hall-effect sensors, more specifically, the CYHVS5-25A. These sensors have a rated input of 1500 V RMS and are capable of measuring voltages up to 2000 V peak with a precision of ±0,5 % and a linearity deviation of 0,2 % [64]. Moreover, this sensor possesses galvanic insulation up to a maximum voltage of 2500 V between the primary and secondary. This is an important characteristic regarding the minimization of security risks during experimental tests, allowing isolation between the power circuit and the DSP. CYHVS5-25A sensors have a similar function to a transformer, presenting a turns ratio of 5:1, granting a primary RMS current $i_r$ of 5 mA and 25 mA on secondary $i_s$ [64]. Considering that the sensor output is obtained in current, it is necessary to use a measurement resistor ($R_m$) on the secondary side to obtain a voltage output. This is also necessary for other types of sensors that have current outputs. Figure 5.3 shows the CYHVS5-25A packaging used (Figure 5.3 (a)), as well as the electric schematic recommended on the datasheet (Figure 5.3 (b)) [64].

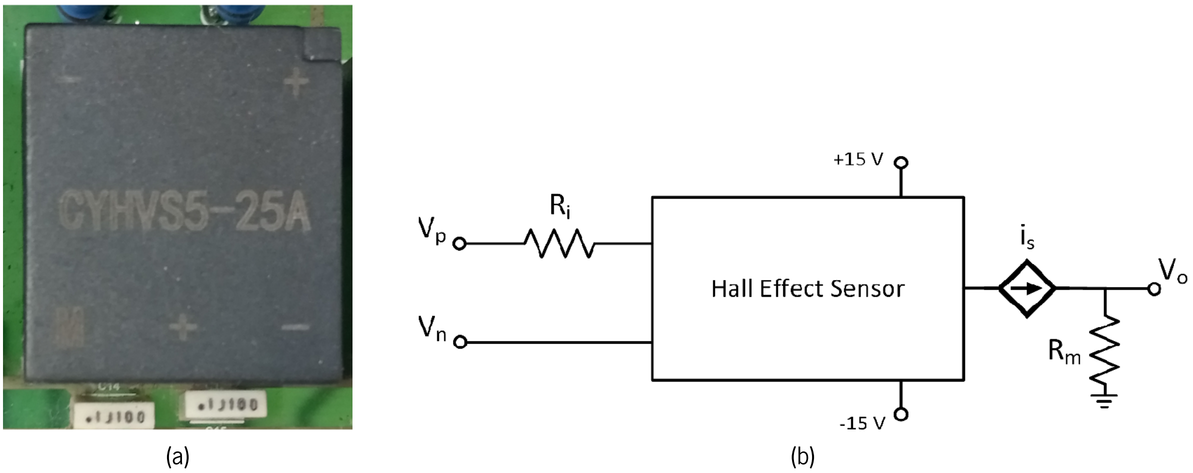

(a) (b)

Figure 5.3: CYHVS5-25A sensor: (a) Picture of the sensor encapsulation; (b) Application schematic of the voltage sensor.

For the sensor's input it is recommended to use a resistance $R_i$ to guarantee that the current $i_p$ does not surpass the rated current of 5 mA. Equation 5.1 expresses $R_i$ calculation, where $V_m$ is the intended maximum voltage to be measured.

$$R_i = \frac{V_m}{i_r} \tag{5.1}$$

Another aspect to take into account is $R_i$ dissipated power $P_{Ri}$, which can be obtained through the Equation 5.2. Considering this, it is a good strategy to use two resistance in series, dividing the dissipated power.

$$P_{Ri} = R_i \, i_p^2 \tag{5.2}$$

This is followed by determining the input resistors, starting with the sensor responsible for measuring the mains voltage. Knowing that the RMS value of the mains voltage under normal operating conditions is in the range between 230+6% V and 230-10% V and taking into account the standard values of resistances, two resistors of 27 k$\Omega$ are used in series, making up an input resistance $R_i$ of 54 k$\Omega$. Based on Equation 5.3 it is possible to calculate $R_i$ considering the nominal voltage that the sensor is going to measure.

$$V_n = R_i \, i_N \tag{5.3}$$

Since the primary's nominal current $I_N$ is 5 mA RMS, the nominal voltage of the mains voltage sensor is 270 V RMS, which allows the reading of instantaneous voltage values up to approximately ±381.84 V. For the DC-link voltage, and taking into account the most appropriate standard value available, two 47 k$\Omega$ series resistors are used. Applying Equation 5.3, it can be concluded that the nominal measured value is 470 V RMS, corresponding to approximately 661.68 V peak. Considering this value is far greater than the circuit nominal voltage, this sensor has a lower sensibility. Although, the instrumentation circuit relative to this sensor can compensate for the unused range. Finally, for the battery voltage sensor the resistance used is 15 k$\Omega$, which allows a nominal reading voltage of 150 V RMS. Subsequently, in case of different system requirements (e.g battery swap, or higher DC-Link voltages), these resistance values can be replaced to accommodate other voltage levels.

### 5.2.3 Current Sensors

Similar to voltage sensors is necessary to utilize current sensors to measure and the system's physical quantities. Therefore, is needed three current sensors, two for the battery charger system to measure the current on the DC side (right after the DFB) and for the battery current, and another for the motor system to measure the respective current. Regarding the charger system, it is used the LTS 25-NP sensor to measure the current n the DC side. LTS 25-NP is a current transducer with galvanic insulation. This sensor can measure currents up to $25$ A, however, at the expense of a lower measurement range, it is possible to achieve a better sensibility by adding more turns around the sensor [65].

Opposite to the voltage sensor, LTS 25-NP does not need measurement resistances since the output is in voltage [65]. The output voltage $V_{out}$ is given by Equation 5.4 where $i_{PN}$ is the current on primary, $i_P$ the instantaneous current measured and $V_{ref}$ a voltage reference of 2.5 V.

$$V_{out} = V_{ref} + 0.625 \, \frac{i_P}{i_{PN}} \tag{5.4}$$

By default, $i_{PN}$ is equal to 25 A, but adding turns around the conductor modifies this value. For the specific case of the LTS 25-NP sensor, three possible implementations are providing three different nominal current values of ±25 A, ±12 A, ±8 A, corresponding to one, two, and three turns on the primary conductor. With this, the number of spirals and the measuring range can be adjusted to the current to be measured. Taking into account that the nominal current measured by this sensor is 13 A, is opted for 1 primary turn providing a primary nominal current of ±25 A.

Regarding the battery charging current and the motor, the current sensor opted is the LA-100-P and LA-200-P sensors, respectively. These sensors have the same working principle only differing on the electric characteristics and measuring ranges. The difference from this sensor to sensors similar to the LTS 25-NP is that, this one does not measure the current directly, instead it measures the magnetic field created by the conductors passing its nucleus. The LA-100-P sensor can measure up to ±150 A, with a nominal primary value of 100 A $i_P$. On the secondary side, the sensor presents a nominal current of 50 mA that corresponds to a transformation ratio of 1:2000 [66]. Concerning the LA-200-P the measuring range is ±300 A, with a nominal primary value of 200 A and on the secondary side a nominal current of 100 mA and the same transformation ratio of the LA-100-P [67]. Similar to the voltage sensor shown, the LA200-P current sensor also has a measured value given in current at its output, so it is necessary to use a measurement resistance $R_m$ to obtain its voltage equivalent. In Figure 5.4 it is possible to observe the encapsulation of the LA current sensor series (Figure 5.4 (a)) used as well as the application scheme recommended by its manufacturer (Figure 5.4 (b)).

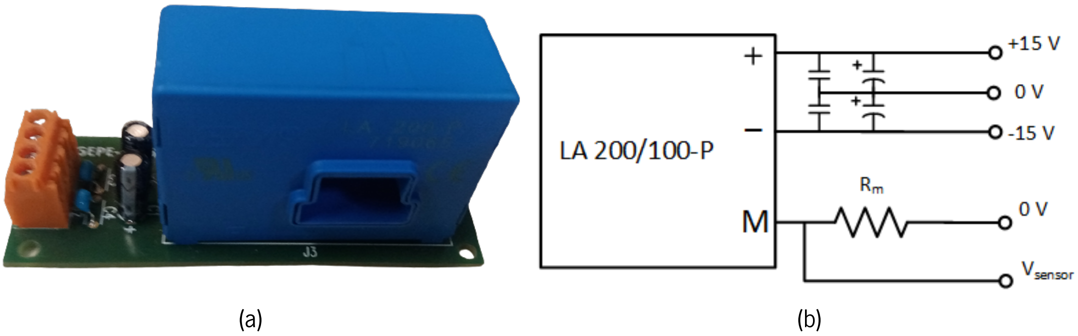

Figure 5.4: LA current sensor series: (a) generic application board and encapsulation of a LA current sensor series; (b) application schematic of the LA sensor.

Considering the nominal current values to be measured by these two sensors, it is needed to determine the number turns for the primary current to adjust the measuring range and increase their sensibility. Regarding the LA-100-P, the sensor measures the charger output current that is applied to the battery. For the characteristics presented in the simulation chapter, this current value presents a maximum of 30 A. Therefore for a 100 A $i_{PN}$ sensor is recommended to use three primary turns, providing a measuring range of ±33 A. On the motor system, considering that the motor current can reach up to ±200 A, the LA-200-P only requires one primary turn.

### 5.2.4 Sensor for Measuring the Rotor Speed

The implemented motor control technique requires the input of $V_{emf}$. Since it is not possible to measure this voltage directly, is calculated by acquiring the instantaneous speed, following Equation 3.6. To measure the motor rotation speed is used the hall effect magnetic sensor AM512B produced by RLS [68]. The sensor is an angular magnetic encoder used for motor motion control, flow measurement, and positioning applications [68]. The AM512B is accompanied by the RMK1B evaluation board with all the necessary components. According to the datasheet, the sensor has different output configurations [68]. For this application is configured the output to incremental, which means the outputs are three signals A and B, shifted by 90°, and Z that counts every turn. Taking into account that the sensor generates 128 pulses ($n_{pulses}$) for each turn, this results in an incremental encoder where speed is determined based on the frequency of A or B signals ($f_{signal}$), as shown in Equation 5.5. The direction of rotation is given by the order in which A and B appear, e.g. the direction is positive when the A signal advanced in relation to B and negative when the opposite is true. According to the AM512B datasheet, the amplitude of the output signals is given concerning the voltage value with which it is supplied, which is between 4 V and 7 V. However, the digital pins of the DSP only support signals with a maximum amplitude of 3.3 V. Therefore, it is necessary to implement a signal conditioning circuit to shift the voltage to acceptable values. The circuit implemented is a simple voltage divider that is illustrated in Figure 5.6 and is described in the next section, as part of signal conditioning.

$$speed(rpm) = \frac{60\, f_{signal}}{n_{pulses}} \tag{5.5}$$

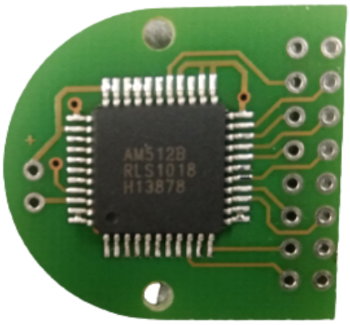

Figure 5.5: Picture of the AM512B sensor integrated with the evaluation board RMK1B.

### 5.2.5 Control Board - Signal Conditioning

The sensors shown above have analog output signals that must be converted to digital signals to then be processed by the DSP. For this purpose, it is required an Analog-to-Digital Conversion (ADC) module. The DSP is an integrated ADC Module with a reading range between 0 V and 3 V, which can be different from the output obtained by the sensors. On top of that sensors that measure negative currents/voltages require the implementation of an offset since the ADC can not read negative values and might be damage. Therefore, it is essential to implement signal conditioning circuits. From the sensors described before, only the power grid voltage and the motor current sensors are subject to negative values and need additional instrumentation to implement an offset. Regarding the other four sensors, they only require a voltage divider to shift the sensor output value to the range accepted by the ADC. In Figure 5.6 is displayed the voltage divider instrumentation where the measurement resistor is represented by $R_1$ and $R_2$. This is justified by the presence of a minimum and maximum resistance value on the output of the sensor that is specified on the respective datasheet.

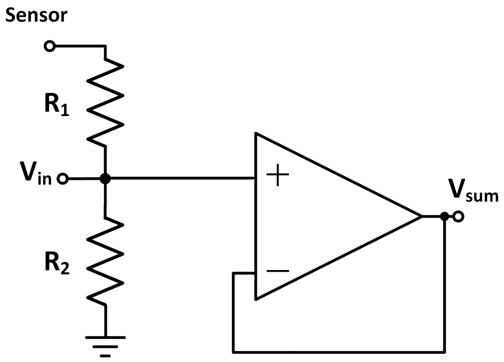

Figure 5.6: Voltage divider schematic.

For the sensors referred above that require an offset is needed to add more components to the circuit in Figure 5.6. Therefore, a non-inverting amplifier assembly using an operational amplifier (AMPOP) is used to move the signal measured by the sensors to the desired ADC range. This circuit has the benefit of not inverting the input, however, it poses an additional difficulty in adjusting the gain and offset, since it is not possible to establish the two parameters independently. Figure 5.7 is presented the measurement resistors and subsequently the non-inverting amplifier.

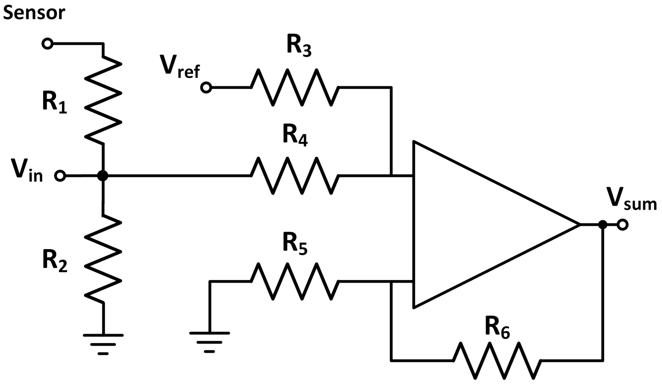

Figure 5.7: Schematic of the non-inverting amplifier for offset addition.

Since this circuit is a non-inverter, the input signal is connected to the non-inverting AMPOP input. To add the desired offset, it is essential to use a voltage source with a very precise value. For this purpose is opted to use the LT1009 component from Texas Instruments, capable of maintaining a regulated output voltage of 2.5 V with a maximum deviation of ±5 mV [69]. Equation 5.7 represents the output voltage provided by the assembly ($v_{sum}$) as a function of the input voltage ($v_{in}$) and the voltage reference used ($V_{ref}$).

$$V_{sum} = (1 + \frac{R_6}{R_5})\,(\frac{R_3}{R_3 + R_4}\,V_{ref} + \frac{R_4}{R_3 + R_4}V_{in}) \tag{5.6}$$

To simplify the implementation of the circuit, it is considered $R_5 = R_6$. Therefore, the first term of the expression is equal to 2. As mentioned, the gain and the offset are not independent, therefore, priority is given to the offset value. The offset can be calculated using the Equation 5.7.

$$V_{offset} = (1 + \frac{R_6}{R_5})(\frac{R_3}{R_3 + R_4 V_{ref}}) \tag{5.7}$$

Considering that the ADC reading range is from 0 V to 3 V the recommended offset is 1.5 V, where values bellow are considered negative voltages or currents, respective to the sensor in question. To obtain 1.5 V from the 2.5 V voltage reference, it is implemented another voltage divider composed by $R_3$ and $R_4$ (Figure 5.7), where $R_3/R_4$ = 3/7. Taking into consideration the standard resistance values, it is opted for $R_3$ = 24 k$\Omega$, $R_4$ = 56 k$\Omega$. For the both resistors $R_5$ and $R_6$ it is elected a value of 10 k$\Omega$, being the most relevant aspect the ratio between the two. After the offset is defined, it is established the circuit's implicit gain. Simplifying Equation 5.7 is possible to obtain Equation 5.8, expressing the operation carried out by the non-inverting amplifier. Observing Equation 5.8 is verified that the circuit introduces a gain of 1.4.

$$V_{sum} = 1.4 V_{in} + 1.5 \tag{5.8}$$

Accordingly, with the circuits Equations obtained, it is then determined the value of the measurement resistors $R_1$ and $R_2$ for each sensor. The CYHVS5-25A voltage sensor datasheet shows that the measurement resistance can not assume a random value and must be within the range of 100-350 $\Omega$. However, a measuring resistance with a value situated on this range would have a voltage drop the sum and amplification of which would result in a voltage of more than 3 V, making it unreadable and may even damage the internal ADCs of the DSP. For this reason, two resistors are used in series to make up a total resistance following the range required by the sensor and to obtain readable voltage values for the ADCs and with the most appropriate range possible. Regarding the determination of the input resistances done in section 5.2.2, the grid voltage sensor of the charger has a measuring range of ±381.84 V approximately, so this range can be slightly reduced. Applying Equation 5.8 and opting for $R_2$ = 33 $\Omega$, is possible to obtain a voltage of 3 V on the respective ADC input. At the same time, 3 V on the ADC corresponds to a voltage measured by the sensor of approximately 350 V, which allows the measurement of a peak value 6% higher than the mains nominal value as tolerated by legislation. In order to make a measurement resistance within the range required by the sensor, it is opted for $R_1$ = 120 $\Omega$. Relative to DC-link and battery voltage sensors, since both are measure DC voltages always positive values, the use of the adding amplifier can be exempted. Therefore, the voltage acquired by the respective ADC is obtained by the voltage divider formed by the two measuring resistances. It should be remembered that the voltage sensor range on the DC-link has a exaggerated value (the maximum value allowed by the measurement is 661 V), so it is important to reduce it to obtain a higher reading sensitivity. As such, $R_2$ = 120 $\Omega$ and $R_1$ = 30 $\Omega$ provides a voltage drop of 3 V when the sensor measures a voltage of 470 V on the DC-link. Concerning the battery voltage sensor, the nominal value is 100 V. Assuming $R_1$ = 30 $\Omega$ and$R_2$ = 180 $\Omega$, a voltage of 3 V is obtained in the ADC when the voltage in the batteries is approximately 150 V. For the current sensor LA-100-P, the nominal current measured at the battery is 30 A, then, opting for $R_2$ = 60 $\Omega$ allows a maximum current of 33 A that corresponds to 3 V on the ADC. Regarding the current sensor LA-200-P, it can measure a motor current of

±200 A, and similar to the power grid voltage sensor it requires the addition of an offset. Therefore applying Equation 5.8 it can be determined that $R_2$ = 30 $\Omega$.

As referred before, the LTS 25-NP current sensor is the only sensor used that has an output given in voltage. The sensor only measures positive values, therefore is exempted from the use of an offset and the only adjustment to be made is the attenuation of the sensor output voltage. As shown in Equation 5.8 the LTS 25-NP has a voltage reference of 2.5 V and it is verified that the output can assume values from 2.5 V and 3.75 V. Since 3/3.75 = 0.8, is obtained that the sum of the resistances is equal to 1.25 times the resistor of higher value. In addition, it is necessary to make an analog filter of the obtained signals, in order to diminish the high frequency noise and avoid bad readings for the ADC. With this in mind, it is implemented a Low-Pass Filter (LPF) to then be placed on the ADC channel input of the DSP. Based on Equation 5.9 it is possible to determine the cutoff frequency $f_c$ of the filter.

$$f_c = \frac{1}{2\pi RC} \tag{5.9}$$

By setting a cut-off frequency of 20 kHz and a capacity of 10 nF, it is obtained a resistance of approximately 795.77 $\Omega$. It is important to note that it should have opted for a cutoff frequency a few decades above the maximum signal frequency to minimize phase deviation. On the other hand, if the cutoff frequency is too high, any noise present in the signal will not be eliminated, so a compromise relationship must be maintained between the two factors.

On top of that, it is utilized voltage follower, or buffer amplifier, placed after the voltage divider, and before the LPF. This implementation does not provide any gain to the circuit, but it introduces a high impedance, operating as isolation and providing protection to the DSP. In addition to the above elements, to protect the DSP from over-voltages is inserted a zener diode on the circuit output. On top of that, the zener connection protects against negative voltages. Having said that, Figure 5.8 presents the schematic of the voltage follower with passive filter and a zener diode, where $V_{sum}$ represents the output voltage of the signal conditioning circuit of the respective sensor and $V_{ADC}$ the voltage that will be effectively acquired by the internal ADC channel.

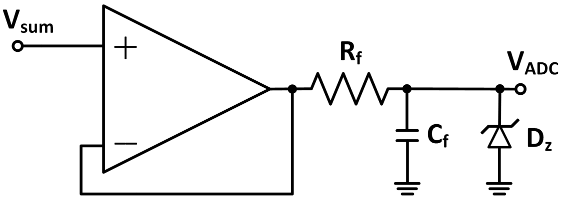

Figure 5.8: Low-pass filter for ADC input.

### 5.2.6 Control Board - Protection and Error Processing

Apart from the signal conditioning the control board also to includes hardware protections, through the processing of error signals. In order to provide protection to the system, the operation of all converters must be suspended if overvoltages and/or overcurrents in any of the magnitudes measured by the sensors are verified. This protection mechanism must be ensured by both software and hardware, thus maximizing risk/damage prevention. Besides, the system should be capable of resuming operation only after user intervention, avoiding undue triggering. The error detection mechanism used consists of a comparative window with two comparators. The operation of this circuit allows a high logical value to be established at the respective output when the input voltage is within the established window and a low logical value if this is not the case. The upper (Upper Trip Point - UTP) and lower (Lower Trip Point - LTP) limits are established by determining the voltages dividers at the positive and negative input terminals of the respective comparators. Figure 5.9 shows the schematic of the window comparator.

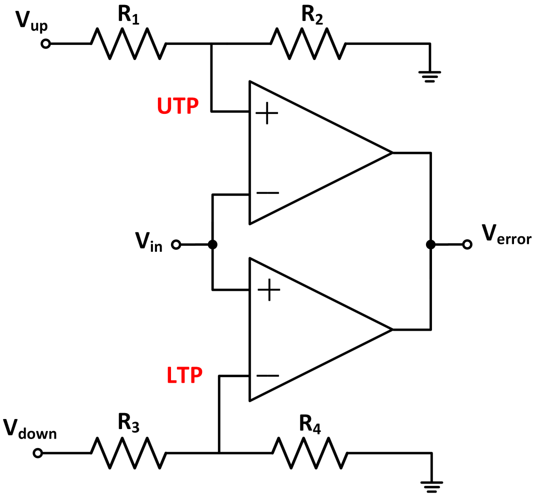

Figure 5.9: Window Comparator utilized for error detection.

For every sensor there is a window circuit, in which they share a single output, functioning as a kind of logical AND. Considering this, the short circuit established between the comparator outputs is only possible if they are an open collector. Therefore, it is used the integrated circuit LM339 from Texas Instruments, containing four comparators [70]. Also, is important to note that this circuit output needs a pull-up resistor to establish a high logical value. The input ($V_{in}$) of the window comparator is the midpoint of the voltage divider formed by the measuring resistors (Figure 5.6). As such, it is necessary to determine the voltage at the said point from which an over-voltage at the sensor input is considered.

Considering excessive voltages for the grid voltage absolute values higher than ±345 V, the resulting voltage drop in the measuring resistor for the limit value is ±1.054 V, thus establishing UTP and LTP. Opting for $V_{up}$ = +15 V and $V_{down}$ = -15 V and assuming LTP = -UTP, it is determined that has R1 ≈ 13.2 R2 with $R_1$ = $R_3$ and $R_2$ = $R_4$. Therefore, $R_1$ = 120 k$\Omega$ and $R_2$ = 9.1 k$\Omega$ are used. With this an error is detected when one of the voltages measured by the respective sensor exceeds approximately 345.6 V in absolute value. For the DC voltage sensors, considering they are not subject to negative voltages, it is established for both sensors a LTP of -0.15 V, leaving a small margin to tolerate noise and sensor deviation. Therefore, it is opted for $R_3$ = 200 k$\Omega$ and $R_4$ = 2 k$\Omega$. For DC-link overvoltages, since the capacitors used support a maximum voltage of 450 V and the ripple is at most 20 V, it is established a UTP of 433 V by opting for $R_1$ = 44.2 k$\Omega$ and $R_2$ = 10 k$\Omega$. For the battery, is defined a maximum voltage of 105 V, therefore is opted for $R_1$ = 56 k$\Omega$ and $R_2$ = 15 k$\Omega$. Regarding current sensors, for the LTS 25-NP sensor it can measure a maximum of 20 A DC current, and since the converter is unidirectional the minimum current is 0 A, therefore for a LTP of -0.15 V $R_3$ = 200 k$\Omega$ and $R_4$ = 2 k$\Omega$ and $R_1$ = 63 k$\Omega$ and $R_2$ = 12 k$\Omega$. For the battery current, the LA-100-P sensor can measure a maximum 33 A. With this, is used $R_1$ = 56 k$\Omega$ and $R_2$ = 16 k$\Omega$. Lastly, concerning the motor current sensor, it can measure up to 200 A, where the limits are symmetric, therefore $R_1$ = $R_4$ = 16 k$\Omega$ and $R_2$ = $R_3$ = 3.9 k$\Omega$.

With the procedures carried out, it becomes possible to detect over-voltages and over-current to stop the operation of power converters. Since the comparator outputs will return to a high logical level as soon as the anomaly verified is extinguished, the system may not be prepared to reinitialize. Therefore, it is necessary to add memory to the analog system to save the error signal and prevent an automatic restart. To implement memory to the error processing is opted for the integrated circuit LM555. The LM555 is produced by Texas Instruments and it has a wide range of applications such as delay generation, triangular and saw-tooth waves, PWM signals, as well as a frequency divider or a mono-stable switch [71]. In addition, this integrated circuit can operate as a memory cell. Thus, it is possible to receive the error signal and change the logical level at its output, keeping it unchanged regardless of whether the error signal changes. This component can also restore the respective precious state by application a reset signal. In this way, by operating on a set and reset event basis, the user can restart the system at will. Figure 5.10 situates the LM555 in the context of error processing.

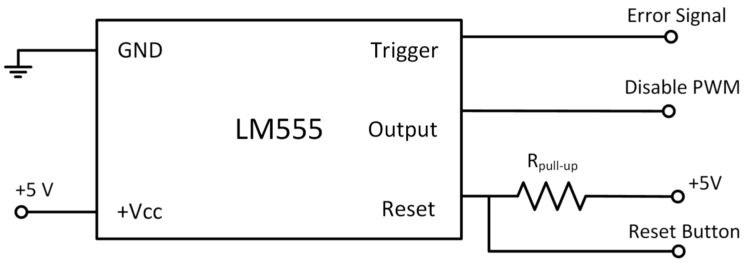

Figure 5.10: LM555 error processing.

That being said, in addition to being sent to the DSP via an optocoupler, the memorized error signal passes through a combination circuit to enable or disable the converter semiconductors. The logic circuit is greatly simplified because the implemented drivers have an enabling input, as will be discussed in the next section. Since the driver's disable input is active at the logical level high, the combinational circuit is an OR port where the inputs are the output of the LM555 and a switching signal from a switch available to the user. The output is then connected to the disable input of each driver.

### 5.2.7 Driver circuits for the Charger Converter

The boundary between the control part and the power floor is established by the power semiconductor driver. Although a MOSFET or IGBT is a voltage-controlled device, it is required to enable/disable the gate terminal to operate the semiconductor. Considering that an IGBT operates like a switch, it is necessary that the voltage applied to the gate concerning the source/emitter of the upper semiconductor be maintained at appropriate values.

Given the requirements presented, to drive the power semiconductors is necessary to use an appropriate driver circuit. As such, it is used a driver from the manufacturer Analog Devices with the reference ADUM3123. This driver is designed for a single IGBT and it guarantees galvanic isolation between input and output up to 3 kV. The ADUM3123 can be supplied with 3.3 V or 5 V on the primary side and 4.5 V to 18 V on the secondary. On top of that, it supports a maximum peak current of $4$ A at the output and allows a switching frequency up to 1 MHz [72]. Physically, the ADUM3123 encapsulation is SMD (Surface Mounted Device), contributing to a more compact PCB. As mentioned in the previous section, this driver has a disable input, disabling commutations and keeping the outputs at a low level when this signal acquires a high logical level, regardless of the gate signals sent to the driver. On the input terminal of the ADUM3123 is applied the PWM signal with a specific duty-cycle provided by the DSP GPIO.

For the supply of the driver output is necessary to use an external DC power supply, so it is opted for the TMA1515S isolated DC-DC converters [73]. The output of the TMA1515 is the same as the input but it is isolated from the primary side and consequently from the control system. The reason for the voltage shift of 5 V to 15 V is that the IGBT gate acts similarly to a capacitance with a voltage threshold of 5.5. With a higher voltage PWM, the capacitance reaches this threshold faster providing a faster IGBT response. The ADUM3123 driver circuit implementation is illustrated in Figure 5.11.

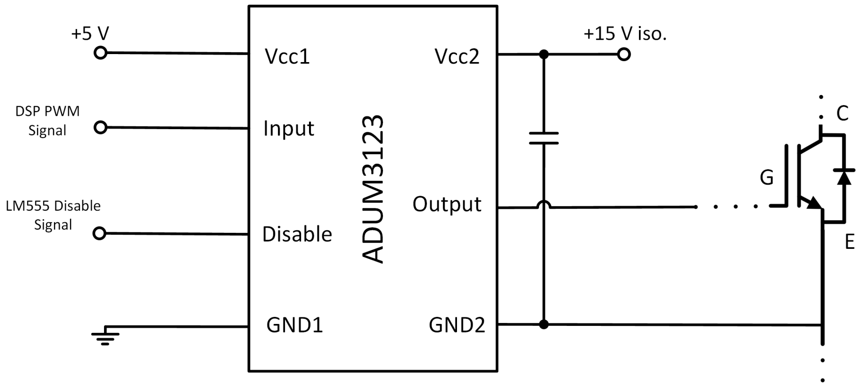

Figure 5.11: ADUM3123 and driver configuration.

As alluded before, for the DC-DC buck/boost cascade converter is necessary two IGBTs, therefore it is replicated the driver circuit for both semiconductors. The two driver circuits are present on the control board that acts as an interface between the DSP and the IGBT. The connection with the DSP is made by a DB9 connector with +5 V and GND supply and the respective buck and boost PWM signals.

The developed control board, is illustrated in Figure 5.12 along side with the description of the respective sub-circuits, that were detailed in the previous sections.

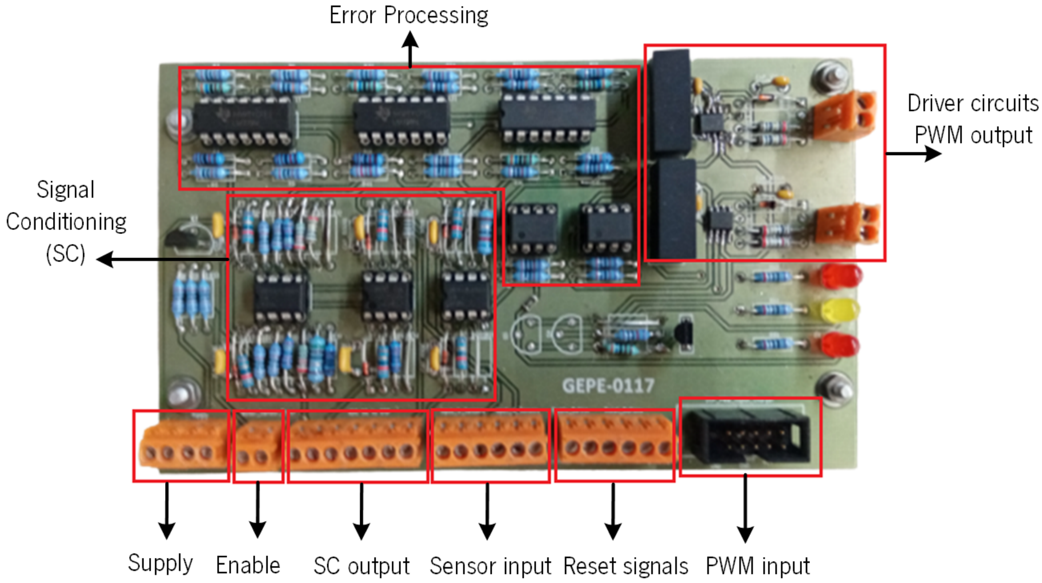

Figure 5.12: Control board developed and the respective sub-circuits.

### 5.2.8 Driver modules for the Motor Full-Bridge Converter

The motor converter semiconductors are required to sustain a rated current of 200 A, therefore it is necessary to use specific IGBTs that can fulfill this requisite. With this in mind, it is opted to use High Power IGBT Modules and consequently are used driver modules more appropriate for these conditions than the ADUM3123. The driver used for the motor converter is the SEMIKRON SKH22AH4, which is a hybrid dual IGBT driver with a maximum switching frequency of 50 kHz, turn on gate output of 15 V [74]. This driver offers protection against short circuits and galvanic isolation through the pulse transformers it has internally, preventing problems arising in the power system from spreading to the control system. Another feature of the SKHI22A R driver is that it allows the detection of anomalies in the driver itself, as well as the detection of overcurrents in the IGBTs modules [74]. Relative to the driver circuits, for the semiconductors referred, GEPE researchers developed the command board GEPE-0015 and the driver board GEPE-0025, used for similar systems. These boards were previously tested and validated for the necessities presented above. With this, it is opted to implement this solution, however, in theory it can be used ADUM drivers. The command board GEPE-0015 serves as an interface between the DSP and the motor driver boards and also receives error signals from the control board that debilitate the motor converter. Despite also having error processing, the purpose of GEPE-0015 is to process the PWM signals from the DSP and send them to the driver boards. The interface made between the DSP and the driver boards is made by shifting the PWM voltage from 3 V to 15 V, for the same reasons as mentioned on the driver circuit above. The GEPE-0015 board is supplied with 15 V, GND and the error processing is similar to what is described for the control board, i.e it has an open coletor for error output and a reset button [75]. In Figure 5.13 is possible to observe that command board has two driver outputs, A and B, that can operate one IGBT leg, respectively. This characteristic simplifies the control of the motor converter since it is composed by two IGBT legs. The driver boards GEPE-0025, are composed by the SEMIKRON driver SKHI22AH4 (R) and two connectors to make interface with the GEPE-0015 board and the IGBT modules. The implementation of this driver similar to recommended by the datasheet, where the only difference is the DB9 connector to GEPE-0015 board [76]. Each driver can activate two IGBTs, therefore it is needed a total of two GEPE-0025 boards. With this, one is connected to the output A and other to output B of the command board GEPE-0015.

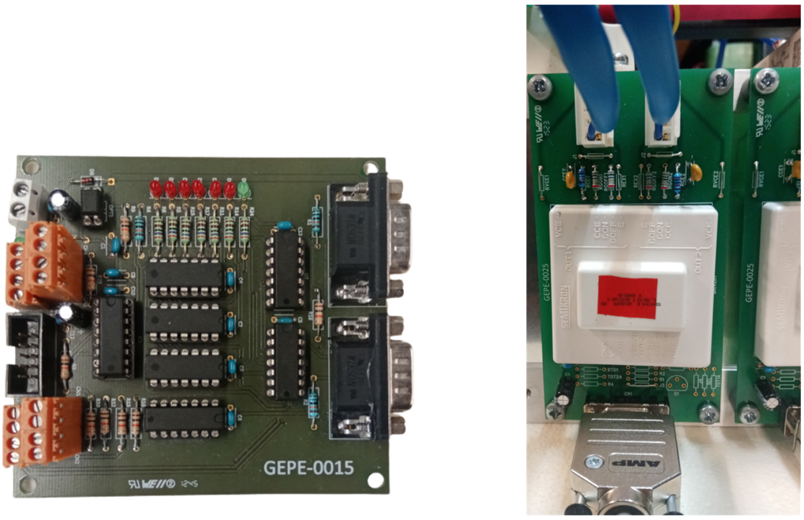

(a) (b)

Figure 5.13: Command and driver boards utilized for the motor control system: (a) GEPE-0015 command board; (b) GEPE-0025 main driver board with the integrated SKH122AH4 driver.

Between each driver and the respective IGBT modules there is a small PCV (developed by GEPE), GEPE-0016, which it is shown in Figure 5.14, which ensures that the voltage between the gate and emitter of each IGBT does not exceed the maximum value recommended by the manufacturer.

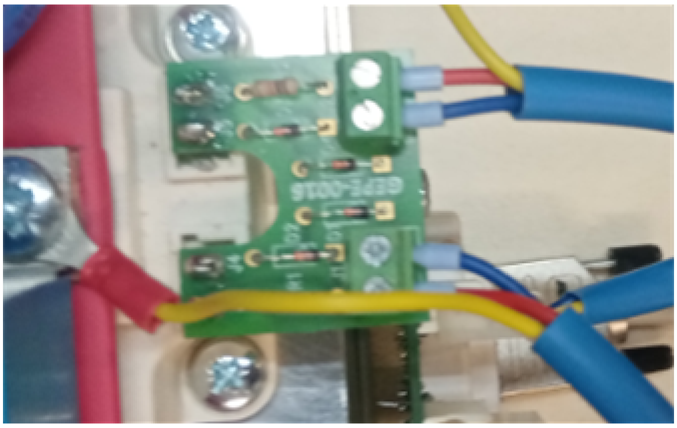

Figure 5.14: Picture of the GEPE-0016 PCB.

### 5.2.9 DAC - Digital to Analog Board

For the validation of control theories and to verify the correct operation of the converters, it is essential to provide real-time monitoring of the DSP's internal variables. Thus, it is used the PCB shown in Figure 5.15, consisting of a Digital to Analog Converter (DAC). As characteristics, this DAC is the model TLV5610 from Texas Instruments, which allows the simultaneous display of 8 channels with a maximum resolution of 12-bits [77]. At the output, the DAC has a voltage ranging from 0 V to 2.5 V, therefore to improve the readability, GEPE researchers implemented a signal conditioning circuit on the PCB to obtain bipolar values between -5 V and +5 V at the output.

The communication with the DSP is based on the SPI protocol (Serial Peripheral Interface) through a DB9 plug, which also provides a DC supply. On the other hand, BNC cables are used to communicate with an oscilloscope to monitor the DSP internal variables.

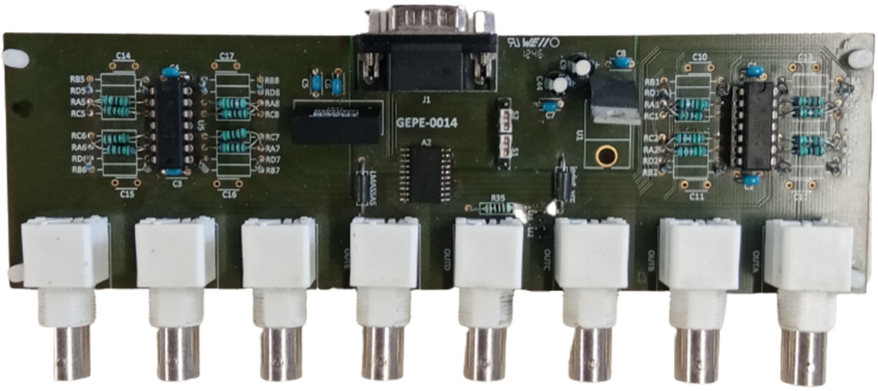

Figure 5.15: Picture of the DAC board used.

## 5.3 Power System Development

This section presents the power circuits of the developed system, namely the AC-DC converter, and the full-bridge DC-DC converter for the charger and motor modules, respectively. Therefore, the components of the developed converters are described, as well as the assembly and disposition of the hardware. The passive elements necessary for the correct operation of the converters are also presented, such as the DC-link capacitors and inductors.

### 5.3.1 Charger Converter Prototype

Starting from the grid side, it is used a VARIAC (Variable AC Power Supply Transformer), that allows regulation and control over the AC voltage. This is necessary for testing with lower voltages, to adjust the controls and other system variables before testing with the power grid nominal voltage. On top of that, it is used a 1:1 transformer between the power grid and the VARIAC to provide a layer of insulation. Finally is introduced a bypass switch for the reason mentioned on the simulation chapter, and also protects the VARIAC during operation start from current peaks. Thereafter, it is plugged the VARIAC supply to the PCB i.e. the DFB converter. The diode bridge is composed by the semiconductor STTH3012W, a fast recovery diode produced by STMicroelectronics [78]. The STTH3012W diode can support a maximum cathode-anode of 1200 V, currents up to 30 A and a maximum temperature of 175 °C. On top of that, the semiconductor has a recovery time of 47 s. Considering that the buck and boost diodes are also STTH3012W with switching frequency of 50 kHz the semiconductor recovery time is an important aspect. In addition, these diodes are also justified by the necessity of sustaining voltages up to approximately 420 V and maximum currents of 30 A.

The controllable semiconductors used are two FGA25N120ANTD IGBTs. These semiconductors have maximum collector-emitter voltage of 1200 V and supports a maximum collector current of 50 A at 25 °C. In relation to the gate capacity, the value indicated in the datasheet is 3700 pF when tested with a 1 MHz signal, which is quite low considering the power levels in which the IGBT operates. Typical switching times for this device are below 200 ns. Also the anti-parallel diode built into the IGBT is considerably fast, with usual reverse recovery times of decades of nanoseconds. Physically it features a TO-247 encapsulation, allowing a power dissipation of 312 W at 25 °C [79].

To be able to consume energy into the power grid, the DC-link must be able to store a considerable amount of energy. In addition, the DC-link voltage ripple must not be exceedingly high to not affect the correct operation of the converter. As such, for the DC-link are used four 450V/540uF electrolytic capacitors from the manufacturer Vishay BC. The capacitors are located on the PCB converter as opposed to being on a separate board, which is commonly seen.

The inductance value of the inductors used on the AC-DC converter has a direct influence on the current filtering, so the higher it is the lower the current ripple obtained. However, as the switching frequency is relatively high, the inductance value required to obtain a current of relative quality is not very high. Considering this, it is resorted to the simulations implemented to determine an appropriate value. That being said, according to the simulation chapter, it is used an inductance value around 500 mH.

In switching applications, both diodes and IGBTs temperature rises proportionally to current. Therefore temperature dissipation and cooling are essential in power applications, specifically for semiconductors. With this in mind, it is used a heatsink with dimensions 20x9.5x4 cm, where the semiconductors are inserted. Figure 5.16 shows the charger power PCB implemented with all the hardware, the heatsink with the semiconductors fixed (bottom of the figure), and the connection to the power grid using a generic plug.

### 5.3.2 Motor Converter Prototype

As mentioned the BDC motor used in this thesis is the ME1003 from Motenergy. It is a PMDC motor with a nominal power of 12.6 kW-16 kW for a 72 V and 96 V voltage supply, respectively. To measure

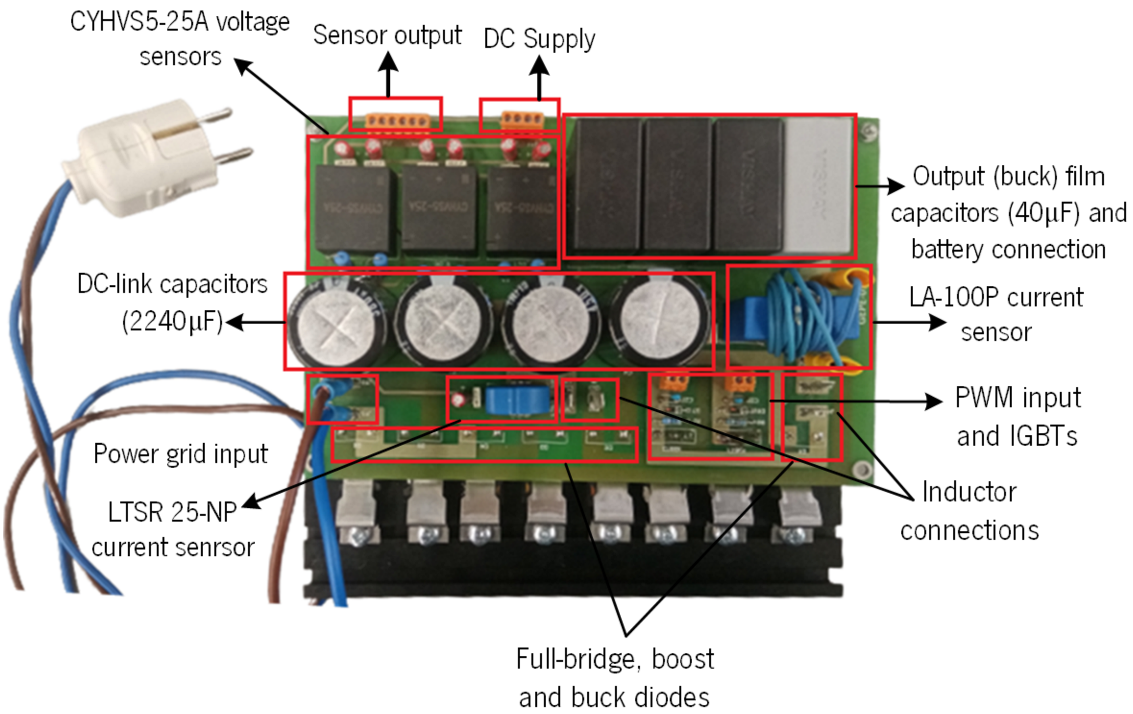

Figure 5.16: Picture of the charger power board were are detailed the respective components.

accurately the motor speed it is required that the magnet coupled on the rotor is close enough to the speed sensor, <2 mm. Therefore are made adaptations to the motor in order to fixate the sensor. Figure 5.17 demonstrates the motor used and a metal sheet adaptation to insert the sensor.

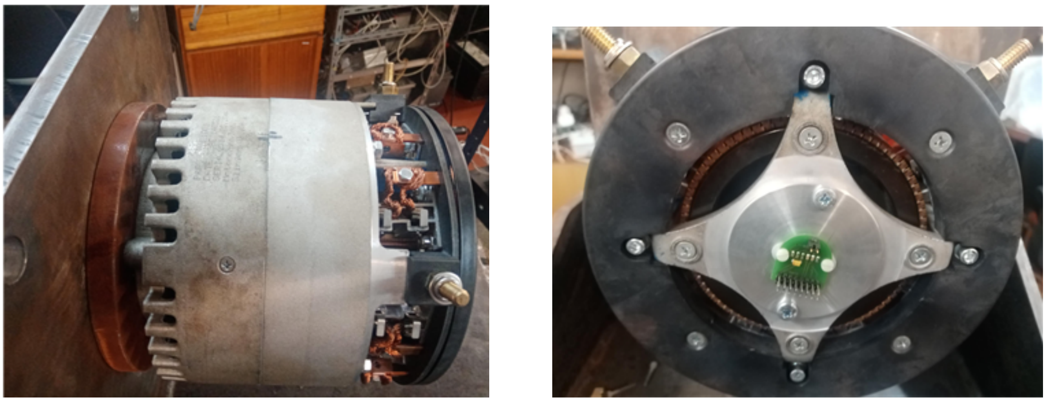

(a) (b)

Figure 5.17: Picture of the ME1003 motor: (a) side view of the motor; (b) bottom of the ME1003, where the speed sensor is attached.

For the motor full-bridge converter, due to the power involved, it is not possible to implement this circuit on a PCB. For this reason, it is developed a prototype for the converter, constituted by the IGBTs, and the respective driver circuits coupled to a heatsink. For this type of applications is used a 12x12x30 cm heat-sink, in which can be placed a cooling fan to improve heat dissipation. The two driver circuits are fixed on the lateral and the IGBT modules on the top, along with passive components, that are connected with 2 bars of cooper. The modules used for the motor converter are semikron's SKM400GB066D. These modules are especially recommended for typical applications in uninterruptible power supplies [80]. Each of these modules consists of two IGBTs with their respective anti-parallel diodes, which have a maximum voltage between collector and emitter of 1200 V, which can be covered by a maximum current of 612 A [80]. In addition, this module has, among other important features, a rise time of 60 ns and a fall time of 65 ns. Figure 5.18 illustrate the encapsulation of the SKM400GB066D IGBT utilized.

(a) (b)

Figure 5.18: Pictures of the SKM400GB066D IGBT module: (a) Side view, showing the IGBT leg layout; (b) Top view of the IGBT.

With this, it is proceeded to assemble the H-bridge converter prototype, where the heat-sink is used as the structure frame, with the IGBT modules fixed on the top and the GEPE-0025 drivers at the front. On top of that, it is used cooper bars for the connections between the hardware, and a capacitor bank to prevent voltage spikes and overvoltages. Figure 5.19 shows the full-bridge motor converter prototype, where can be seen the driver modules (front), as well as the IGBT modules attached to the heatsink (top) with the capacitors on top.

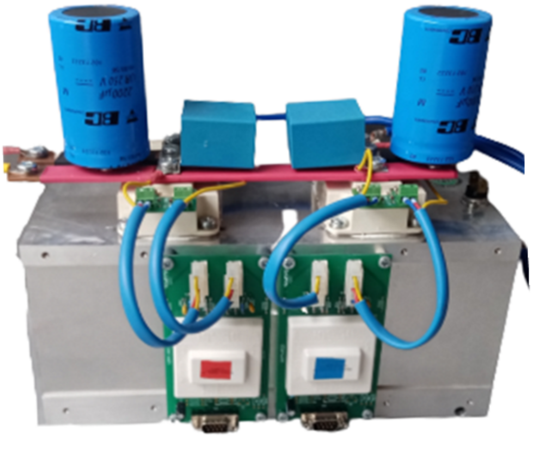

Figure 5.19: Picture of the developed motor converter prototype.

To better describe the implementation and assembly of the hardware, particularly for the motor testing, it is shown in Figure 5.20 the motor control system and all the connections between PCBs.

Furthermore, for the motor experiments it is utilized a workbench appropriate for practical tests. The work bench allows the docking of the motor to a brake which can simulate a mechanical load set by the user through a regulator and can be monitored in a display. Figure 5.21 presents the workbench, in which the ME1003 motor is connected.

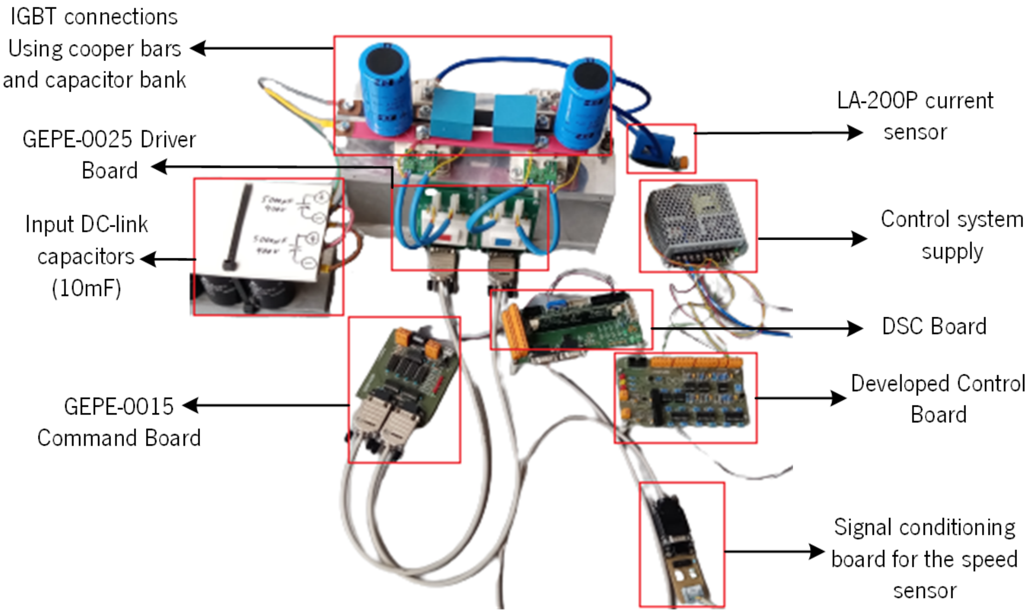

Figure 5.20: Traction system assembly and respective connections between PCBs.

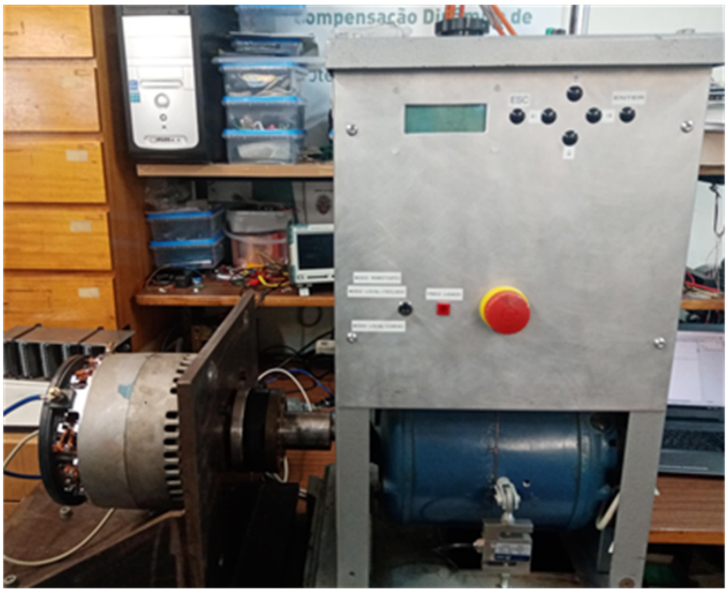

Figure 5.21: Motor workbench utilized for the experimental tests.

## 5.4 Chapter Conclusion

This chapter described the implementation of proposed systems hardware, the development of PCBs for signal conditioning and error processing, as well as the calculation of the parameters of components. Initially, it was described the control system, and presented the DSP that makes all the digital control calculations to operate the power converters, as well as the sensors to measure electric quantities. It was also described how these electric quantities, such as current and voltage, were translated to digital values readable by the DSP ADC module and consequently the signal conditioning required for this process. On top of that, it was described the error processing when occurs an over/sub-voltage or current anomaly to avoid hardware damage. On the other hand, the driver circuits and modules used to isolate the control system from the power system and to appropriately activate the IGBT's gates were presented. Most of the hardware was implemented from scratch, except for the four PCBs developed previously by GEPE researchers, the GEPE-0015, GEPE-0025, GEPE-0016, and the conditioning signal PCB for the speed sensor. It is important to note that the hardware re-utilized was previously tested and validated. After covering the control systems, it was presented the power systems, where it is explained the implementation of the charger power board, as well as the motor converter prototype. For the power systems, it was described the choice of the semiconductors used as well as capacitors and other passive components. For the battery charger system, it was explained the used of a transformer and a VARIAC between the converter and the voltage supply, to apply another layer of isolation as well as to regulate the power grid voltage to lower values, respectively. On top of that, it was presented the motor model used, the ME1003, and how it is installed on the workbench to apply a mechanical load.

# Chapter 6

# Experimental Tests and Results

## 6.1 Introduction

This chapter presents the analysis of the experimental results obtained for the developed traction and charger systems. As such, the results are analyzed in a progressive format, where are tested the blocks necessary for the operation of the systems, such as the mechanism for synchronization with the power grid, the current and voltage control techniques, among others. With this, the experimental results are presented according to the sequence in which they were obtained. As a safety measure and to ensure the integrity of the developed of the hardware, the voltage and current values used in the tests was gradually increased until reasonable values were reached, thus making it possible to obtain results involving significant power levels, even though they are substantially below the nominal values.

## 6.2 Motor Operation Results

The simulation results for the traction system were obtained using the setup presented in chapter 5 (Figure 5.20), where is used a motor workbench. The motor reference current is set by a potentiometer, that simulates an acceleration/braking hand accelerator. The first step was supplying the motor directly with low voltage to see the current waveforms, and how the motor operates. Next, it was measured the PWM signals at the IGBT gates and validated the correct functioning of the driver modules (Figure 6.1). Before fully operating the motor, it was determined empirically the PI control gains of the torque control. Therefore, various results were obtained but are only shown the conclusive ones, where the system can be validated. With this in mind, it is shown in Figure 6.1 the PWM signals for the mode 1 and the respective waveforms of the motor's current and voltage waveforms, during open loop control and a constant duty-cycle. In this mode of operation, it is applied to the IGBT S1 the PWM signal with varying duty-cycle (PWM$_a$) and to the IGBT S4 a 90 % duty-cycle PWM that corresponds as ON (PWM$_b$) (Table 3.1). As expected, the PWM signals have a frequency of 10 kHz and an amplitude of 23 V (-7 V to 16 V) and a fairly good rise-up time. On the other hand, due to the motor's low inductance (93 $\mu$H at 120 Hz), the respective current ($i_{motor}$) has high variation. Consequently, later on, it was necessary to add a sliding window average to reduce the impact on the control. This has an impact on the control by increasing the time constant, or reaction time. However, in the context of a motor operation, the time scale is great enough for this to have major significance. By observing Figure 6.1 it is possible to see that while both IGBTs are OFF, the motor starts coasting. Despite, having no current supply during this phase, the motor produces a back-EMF voltage, which can be seen effects on the motor voltage ($V_{motor}$).

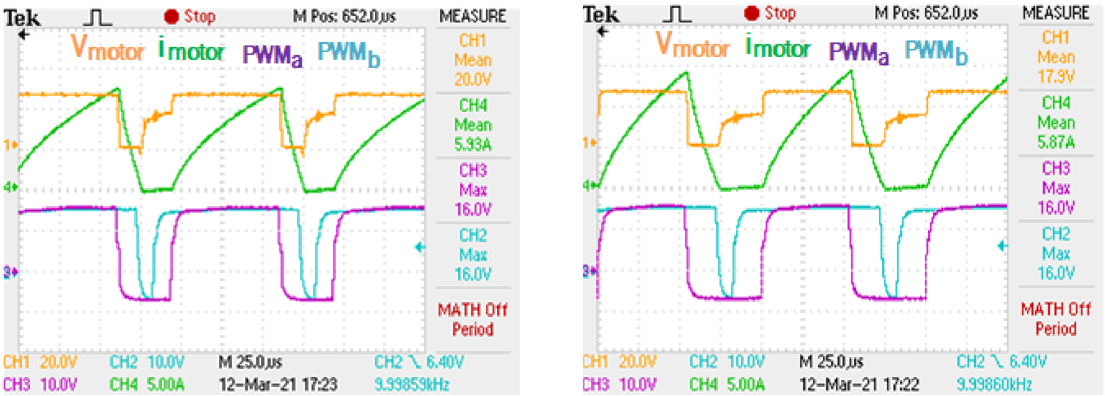

(a) (b)

Figure 6.1: Typical current (CH4: 5 A/div) and voltage (CH1: 20 V/div) waveforms of the ME1003 motor, during acceleration mode, and the respective PWM signals (CH2,CH3: 10 V/div), for driver validation. Time scale of 25 $\mu$s.

The motor speed, as well as the modes of operation, were obtained via DAC. On top of that, on the simulation results shown, is measured the back-EMF voltage instead of rotation speed, since it is easier to monitor and speed can be easily obtained by applying the $K_v$ constant ($K_v$ = 0.207 V/rpm). Another solution to measure the rotation speed is using a tachometer. A tachometer is specially used to measure the speed of rotating objects, where it is attached a part of the device that measures the number of rotations internally. The tachometer also has a light emitter that can be measured by pointing it to the rotating shaft. For the conducted tests it was used a constant DC power supply of 31 V (43 % of the rated value), instead of a battery, therefore the validation of the regenerative braking was conditioned. However, due to the high capacitors on the DC-link input, making up to 10 mF capacitance, it was possible during mode 2 to return energy to these capacitors. This phenomenon was monitored by observing motor's current direction, which it was negative, or rather, from the motor to the power supply. To monitor the motor behavior it was necessary to use a greater oscilloscope time scale than what it was set for the charger tests. The current range used on the tests shown is from -5 A to 15 A, which without a mechanical load the acceleration is already very significant. On top of that tests with a 2 Nm mechanical load were conducted, where the only noticeable differences it was a higher current threshold for the motor to generate enough torque to rotate, an applying a mechanical load while during operation reduces the motor speed. With this, it was concluded that effective torque, is the difference between motor torque and mechanical torque. Another important aspect of the experimental tests conducted was the difficulty in capturing conclusive results. On top of that, in the tests conducted, real-time observation of the motor behavior was a greater validation factor.

Considering the test description above, the motor results are presented in Figure 6.2, showing the back-EMF voltage ($V_{emf}$), the operation mode, the motor current ($i_{motor}$) and the respective reference ($i_{ref}$). By observing the waveforms of Figure 6.2 it is possible to compare the motor current value with the reference and conclude that the control is functioning properly and it has a good reaction time. On top of that can also be established the relation between current/torque and the speed evolution. In some tests, it was reached speeds up to 642 RPM, as shown in Figure 6.3. However, to notice variations in the oscilloscope time scale, it was only reached a rotation speed of 150 RPM. As referred before, during these tests the regenerative braking validation comes from observing the motor current sign. With this, it is assumed that when the current is negative it flows to the battery or, in this case, to the capacitor bank.

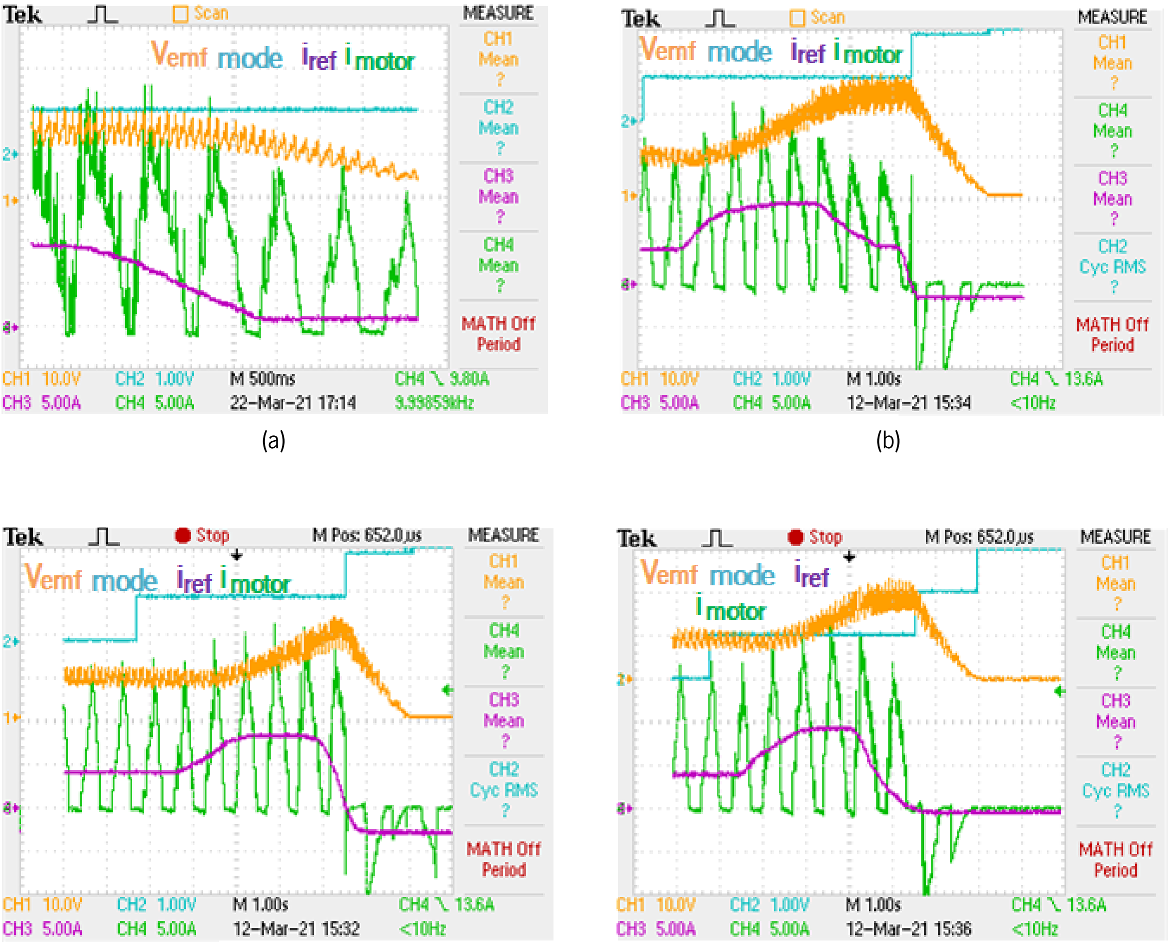

(a) (b)

(c) (d)

Figure 6.2: Waveform results of motor operation showing the waveforms/curves of the back-EMF voltage (CH1: 10 V/div), mode (CH2: modes 0 to 4 (0 no control) as per established before (1 mode/div)), reference current (CH3: 5 A/div), and motor current (CH4: 5 A/div): (a) Deceleration test while in mode 1; (b) and (c) Acceleration test followed by regenerative braking; (d) Test of modes 1, 2, 3. Time scale of 1 s/div.

Figure 6.3: Tachometer measuring the rotation speed of the motor axle using the light emitter mode.

## 6.3 Charger Operation Results

For the charging system, the experimental results were obtained in a similar order to the computer simulations. With this, it is started with PLL and PFC boost validation and lastly the charger control results are presented.

### 6.3.1 Synchronization with the Power Grid

The first step to test the charger converter, it was the validation of the PLL signal generated. For this, it was required a voltage sensor, and by means of a VARIAC it could be applied different voltage values and also test the amplitude synchronization. To visualize the PLL signal was used an external DAC, that was connected to the oscilloscope. From the oscilloscope, it was possible to monitor the PLL signal in comparison to the power grid voltage (monitored directly from the power supply), and gradually adjust the PLL algorithm gains to refine the obtained signal. The result obtained is shown in Figure 6.4, where it is present the moment the algorithm is activated. With this, it could be concluded that the synchronization takes one power grid period. Is worth noting that for this test is used a peak voltage of 60 V. The frequency of the PLL signal is also shown on the bottom right corner of Figure 6.4, which assumes a value of 50 Hz.

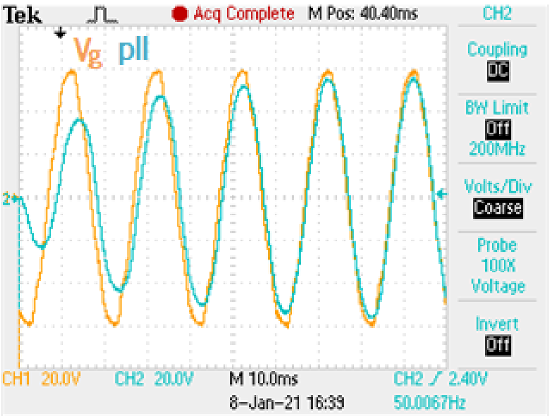

Figure 6.4: PLL Synchronization (CH2: 20 V/div) with the power grid voltage (CH1: 20 V/div).

To further validate the obtained PLL signal, it was also monitored the $\omega$t value calculated by the algorithm, in a steady-state regime, which it is present in Figure 6.5. A correctly calculated $\omega$t, must oscillate between 0 and $2\pi$ at a frequency of 50 Hz. It should be noted that the DAC output is 200 mV/div which can be translated to $\pi$/div.

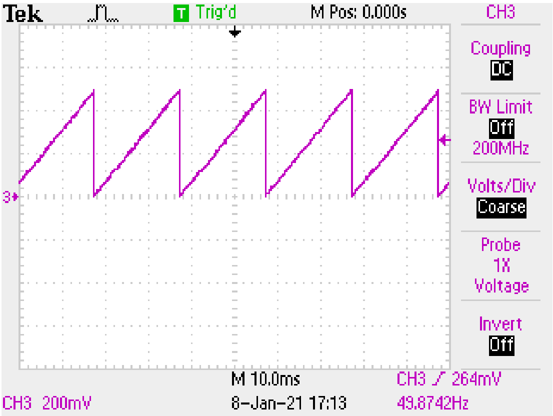

Figure 6.5: Frequency component of the PLL signal, $\omega$t, during steady-state regime (CH3: 2 mV/div, corresponding to 2 $\pi$/div).

### 6.3.2 Power Factor Correction and DC-Link Regulation

In this section is presented the experimental results of the AC-DC boost converter where it is validated the DC-link voltage regulation and the harmonics compensation. With this, Figure 6.6 shows as an example of the waveform the current prior to the start of the PFC current control, as well as the pre-charge DC-link voltage and the power grid voltage for comparison.

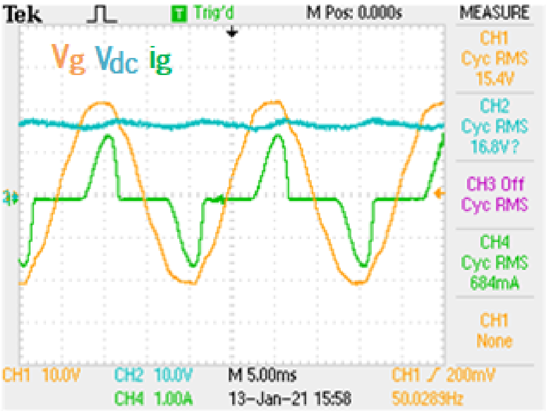

Figure 6.6: Synthesized current without the current control (CH4: 1.00 A/div), pre-charge DC-link voltage (CH2: 10 V/div) and power grid voltage (CH1: 10 V/div). Time scale of 5 ms/div.

To test the current control it was set a power grid voltage of 24 V RMS and a DC-link reference voltage of 40 V (10 % of the nominal value). Considering, it is not possible to isolate the DC-link from the buck converter, it is closed (allows current flux) the respective IGBT (PWM 100%) and placed on the output of the charger prototype a resistive load. This allows to test the AC-DC converter independently from the charging buck converter. The value of the resistive load, impacts the magnitude of the synthesized current, with this in mind it was opted to use a resistor of 26 $\Omega$.

To evaluate the PFC behavior it was measured reference current ($i_{ref}$) and the DC-link voltage ($V_{dc}$) with the DAC, as well as both power grid voltage and current ($V_g$, and $i_g$ ), and the current on the DC-side ($i_{dc}$) directly by the sensors. By measuring these quantities it is expected to obtain results similar to the waveforms obtained on the simulation. With this in mind, in Figure 6.7 the current and voltage waveforms are presented, in which it is possible to verify that the DC-link voltage value is what was expected, presenting a ripple of 2 V (5%). On top of that, it is validated the current control considering that synthesized current, after some control refinement, it has a THD$_f$ of 5.26%, as shown in Figure 6.7 (c).

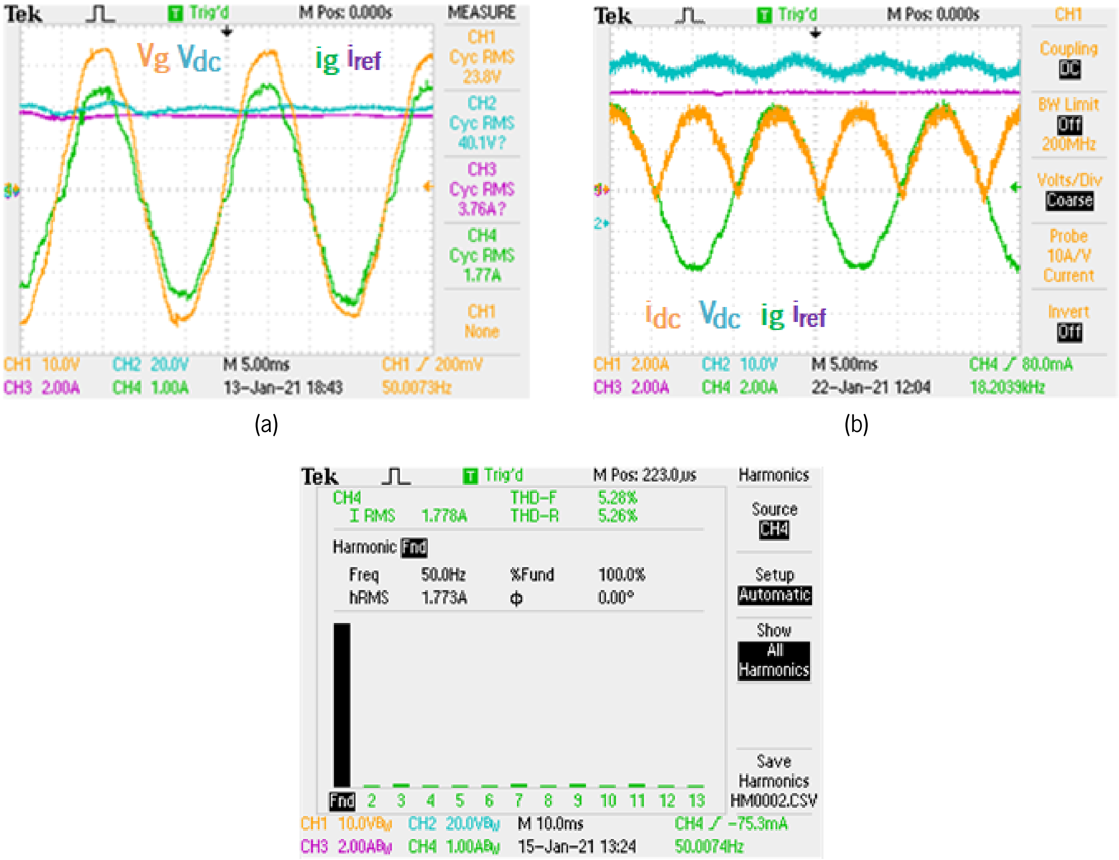

(a) (b)

(c)

Figure 6.7: PFC waveform results showing the absorbed power grid current (CH4: 1 A/div), reference current, (CH3: 2 A/div), DC-link voltage (CH2: 20 V/div) and : (a) Grid voltage (CH1: 10 V/div); (b) DC-side current (2 A/div): (c) Harmonic analysis of the absorbed current and the respective THD measurement. Time scale of 5 ms/div.

### 6.3.3 Buck Converter - Charger Control Operation

The next step to validate the charger system was the buck converter. With this, taking into account the stipulated values for the PFC tests is set a charging reference current of 1 A. On the other hand, for the conducted tests was used a resistive load instead of a battery, which it is not optimal for validating the charging control. However, it is still possible to confirm the correct implementation of the PI control. Therefore, it was used a resistive load of 13 Ω, and activated the PFC converter as presented above, resulting in the waveforms shown in Figure 6.8. Figure 6.8 shows the charger control in steady-state, where can be seen a constant load current of 1 A. On top of that, it is verified that the DC-link voltage remains stable during charging, and that both PFC and charger controls do not destabilize each other.

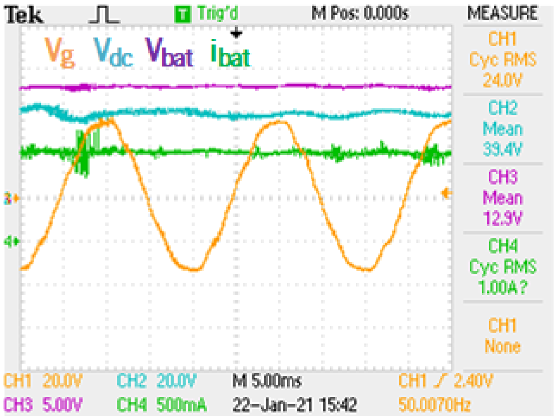

Figure 6.8: Buck converter waveform results showing power grid voltage (CH1: 20 V/div), DC-link voltage (CH2: 20 V/div), battery (load) voltage (CH3: 5 V/div) and battery current (CH4: 500 mA/div). Time scale of 5 ms/div.

To monitor the control behavior, it is shown in Figure 6.9 a transient-state, with an initially reference current of 0 A and then input a 2 A step. By comparing the battery current with the duty-cycle, it can be seen the control behavior, where initially there is an overshoot followed by an undershoot then gradually stabilizing around the reference. In this test, it was achieved a steady-state in 800 $\mu$s. It is also noted that the disturbance on the signals is due to switching noise (50 kHz), which could be eliminated with the use of a low-pass filter.

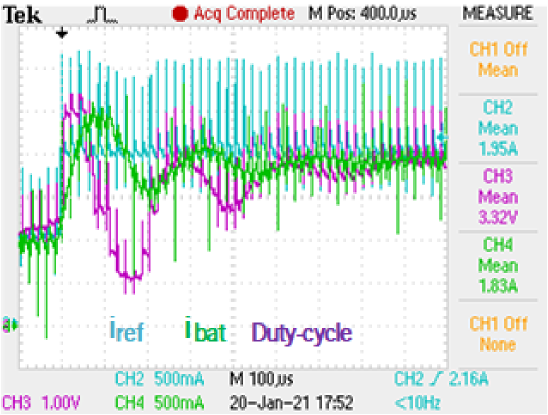

Figure 6.9: PI Control behavior waveforms: Reference current (CH2: 500 mA/div), battery current (CH4: 500 mA/div) and duty-cycle (CH3: Relative value). Time scale of 100 $\mu$s/div.

Figure 6.10 shows how the load current is affected by the IGBT PWM, causing a small ripple, due to the buck converter inductance. As alluded before the inductance value determines the current ripple. With this, it is possible to verify that during the period where the IGBT is ON the inductance charges energy, and during the OFF period it discharges. Similarly to Figure 6.9 the disturbance present in the reference current is due to switching noise impact on the oscilloscope and it is greater, with the increase of current/power.

One important aspect during the test of the charger module was the operation of the buck IGBT. Considering the used topology, if the IGBT is OFF, there is no current flux to the resistive load which causes a rapid voltage increase on the DC-link capacitors until they eventually blow up, causing serious damage.

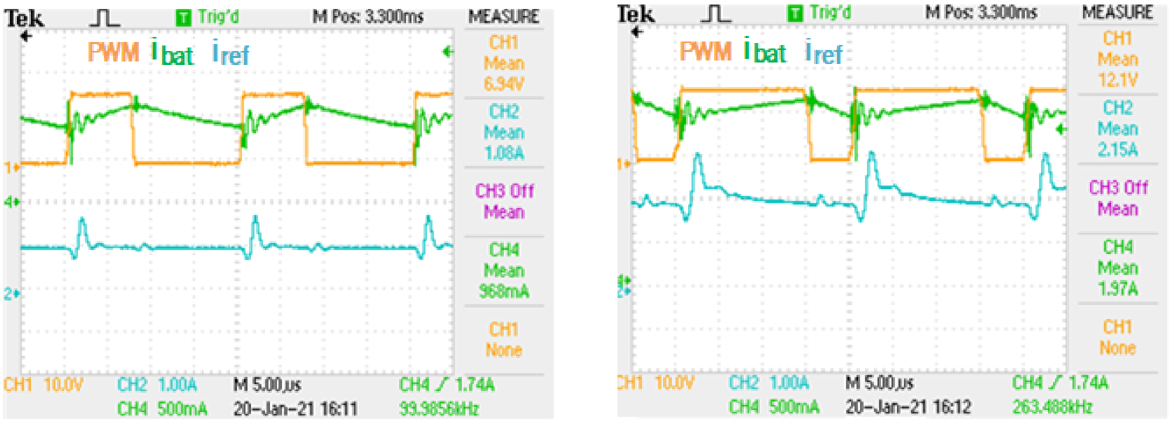

(a) (b)

Figure 6.10: PWM signal (CH1: 10 V/div) comparison with the Load current (CH4: 500 mA/div), and the reference current (CH2: 1 A/div): (a) Results with a 1 A reference; (b) Results with a 2 A reference. Time scale of 5 $\mu$s/div.

Therefore it was essential that the buck IGBT was monitored and never fully opened.

## 6.4 Chapter Conclusion

In the present chapter the results obtained during the experimental phase of the development of the charging and traction were presented and discussed.

Thus, firstly, the results of the charger operation were shown. Starting with the validation of the PLL algorithm, it was then presented the results of the current control and DC-link regulation detailing the current and voltage waveforms monitored in the oscilloscope. The results were obtained in power levels much lower than the rated (10%) ones which it is a shortcoming in terms of validation and future application, however it can be confirmed the correct implementation of the converters and control methods. On top of that, the power grid current absorbed still has a noticeable THD (5.26 %), that with improvements on the current control and further testing it would be able the remaining harmonic content. On top of that the usage of a resistive load instead of a battery limits the legitimacy of the experimentation.

Regarding the motor operation results, it was chronologically detail the procedures conducted, where firstly was tested the motor with a direct DC power supply to monitor its natural operation. Then, it was presented the waveform results of the PWM signals, validating the driver implementation, as well as the typical current and voltage waveforms for the ME1003 motor. Finally, it was detailed the set testing conditions for the torque control validation, and the respective waveform results obtained in the oscilloscope. For the experimental procedure, it was used a potentiometer that simulates a hand accelerator and stipulates the reference current. Thus, withing a time scale of a few seconds, it was input arbitrary references in order to test the operation in the different operation modes. Since it is used a fixed DC power supply instead of a battery, the validation of the regenerative braking was made by evaluating the current sign and considered that when the motor current is negative its flows in the direction of the supply.

# Chapter 7

# Conclusion

## 7.1 General Conclusions

In this thesis it was developed and presented a system prototype capable of operate the traction of DC motor and allow regenerative braking, as well as a controllable battery charging system that integrates Power Factor Correction (PFC) and harmonic compensation. For the traction system it was developed a Full IGBT bridge, or H-Bridge that allows the motor to operate the various modes. On the battery charging prototype it was implemented a two-stage system, where in the first stage was developed of an AC-DC converter that integrated a PFC current control, and regulated the DC-link voltage. Then on the second stage is composed by a DC-DC converter that provides a charging current control.

In chapter 1 were presented the energy challenges that society faces today, and proposed an electric motorcycle as a more sustainable solution when compared to the traditional internal combustion vehicles. It was presented the commonly used motors used in Electric Vehicles (EV) as well as the available market for different electric motor types. On top of that, it was detailed the controllers used to operate motor traction and respective functionalities and characteristics. Still in the topic of electric motors, it was introduced the concept of regenerative braking and the upsides this technique brings in terms of energy sustainability by returning energy to the batteries. Next, it was covered battery charging and energy quality solutions, where battery charging methods and applications were shown. In this context, it was also detailed energy problems such as harmonics and solutions to mitigate them. Then, it was proposed two system prototypes and the respective advantages/disadvantages. Lastly, it was presented the motivation to develop this thesis and the objectives initially proposed.

In chapters 2 and 3 was made a bibliographic research about the charger and motor topologies, respectively. Chapters 2 and 3 provided all the theoretical information necessary to implement the proposed traction and charger systems. With this in mind, both chapters were divided similarly where, firstly various converter topologies for each system were presented, in particular the full and half-bridge converters for the motor module. For the charger module it was detailed the diode full-bridge (DFB) and the active rectifier as the AC-DC PFC converters, and the buck converter for the battery charger. Secondly, control techniques for the converters proposed, as well as Pulse Width Modulation (PWM) techniques were then presented. For the AC-DC converter, in chapter 2, it was proposed the PI current control and predictive control with Sinusoidal Pulse Width Modulation (SPWM) technique. Regarding the battery charger, it was introduced the lithium battery and respective charging control methods, such as constant current-constant voltage (CC-CV), constant current-constant temperature (CC-CT), and simple constant current (CC). Concerning the traction system, in chapter 3, it was presented a torque control based on the converter system and a hysteresis current band control.

After presenting the different converter and control solutions, chapter 4 presented the computer simulations of the opted topologies on the PSIM software. With this, it was firstly presented the design of the simulation models, in particular of the BDC motor and the AC-DC converters and the respective parameters. Then, it was implemented the control system, where it was used a coding block to write the control code in C language. For the control system, it was required to measure variables from the power system by means of voltage and current sensors, which are the input of the coding block. The output of the coding block is a duty-cycle reference value that it is then applied to the PWM technique. the PWM technique implemented in simulation is based on the comparison between the duty-cycle reference and a triangular waveform, that results in a PWM signal. The PWM signal is then applied to the respective IGBT gate. With the control and the converter systems implemented in then preceded to evaluate the results and validate the topologies. The main purpose of these computer simulations is to achieve a system that it is close as possible to what it is going to be used in experimental tests, in order to reduce the risk of errors in more advanced stages. With this, the main concern was to refine the control system according to the waveform results obtained and monitor the changes to gradually improve the simulation. This feedback process was conducted until the simulation results matched the topologies theory.

Once the computer simulations were concluded, the next step was the implementation of the hardware. Therefore, in chapter 5 is detailed the design of the control and power systems development. Some of the hardware was previously developed and validated by GEPE researchers, then at the initial stage, it was made a schematic of the existing circuits. At the same time, it was made a hardware draft for the circuit Printed Circuit Boards (PCB) that were developed afterward. As it has gradually opted for the material components it was described the respective details of the hardware. The circuit PCBs developed were a control PCB, which integrated signal conditioning for the sensor's output to be readable by the DSP, error processing to detect and act on overcurrents/overvoltages, and the driver circuits for the two IGBTs of the charger power converters. The control PCB was integrated on both charger and traction systems, where, in the latter, it provides the signal conditioning for the motor current sensor. The main concern during the development of this circuit PCB was the definition of the component values, such as resistors, in order to obtain the expected result. With this, it was required circuit analysis skills to correctly assert the components. Besides the control PCB, it was also developed the power PCB for the charger system. This circuit PCB incorporates the converters, as well as the passive components, such as capacitor and inductors, but also the sensors. To develop this PCB was needed to take into consideration the power levels involved, which are higher than the ones in the control PCB. One of the challenges of developing PCBs was the organization and mapping of the components on the circuit in order to optimize space and connections. The circuit PCBs that were re-utilized were the command PCB GEPE-0015, which provides an interface between the DSP and driver PCBs. Connected to the GEPE-0015 are two driver PCBs GEPE-0025 that command one IGBT leg of the H-bridge, respectively. Another PCB that was utilized was a Digital-to-Analogic (DAC) PCB that enabled digital values processed in the DSP to be monitored on the oscilloscope in real-time. The fourth PCB that was previously developed and integrated into this thesis was a small signal conditioning PCB for the speed sensor. The final procedure of the traction and charger systems implementation was the welding of the developed circuit PCB's hardware and the assembly of the converter prototypes.

In chapter 6 was presented the results obtained during the experimental phase of the traction and charger systems development. Initially, it was validated the correct operation of the control system sub-circuits and made corrections to errors during the circuit PCB development. At the same time were made linearity testing to the voltage and current sensors in order read more accurate values. It is important to note that the third voltage sensor on the charger system, responsible for the measurement of the battery voltage was not applied for the charging control implemented (CC protocol). Although, this sensor is necessary in case a more advanced protocol such has CC-CV is implemented. After that, without powering the converters, it was tested the driver circuits and applied PWM signals to the power semiconductor's gates in order to validate the respective frequency and amplitude. It was then orderly obtained the experimental results of the charger system, starting with the AC-DC converter and the respective synchronization with the power grid, DC-link regulation and harmonics compensation, followed up by the current control validation of the buck converter. The validation of the charger system was conditioned by the used of a resistive load instead of a battery. This degrades the quality of results since is not possible to monitor the gradual battery charge. The main concern/difficulty during the charger system tests was to refine the PI control gains and reduce the Total Harmonic Distortion (THD) of the absorbed current. On top of that it was necessary to accommodate the regulation of the DC-link voltage to the activation of the charger buck converter, which caused a rising voltage step. It was also important to monitor the PWM signal of the buck IGBT since with it being open (no current flux) caused a rapid and indefinite rise of the voltage on the DC-link capacitors. With this in mind, it was necessary to strictly limit the PWM duty-cycle to avoid risk of damage. This rapid rising in voltage caused adversities which did not allow the testing of the charger system with higher power levels.

Subsequently, it was preceded to the traction system experimental tests, where initially it was supplied the DC motor, ME1003, in order to observe it's behavior, and obtain the characteristic voltage and current waveforms. Then, it was presented the experimental results, where it can be validated the motor modes of operation. With the waveform results presented it was possible to see the effect of the reference current on the acceleration. A problem that occurred during the control tests was the rapid acceleration and deceleration of the motor, caused by the great variation in current. This is caused due to the low motor inductance, which also translates to a particularly high rated current and low rated voltage. This situation was solved by implementing an average of the motor current values read by the sensor, which also slows down the control reaction. The main shortcoming of the traction system experimental tests was the use of a constant DC power supply, which did not allow a thorough validation of the regenerative braking, besides monitoring the current direction. On top of that, it was noticed a difficulty in obtaining conclusive results by simply monitoring the oscilloscope variables, such as motor current and speed, considering it was mostly resorted to observing the motor behavior in real-time. On top of that, it was only possible to verify braking, by virtue of the high capacitance on the converter input, which allowed some energy to be sent back to the capacitor bank and simulate battery operation. Other than that it was possible to validate the traction system by controlling the motor torque using a potentiometer that acted as a pedal.

The development of this thesis involved several areas of electronics and programming, that were essential during this project. Accordingly, for the elaboration of this type of work it was a needed good knowledge in circuit instrumentation, power electronics, analogue and digital electronics, microcontroller programming, knowledge of simulation tools, as well as PADS for the development of PCBs. No less important, it was need for knowledge of mechanics, be fundamental for the physical integration of the components involved in the various systems, specifically for the the motor module.

With the conclusion of this work it can be concluded that the objectives initially proposed for this thesis were achieved in its majority. In retrospective, the work carried out allows to conclude that:

- The proposed topologies for the traction and charging systems were respectively validated in computer simulations;
- The PCB development and the assembly of the traction and charging systems were, overall, correctly implemented.
- The proposed control algorithms were experimentally validated, namely the torque control, the PI controls, as well as the SPWM and PWM techniques;
- It was verified the ability of the charger system to provide a controllable and constant current at the output, while absorbing a power grid current with low harmonic content and regulating the DC-link voltage;
- It was validated the performance of the traction system, where it was possible to control the motor torque by means of a hand accelerator and it was verified the respective modes of operation and transitions between them.

## 7.2 Future Work Proposals

Despite the conclusion of this thesis there are still aspects that should be perfected, and improvements to be implemented, for example:

- Correct the errors in the development of the control PCB;
- Improve the testing conditions in order to redo the experimental tests and progressively achieve the rated power values;
- Improve the PFC control in the charger system to obtain better results in regard to the absorbed current THD;
- Implement a more robust and safer charging protocol, such as a CC-CV or CC-CT techniques;
- Redo the experimental tests of both traction and charger systems using a real battery as a supply and load, respectively;

- Implement a controllable semiconductor in series with a power resistor close to the battery (traction system), in order to dissipate power spikes and overloads that can damage the converter during regenerative braking.

# Bibliography

[1] United Nations. *Monomeric indole alkaloids from the aerial parts of Catharanthus roseus*. 2010.

[2] C. S. Boopathi, Soutreyo Saha, Anvita Singh, and Soumyajeet Sinha. Regenerative braking in electric vehicles. *International Journal of Recent Technology and Engineering*, 8(2 Special Issue 11):3338–3346, 2019.

[3] Juan De Santiago, Hans Bernhoff, Boel Ekergård, Sandra Eriksson, Senad Ferhatovic, Rafael Waters, and Mats Leijon. Electrical motor drivelines in commercial all-electric vehicles: A review. *IEEE Transactions on Vehicular Technology*, 61(2):475–484, 2012.

[4] João Luiz Afonso. Maquinas Elétricas, 1984.

[5] Chaelim Jeong, Junkyu Park, and Nicola Bianchi. Alternatives to replace rare-earth permanent magnet motors in direct drive applications. *2020 International Symposium on Power Electronics, Electrical Drives, Automation and Motion, SPEEDAM 2020*, pages 676–681, 2020.

[6] Gianmario Pellegrino, Alfredo Vagati, Barbara Boazzo, and Paolo Guglielmi. Comparison of induction and PM synchronous motor drives for EV application including design examples. *IEEE Transactions on Industry Applications*, 48(6):2322–2332, 2012.

[7] Sarlech Enterprises (India). Hand Blender Motor, 2020.

[8] Toshinori Baba. MT61 DC motor stator and brush, 2014.

[9] S.J. de Waard. Rotterdam Ahoy Europort 2011 (14), 2011.

[10] Yi Chun Hsu, Sheng Cheng Kao, Chi Yuan Ho, Pin Hong Jhou, Min Ze Lu, and Chang Ming Liaw. On an Electric Scooter with G2V/V2H/V2G and Energy Harvesting Functions. *IEEE Transactions on Power Electronics*, 33(8):6910–6925, 2018.

[11] Rini Nur Hasanah, Victor Andrean, Hadi Suyono, and Soeprapto. An effective method of regenerative braking for electric vehicles. *International Journal on Advanced Science, Engineering and Information Technology*, 7(5):1943–1949, 2017.

[12] S M Asyrafs, P M Heerwan, I M Izhar, I M Zulhilmi, and I M Sollehudin. Comparison of braking performance between mechanical and dynamic braking for electric powered wheelchair. *IOP Conference Series: Materials Science and Engineering*, 469:012104, jan 2019.

[13] Lutfi Al-Sharif. Overview and comparison of electrical and mechanical braking in drive systems. 12 2016.

[14] Murat Yilmaz and Philip T. Krein. Review of battery charger topologies, charging power levels, and infrastructure for plug-in electric and hybrid vehicles. *IEEE Transactions on Power Electronics*, 28(5):2151–2169, 2013.

[15] Tomislav Dragicevic, Josep M. Guerrero, Juan C. Vasquez, and Davor Skrlec. Supervisory control of an adaptive-droop regulated DC microgrid with battery management capability. *IEEE Transactions on Power Electronics*, 29(2):695–706, 2014.

[16] Peter Palensky, Edmund Widl, Matthias Stifter, and Atiyah Elsheikh. Modeling intelligent energy systems: Co-simulation platform for validating flexible-demand EV charging management. *IEEE Transactions on Smart Grid*, 4(4):1939–1947, 2013.

[17] Yijia Cao, Shengwei Tang, Canbing Li, Peng Zhang, Yi Tan, Zhikun Zhang, and Junxiong Li. An optimized EV charging model considering TOU price and SOC curve. *IEEE Transactions on Smart Grid*, 3(1):388–393, 2012.

[18] Zhe Wei, Yue Li, Yongmin Zhang, and Lin Cai. Intelligent parking garage EV charging scheduling considering battery charging characteristic. *IEEE Transactions on Industrial Electronics*, 65(3):2806–2816, 2018.

[19] Quasi-z-source Integrated On-board Charger, Tuopu Na, Qianfan Zhang, Jiaqi Tang, and Jinxin Wang. Active Power Filter for Single-Phase. 3(3):197–201, 2018.

[20] Christelle Saber, Denis Labrousse, Bertrand Revol, and Alain Gascher. Challenges Facing PFC of a Single-Phase On-Board Charger for Electric Vehicles Based on a Current Source Active Rectifier Input Stage. *IEEE Transactions on Power Electronics*, 31(9):6192–6202, 2016.

[21] Supasit Ketsingsoi and Yuttana Kumsuwan. An off-line battery charger based on buck-boost power factor correction converter for plug-in electric vehicles. *Energy Procedia*, 56(C):659–666, 2014.

[22] Ieee recommended practice and requirements for harmonic control in electric power systems. *IEEE Std 519-2014 (Revision of IEEE Std 519-1992)*, pages 1–29, 2014.

[23] R. D. Henderson and P. J. Rose. Harmonics: the effects on power quality and transformers. *IEEE Transactions on Industry Applications*, 30(3):528–532, 1994.

[24] B. Singh, B.N. Singh, Ambrish Chandra, Kamal Al-Haddad, Ashish Pandey, and D.P. Kothari. A review of single-phase improved power quality ac~dc converters. *IEEE Transactions on Industrial Electronics*, 50(5):962–981, oct 2003.

[25] Johann W. Kolar and Thomas Friedli. The essence of three-phase PFC rectifier systemspart i. *IEEE Transactions on Power Electronics*, 28(1):176–198, 2013.

[26] Hongbo Li, Kai Zhang, Hui Zhao, Shengfang Fan, and Jian Xiong. Active power decoupling for high-power single-phase PWM rectifiers. *IEEE Transactions on Power Electronics*, 28(3):1308–1319, 2013.

[27] Bhim Singh, Brij N. Singh, Ambrish Chandra, Kamal Al-Haddad, Ashish Pandey, and Dwarka P. Kothari. A review of three-phase improved power quality ac-dc converters. *IEEE Transactions on Industrial Electronics*, 51(3):641–660, 2004.

[28] J. R. Rodriguez, J. W. Dixon, J. R. Espinoza, J. Pontt, and P. Lezana. Pwm regenerative rectifiers: state of the art. *IEEE Transactions on Industrial Electronics*, 52(1):5–22, 2005.

[29] L. G. Barbosa Rolim, D. Rodrigues da Costa, and M. Aredes. Analysis and software implementation of a robust synchronizing pll circuit based on the pq theory. *IEEE Transactions on Industrial Electronics*, 53(6):1919, 2006.

[30] S. Golestan, M. Monfared, F. D. Freijedo, and J. M. Guerrero. Design and tuning of a modified power-based pll for single-phase grid-connected power conditioning systems. *IEEE Transactions on Power Electronics*, 27(8):3639–3650, 2012.

[31] Filipe Carvalho Machado. *Acionamento Eletrónico de Velocidade Variável com Retificador Ativo para Motor de Indução Trifásico*. PhD thesis, 2019.

[32] M R Iravani. A New Phase-Locked Loop ( PLL ) System. pages 5–8, 2001.

[33] Joerg Dannehl, Christian Wessels, and Friedrich Wilhelm Fuchs. Limitations of voltage-oriented PI current control of grid-connected PWM rectifiers with LCL filters. *IEEE Transactions on Industrial Electronics*, 56(2):380–388, 2009.

[34] Kaveh Sarrafan, Kashem M. Muttaqi, and Danny Sutanto. Real-Time Estimation of Model Parameters and State-of-Charge of Li-Ion Batteries in Electric Vehicles Using a New Mixed Estimation Model. *IEEE Transactions on Industry Applications*, 56(5):5417–5428, 2020.

[35] Henry Miniguano, Andres Barrado, Antonio Lazaro, Pablo Zumel, and Cristina Fernandez. General parameter identification procedure and comparative study of Li-Ion battery models. *IEEE Transactions on Vehicular Technology*, 69(1):235–245, 2020.

[36] Xing Luo, Jihong Wang, Mark Dooner, and Jonathan Clarke. Overview of current development in electrical energy storage technologies and the application potential in power system operation. *Applied Energy*, 137:511–536, 2015.

[37] Yongquan Sun, Lingxi Kong, Hassan Abbas Khan, and Michael G. Pecht. Li-ion Battery Reliability - A Case Study of the Apple iPhone®. *IEEE Access*, 7:71131–71141, 2019.

[38] Haining Liu, Ijaz Haider Naqvi, Fajia Li, Chengliang Liu, Neda Shafiei, Yulong Li, and Michael Pecht. An analytical model for the CC-CV charge of Li-ion batteries with application to degradation analysis. *Journal of Energy Storage*, 29(March), 2020.

[39] Claus Ableiter. Lithium-Ionen-Accumulator, 2018.

[40] Vinicius Albanas Marcis, A. V.J.S. Praneeth, Lalit Patnaik, and Sheldon S. Williamson. Analysis of CT-CV Charging Technique for Lithium-ion and NCM 18650 Cells. *2020 IEEE International Conference on Power Electronics, Smart Grid and Renewable Energy, PESGRE 2020*, (1):947–952, 2020.

[41] Lalit Patnaik, A. V.J.S. Praneeth, and Sheldon S. Williamson. A Closed-Loop Constant-Temperature Constant-Voltage Charging Technique to Reduce Charge Time of Lithium-Ion Batteries. *IEEE Transactions on Industrial Electronics*, 66(2):1059–1067, 2019.

[42] Heng Li, Xiaoyong Zhang, Jun Peng, Jianping He, Zhiwu Huang, and Jing Wang. Cooperative CC-CV Charging of Supercapacitors Using Multicharger Systems. *IEEE Transactions on Industrial Electronics*, 67(12):10497–10508, 2020.

[43] Single-phase Drive System, Ahmad M Al-kandari, and Tamer H Abdelhamid. A sinusoidal PWM Control For Four-Quadrant. pages 147–151, 2002.

[44] Zhi Yang, Fei Shang, Ian P. Brown, and Mahesh Krishnamurthy. Comparative study of interior permanent magnet, induction, and switched reluctance motor drives for EV and HEV applications. *IEEE Transactions on Transportation Electrification*, 1(3):245–254, 2015.

[45] Stijn Derammelaere, Michiel Haemers, Jasper De Viaene, Florian Verbelen, and Kurt Stockman. A quantitative comparison between BLDC, PMSM, brushed DC and stepping motor technologies. In *19th International Conference on Electrical Machines and Systems, ICEMS 2016*, pages 1–5. The Institute of Electrical Engineers of Japan, 2017.

[46] Aaron M. Harrington and Christopher Kroninger. Characterization of Small DC Brushed and Brushless Motors. *Arl-Tr-6389*, (March):1–48, 2013.

[47] André Thess, Evgeny Votyakov, Bernard Knaepen, and Oleg Zikanov. Theory of the Lorentz force flowmeter. *New Journal of Physics*, 9:1–4, 2007.

[48] S. H. Kim, S. Hashi, and K. Ishiyama. A method for acquiring the torque of a magnetic pump. *IEEE Transactions on Magnetics*, 47(10):3971–3974, 2011.

[49] K R Sidhdhapura and D B Raval. *DC Machines and Transformers Lecture Notes*. 2015.

[50] Miguel Angel Rodríguez Pozueta. Principio motor c.c, 2010.

[51] Juan Carlos A. Floriani. Generalized analysis of current ripple in a pulsewidth modulation H-bridge converter with unipolar-bipolar switching. *IEEE Power Electronics Letters*, 2(3):83–86, 2004.

[52] G. Hu Chen and Ming Yang Cheng. MOTA Implementation of a highly reliable hybrid electric scooter drive. *IEEE Transactions on Industrial Electronics*, 54(5):2462–2473, 2007.

[53] Young Joo Lee, Alireza Khaligh, and Ali Emadi. A compensation technique for smooth transitions in a noninverting buck-boost converter. *IEEE Transactions on Power Electronics*, 24(4):1002–1015, 2009.

[54] Angelica Mendoza-Torres, Nancy Visairo, Ciro Nuñez, Jesus Armenta, Elías Rodríguez, and Ilse Cervantes. Switching rule for a bidirectional DC/DC converter in an electric vehicle. *Control Engineering Practice*, 82(March 2018):108–117, 2019.

[55] Kuo Chun Wu, Hung Hsien Wu, and Chia Ling Wei. Analysis and Design of Mixed-Mode Operation for Noninverting Buck-Boost DC-DC Converters. *IEEE Transactions on Circuits and Systems II: Express Briefs*, 62(12):1194–1198, 2015.

[56] Feng Kuang Wu, T. J. Yeh, and Chun Feng Huang. Motor control and torque coordination of an electric vehicle actuated by two in-wheel motors. *Mechatronics*, 23(1):46–60, 2013.

[57] Giuseppe S. Buja and Marian P. Kazmierkowski. Direct torque control of PWM inverter-fed AC motors - A survey. *IEEE Transactions on Industrial Electronics*, 51(4):744–757, 2004.

[58] Inc Montenergy. ME1003 Data sheet. pages 1–4, 2011.

[59] Robert Oshana. 4 - overview of digital signal processing algorithms. In Robert Oshana, editor, *DSP Software Development Techniques for Embedded and Real-Time Systems*, Embedded Technology, pages 59–121. Newnes, Burlington, 2006.

[60] M. Karimi-Ghartemani and M.R. Iravani. A new phase-locked loop (pll) system. In *Proceedings of the 44th IEEE 2001 Midwest Symposium on Circuits and Systems. MWSCAS 2001 (Cat. No.01CH37257)*, volume 1, pages 421–424 vol.1, 2001.

[61] Takeshi Ishigohka, Kenji Uno, and Sakio Nishimiya. Experimental study on effect of In-rush current of superconducting transformer. *IEEE Transactions on Applied Superconductivity*, 16(2):1473–1476, 2006.

[62] Mi Zhou, Zhuochao Sun, Qiong Wei Low, and Liter Siek. Multiloop control for fast transient DC-DC converter. *IEEE Transactions on Very Large Scale Integration (VLSI) Systems*, 27(1):219–220, 2019.

[63] Texas Instruments Incorporated. TMS320F2833x, TMS320F2823x Digital Signal Controllers (DSCs) 1 Device Overview. *Texas Instruments*, page 203, 2016.

[64] Markt Schwabener Str and Dr-Ing habil Jigou Liu. Hall Effect Voltage Sensor CYHVS5-25A. 49(May):2574100–2574102, 2016.

[65] Lem. Current Transducer LTS 25-NP I PN 25 At, 2001.

[66] LEM. Current Transducer LA 100-NP Electrical Data, 2011.

[67] LEM. Current Transducer LA 200-P datasheet, 1997.

[68] RLS. AM512B – Angular magnetic encoder IC, 2016.

[69] Texas Instruments. 2 . 5-V INTEGRATED REFERENCE CIRCUIT DESCRIPTION / ORDERING INFORMATION LT1009 2 . 5-V INTEGRATED REFERENCE CIRCUIT, 2005.

[70] Motorola. LM339 - QUAD Single Supply Comparators, 1996.

[71] Texas Instruments. LM555 Timer, 2000.

[72] Analog Devices. Datasheet: ADUM3123. pages 1–12, 2015.

[73] The Korean, Society For, and Space Sciences. TMA1515S. pages 1–9, 2005.

[74] SEMIKRON. SKHI SEMIDRIVER. pages 2–12, 2008.

[75] Delfim Pedrosa. Memória descritiva/relatório de ensaio - GEPE-0015. pages 1–5, 2010.

[76] Delfim Pedrosa. MEMÓRIA DESCRITIVA / RELATÓRIO DE ENSAIO - GEPE-0025. pages 3–5, 2017.

[77] Texas Instruments. 8-CHANNEL, 12-/10-/8-BIT, 2.7-V TO 5.5-V LOW POWER DIGITAL-TO-ANALOG CONVERTER WITH POWER DOWN - TLV5610 TLV5608 TLV5629. (May 2000), 2008.

[78] STMicroelectronics. Ultrafast recovery - 1200 V diode - STTH3012 datasheet. (March):1–9, 2006.

[79] Datasheet: IGBT FGA25N120. *Fairchild*, (May):1–10, 2006.

[80] SEMIKRON. SKM400GB Datasheet. pages 8–11, 2003.